

Improved Simulation Techniques for Modelling Impact and Crash Behaviour of Composite Structures

Von der Fakultät für Luft- und Raumfahrttechnik und Geodäsie
der Universität Stuttgart zur Erlangung der Würde
eines Doktor-Ingenieurs (Dr.-Ing.)
genehmigte Abhandlung

vorgelegt von

Levent Aktay

aus Ankara (Türkei)

Hauptberichter : Prof. Dr.-Ing.habil. B. Kröplin
Mitberichter : Prof. Dr.-Ing. H. Voggenreiter
Tag der mündlichen Prüfung : 13. Juli 2009

Institut für Statik und Dynamik der Luft- und Raumfahrtkonstruktionen
der Universität Stuttgart

2010

Dedicated to my wife Kátia and my son Kaan Leonardo

Acknowledgements

First of all, I would like to express my profound gratitude to the German Aerospace Center (DLR), specifically to the Institute of Structures and Design, where I conducted this research, for making this work possible and for supporting me financially throughout the time of the doctorate.

I offer my sincerest thanks to my committee members: to the chair, Prof. Dr.-Ing. habil. Bernd Kröplin, Director of the Institute for Statics and Dynamics of Aerospace Structures at the University of Stuttgart, and to the co-chair, Prof. Dr.-Ing. Heinz Voggenreiter, Director of the Institute of Structures and Design at DLR, for supporting this work.

I am indebted to the head of the Department of Structural Integrity, Christof Kindervater, for giving me the opportunity to work in his department.

I am deeply grateful to my supervisor, Dr. phil. Alastair Johnson, whose idea was the starting point of my long journey in the world of particles and composite materials. His neverending support, detailed and constructive comments, guidance, understanding and encouragement provided the basis for the present dissertation. His intellectuality and personality extended our discussions beyond the research topics onto several others which made valuable contribution to my personal and professional development.

During this work I had the opportunity to collaborate with Prof. Dr. Mustafa Güden and his research assistant Ahmet Kaan Toksoy from the Department of Mechanical Engineering at the Izmir Institute of Technology (IYTE) in Turkey. I express my sincere thanks to them for enabling a perfect collaboration and for their valuable support, which I heartly appreciated.

Over the years I have been helped and encouraged by my colleagues and by the administrative staff of the DLR Department of Structural Integrity. However, there are some people whom I would like to single out for special thanks: Nicole Lützenburger, Dieter Kohlgrüber and Parya Naghipour. Thanks are also due to Rodolfo Aoki, Harald Kraft, Albert Reiter for conducting the experiments reported in Chapter 5.

This dissertation would not have been possible without the confidence, endurance and support of my family, who has always been a source of inspiration and encouragement. I thank my parents, whose love, teachings and believe in me have brought me this far.

Finally, I give my special thanks to my wife, Kátia, whose patience and understanding enabled me to complete this work. Her neverending support let me concentrate just on my PhD Thesis for many weekends. Obrigado mil vezes!!

This dissertation is dedicated to her for her unconditional support and love and to my son "tatlı" Kaan Leonardo who brought so much happiness to our life. Sorry for the days that "Baba" was whole day at home to study for his PhD exam and couldn't play with you!!

Stuttgart, Januar 2010

Levent Aktay

Contents

Acknowledgements	iv
Contents	vii
List of Figures	xiii
Abbreviations	xiv
Abstract	xvi
Kurzfassung	xviii
1 Introduction	1
1.1 Crashworthiness and Impact in Aerospace Structures	1
1.2 Industry Requirement	6
1.3 Plan of the Thesis	7
2 Literature Review	9
2.1 Energy Absorption and Energy Absorbing Structures	9
2.2 Crashworthiness and Impact in Aerospace Structures	18
3 Numerical Modelling of Crush and Impact Mechanisms	21
3.1 Finite Element Method	22
3.2 Other Alternative Methods	28
3.3 Review of Particle-based Meshless Methods	28
3.4 Conservation Laws in SPH Method	35
4 Coupling between Finite Element Method and Meshless Methods	39
4.1 Need for Coupling	39
4.2 Principles of Direct Coupling	40
4.3 Principles of Adaptive Coupling	40
4.4 Principles of Semi-Adaptive Coupling	41
4.5 Benchmark Simulations	42

5	Application of Meshless Methods in Impact Simulations	53
5.1	Experimental HVI Investigations	53
5.2	Numerical Modelling of HVI Simulations - FEM	59
5.3	Discussion - FEM	62
5.4	Numerical Modelling of HVI Simulations - SPH and Direct-Coupled FEM/SPH Method	62
5.5	Discussion - SPH and Direct-Coupled FEM/SPH Method	70
5.6	Numerical Modelling of HVI Simulations - Semi-Adaptive Coupling . . .	70
5.7	Discussion - Semi-Adaptive-Coupled FEM/SPH Method	73
5.8	Final Discussion	77
6	Application of Meshless Methods in Crash and Energy Absorbing Structures	79
6.1	Experimental Investigations on Empty and Foam-filled Aluminum Crash Absorbers	79
6.2	Numerical Modelling of Foam-filled Aluminum Crash Absorbers - FEM	82
6.3	Discussion - FEM	93
6.4	Numerical Modelling of Foam-filled Aluminum Crash Absorbers - SPH and Direct-Coupled FEM/SPH Method	93
6.5	Discussion - SPH and Direct-Coupled FEM/SPH Method	104
6.6	Numerical Modelling of Bitubular Foam-filled Aluminum Crash Absorbers - SPH and Direct-Coupled FEM/SPH Method	104
6.7	Discussion - SPH and Direct-Coupled FEM/SPH Method	112
6.8	Discussion - Numerical Modelling of Aluminum Crash Absorbers	112
6.9	Composite Crush Absorbers	112
6.10	Experimental Investigations on Carbon-Fibre-Reinforced Composite Tube Segments	113
6.11	Numerical Modelling of the Carbon-Fibre-Reinforced Segments	120
6.12	Discussion - Numerical Modelling of the Carbon-Fibre-Reinforced Seg- ments	125
	Conclusions	127
	Schlussfolgerungen	129
	Bibliography	131

List of Figures

1.1	Composite parts used in Airbus 380 [1]	2
1.2	Composite parts used in Boeing 787 Dreamliner [2]	2
1.3	Possible impact loading cases on aircraft [3]	3
1.4	Energy absorption sequence during vertical crash of a crash-resistant aircraft system [4]	5
2.1	Classification chart for collapse modes and aluminum (Al) alloy tubes under axial compression [8]	11
2.2	Schematic representation of the formation of the splaying/lamina bending mode crush zone based on macroscopic examination [33]	15
2.3	Schematic representation of the formation of the fragmentation/transverse shearing mode crush zone based on macroscopic examination [33]	16
3.1	Homogenised core modelling	25
3.2	Unit cell core modelling	25
3.3	Layered shell model for facings	25
3.4	Stacked shell model for facings	25
4.1	a) Selection of the FEs for the conversion into SPH particles, b) conversion of the FEs into SPH particles and c) final discretisation of the FEM/SPH coupling	43
4.2	Compression of foam block modelled with discrete particles	44
4.3	Tension test of the flat specimen modelled with FEM/SPH coupling	45
4.4	Impact of a rigid impactor on a composite sandwich plate using EET-based damage model	47
4.5	Enrichment of composite sandwich core with a) global enrichment with 1 particle , b) local enrichment with 4 particles and c) detailed view of impact damage zone	48
4.6	Impact of a rigid impactor on a composite sandwich plate using SAC-based damage model (1 discrete particle for 1 FE)	49
4.7	Impact of a rigid impactor on a composite sandwich plate using SAC-based damage model (4 discrete particles for 1 FE)	50

4.8	Tension test of the flat specimen modelled with FEM/SPH coupling (Discrete particles are embedded in FEs)	51
5.1	Concrete projectiles (26 ϕ mm x 37mm and 30 ϕ mm x 50mm)	54
5.2	Damage to sandwich plate after impact	54
5.3	Stress-strain diagram	57
5.4	Corresponding fracturing damage function	57
5.5	Stress-strain plot of PEI foam core	58
5.6	Stress-strain plot of Nomex core	60
5.7	a) Final state of PEI core sandwich plate, b) comparison of the contact force history plots	61
5.8	a) Final state of Nomex core sandwich plate, b) comparison of the contact force history plots	61
5.9	Kinetic and internal energy history plot for a) PEI core sandwich plate, b) Nomex core sandwich plate	61
5.10	Numerical HVI model: a) FEM, b) SPH and c) direct-coupled FEM/SPH model	64
5.11	Maximum core penetration for a) FEM, b) SPH and c) direct-coupled FEM/SPH model	64
5.12	Contact force history of a) FEM vs. Experiment, b) SPH vs. Experiment and c) FEM/SPH vs. Experiment	65
5.13	Glass impactors	66
5.14	a) Impact damage on upper skin, b) damage on upper skin and core, c) damage on upper skin and core and d) backside damage	67
5.15	Impact states $V_o = 65.8\text{m/s}$: a) $t=0.16\text{ms}$, b) $t=0.36\text{ms}$, c) $t=0.72\text{ms}$ and d) $t=1.20\text{ms}$	68
5.16	Impact states $V_o = 108\text{m/s}$: a) $t=0.16\text{ms}$, b) $t=0.20\text{ms}$, c) $t=0.36\text{ms}$ and d) $t=0.80\text{ms}$	68
5.17	Impact states $V_o = 95.1\text{m/s}$: a) $t=0.16\text{ms}$, b) $t=0.28\text{ms}$, c) $t=0.52\text{ms}$, d) $t=0.88\text{ms}$, e) $t=1.00\text{ms}$ and f) backside damage, side view	69
5.18	Stages of quasi-static compression test of Nomex honeycomb: a) buckling initiation, b) progressive folding and c) densification	71
5.19	Stages of quasi-static compression of Nomex honeycomb at 30% and 60% compressive strain a) experiment (initial and 60% deformation), b) FE analysis with 1mm and c) 0.5mm element size	72
5.20	Comparison between the load-displacement curves obtained by experi- ment and the numerical model using micromechanical model of Nomex honeycomb in compression	73
5.21	Comparison between the experimental and numerical stress-strain his- tory of Nomex honeycomb under compression	74

5.22	Application of SAC technique for modelling of Nomex honeycomb crush behaviour: a) homogenised FE model, b) 30% and c) 50% compression of core showing eliminated solids replaced by SPH particles	75
5.23	Numerical views of impact simulation using homogenised models: a) initial state, b) t=0.4ms and c) t=0.6ms	76
5.24	Numerical views of impact simulation using SAC technique: a) initial state, b) t=0.4ms and c) t=0.6ms	76
5.25	Comparison of experimental and SAC-based numerical contact force histories	77
6.1	Bitubular configurations a) BPH, b) BPP and c) BPA	80
6.2	a) Tensional engineering stress-strain curve of Al tube material, b) quasi-static compression stress-strain curve of PS foam fillers	80
6.3	Compression stress-strain curves of Al foam fillers	82
6.4	FE discretisation of a) empty tube (full model), b) foam-filled tube (half model), 1 and 2: compression test plates, 3: empty and foam-filled tube meshing and 4: foam-filler meshing	83
6.5	Quasi-static compression stress-strain curve of PS foam fillers	84
6.6	Penetration of the tube wall into foam filler	85
6.7	a) Kinetic and internal energy histories of 25mm empty tubes at various density scaling and deformation rates, b) corresponding load-displacement curves	86
6.8	Numerical and experimental load-displacement curves of 25mm empty tube for different meshes along the height: a) 40x20, b) 40x40, c) 40x80 and d) 40x160	87
6.9	a) Comparison of experimental and numerical load-displacement curves of 25mm empty tube, b) comparison of experimental and numerical average load-displacement curves of 25mm empty tube	88
6.10	Deformation histories of 25mm empty tube at various percentage deformation ratios: a-c) experimental, d-f) numerical	89
6.11	Deformation histories of 25mm 27.8kg/m ³ PS foam-filled tube at various percentage deformation ratios: a) experimental, b) numerical	89
6.12	Numerical and experimental load-displacement curves of 25mm 27.8kg/m ³ PS foam-filled tube	90
6.13	Images of side views of partially deformed 25mm 27.8kg/m ³ PS foam-filled tubes at 30% deformation; filler and tube surfaces	90
6.14	Numerical and experimental fold lengths vs. foam density	91
6.15	Numerical and experimental SAEs (at 50% deformation) in tubes as function of foam density	92
6.16	Discrete particle modelling of foam filler: a) general, b) detailed view . .	94

6.17	Coupled solid element/discrete particle modelling of foam filler: a) general, b) detailed view	94
6.18	a) The initial FEM model for the SPH and direct-coupled FEM/SPH modelling: a) 1: Central deformation zone, 2: Tube interaction deformation zone, b) conversion of solid elements into discrete particles and c) discrete modelling of foam-filler	95
6.19	Comparison of compression responses of PS foam with the density of a) 21.7kg/m ³ , b) 27.8kg/m ³ using FEM and SPH	96
6.20	Initial states (a and c) and 30% compression strain (b and d) of FEs and discrete particles under numerical constrained compression setup	97
6.21	a) Initial distribution of the particles, b) equidistant distribution of the particles	97
6.22	The comparison of load-displacement response of particle distribution (Original: initial particle distribution, equal distance: equidistant particle distribution)	98
6.23	The comparison of load-displacement response of number of particles (Original: 1296 particles, half: 648 particles and double: 2592 particles)	98
6.24	The numerical deformation modes at 50% compression: a) Initial model, b) model with half number of particles and c) model with double number of particles	99
6.25	The comparison of load-displacement response of maximum smoothing length	99
6.26	The comparison of load-displacement response of number of particles and solid elements: Original: 576 particles/600 FEs, half: 288 particles/300 FEs, double: 1152 particles/1200 FEs	100
6.27	The numerical deformation modes at 50% compression: a) Initial model, b) model with half number of particles and solid elements and c) model with double number of particles and solid elements	101
6.28	SPH model progressive folding of foam-filled tube at a) 30%, b) 50% and c) 80% deformation	101
6.29	Coupled FEM/SPH model progressive folding of foam-filled tube at a) 30%, b) 50% and c) 80% deformation	101
6.30	Comparison of experimental and numerical load-displacement curves of foam-filled tube: a) SPH, b) direct-coupled FEM/SPH	102
6.31	Deformed shapes of foam-filled tubes at 50% deformation: a) FEM, b) SPH and c) direct-coupled FEM/SPH	102
6.32	a) Numerical and experimental fold lengths at 50% deformation, b) comparison of experimental and numerical SAE vs. displacement curves of foam-filled tube	103
6.33	Material model for Al foam [161]	105

6.34	Images of crushed 25mm-diameter Al tube at a) 0%, b) 40% and c) 80% strains	106
6.35	a) Numerical and experimental load-displacement curve of a) 25mm- and b) 35mm-diameter empty tubes	106
6.36	Images of crushed 25mm-diameter Al foam-filled (270kg/m^3) tube at a) 0%, b) 40% and c) 70% strains	107
6.37	Numerical images of crushed 25mm-diameter Al foam-filled (270kg/m^3) tube at a) 0%, b) 40% and c) 70% deformation	107
6.38	Numerical and experimental load-displacement curves of a) 270kg/m^3 , b) 350kg/m^3 and c) 430kg/m^3 Al foam-filled 25mm tubes	108
6.39	Top view of deformed: a) BPH, b) BPP and c) BPA bitubular configurations. In a) both tubes deformed on diamond mode, while interior tube deformed in concertina mode in b) and c)	108
6.40	Side view of crushed BPA specimen	109
6.41	Numerical images of crushed BPH design at a) 0%, b) 40% and c) 65% deformation	109
6.42	Numerical images of crushed BPP design at a) 0%, b) 40% and c) 65% deformation	110
6.43	Numerical images of crushed BPA design at a) 0%, b) 40% and c) 65% deformation	110
6.44	Numerical and experimental load-displacement curves of a) BPH, b) BPP and c) BPA designs	111
6.45	Crushing behaviour of different tube segment specimens [176]	113
6.46	Sketch of the DLR-tube segment specimen [176]	115
6.47	Carbon-fibre-reinforced segment $0^\circ/90^\circ$ specimen after dynamic crushing test with $v_0=5\text{m/s}$ [176]	116
6.48	Results of dynamic crushing tests - $0^\circ/90^\circ$ ($v_0=5\text{m/s}$)	116
6.49	Carbon-fibre-reinforced $0^\circ/90^\circ$ specimens after dynamic crushing test with $v_0=10\text{m/s}$ [176]	117
6.50	Results of dynamic crushing tests - $0^\circ/90^\circ$ ($v_0=10\text{m/s}$)	118
6.51	Carbon-fibre-reinforced $\pm 45^\circ$ specimen after dynamic crushing test with $v_0=5\text{m/s}$ [176]	118
6.52	Results of dynamic crushing tests - $\pm 45^\circ$ ($v_0=5\text{m/s}$)	119
6.53	Carbon-fibre-reinforced $\pm 45^\circ$ specimen after dynamic crushing test with $v_0=10\text{m/s}$ [176]	119
6.54	Results of dynamic crushing tests - $\pm 45^\circ$ ($v_0=10\text{m/s}$)	120
6.55	a) Modelling of segment walls, b) modelling of resin	121
6.56	a) Representation of the delamination interface, b) representation of the debonding interface	122

6.57	Numerical images of crushed carbon-fibre-reinforced composite segment ($v_0=5\text{m/s}$) at a) 0%, b) 20%, c) 40%, d) 60% and e) 80% deformation .	123
6.58	Numerical images of crushed carbon-fibre-reinforced composite segment ($v_0=10\text{m/s}$) at a) 0%, b) 20%, c) 40%, d) 60% and e) 80% deformation	124
6.59	Results of dynamic crushing tests - $0^\circ/90^\circ$ ($v_0=5\text{m/s}$)	125
6.60	Results of dynamic crushing tests - $0^\circ/90^\circ$ ($v_0=10\text{m/s}$)	126

Abbreviations

Al	Aluminum
ALE	Arbitrary Lagrangian Eulerian
BEM	Boundary Element Method
CFD	Computational Fluid Dynamics
CFRP	Carbon-Fibre-Reinforced Plastics
CPU	Central Processing Unit
DE	Discrete Element
DEM	Discrete Element Method
DLR	Deutsches Zentrum für Luft- und Raumfahrt e.V.
EA	Energy Absorption
EET	Element Elimination Technique
EFG	Element Free Galerkin
EOS	Equation of State
FDM	Finite Difference Method
FE	Finite Element
FEM	Finite Element Method
FVM	Finite Volume Method
GFRP	Glass Fibre-Reinforced Plastics (GFRP)
HV	High Velocity
HVI	High Velocity Impact
MDO	Multidesign Optimization
MLPG	Meshless Local Petrov-Galerkin
PDE	Partial Differential Equation
PEI	Polyetherimide
PS	Polysytrene
PU	Polyurethane
PVC	Polyvinylchloride
SAE	Specific Absorbed Energy
SA	Semi-Adaptive
SAC	Semi-Adaptive Coupling
SAN	Styreneacrylanitrile
SMC	Sheet Moulding Compound
SPH	Smooth Particle Hydrodynamics
UD	Unidirectional

Abstract

Composite elements such as glass- and carbon-fibre-reinforced tubes in axial crush exhibit high specific energy absorption (SEA) and a challenge for the engineer is to utilise these properties in structural applications. Numerical tools based on the Finite Element Method (FEM) are unable to simulate accurately the observed crush fronts in brittle composite composed of delaminations with fibre and matrix debris, which have a strong influence on energy absorption (EA). As alternative Meshless Methods replace finite element (FE)s by a set of nodes or particles and have the potential to simulate the fragmentation behaviour. However, they are computationally less efficient and costly and appropriate material models and failure criteria are not yet established. Therefore there is an increasing interest in combining the two different numerical methods. Such coupling could exploit the potential of each method while avoiding their deficiencies.

In this work the meshless Smooth Particle Hydrodynamics (SPH) Method was used for modelling of composite damage phenomena under crash and impact loads. The computational studies were conducted in the explicit numerical tool PAM-CRASH. Because SPH Method is computationally expensive depending on the dynamic neighbouring search algorithm, new numerical techniques were suggested to reduce the computational time. In these techniques the failure region was modelled using a discrete particle formulation (direct coupling) or the FE mesh was converted into discrete particles (semi-adaptive coupling) to model the debris in the propagating crush front. The coupling was applied through a sliding interface condition.

The applicability of SPH Method was firstly tested via benchmark simulation examples, which helped understanding the numerical response of discrete modelling under different loading conditions. The results of the benchmark study were extended to high velocity impact (HVI) simulations of sandwich composite panels. These numerical simulations were conducted for different sandwich panel configurations, impactor shapes and impact velocities. The sandwich panels consisted of carbon fibre/epoxy facings and a core of polyetherimide (PEI) or aramid paper honeycomb (Nomex). The facings were modelled with standard layered shell elements whilst for the PEI core discrete particles were used. In the case of the Nomex core, the core material was modelled with standard solid elements in which the discrete particles were embedded. The numerical

results, such as contact force, core deformation and maximum penetration, obtained by using FEM, SPH Method, direct- and semi-adaptive coupled FEM/SPH Method were compared with the experimental results of gas gun impact tests and good agreement was observed. The coupled techniques showed that they can describe more accurately the physical phenomena involved in the EA in the core, where element distortion occurs. Due to the increase of computational time with increasing number of particles, the coupled techniques showed to be adequate since SPH Method was only employed in the impact damage zone.

The crashworthy response of aluminum (Al) and composite energy absorbers made of carbon fibre composites were also studied. For both crash absorbers, the tube walls were modelled with shell elements. In the case of metallic tubes, the discrete and the coupled FE/discrete element (DE)s were used to model the polystyrene (PS) foam-filler. For the composite energy absorbers, the crushing response of tube segments specially developed for crushing studies was investigated. These segments could be easily built in thermoset and thermoplastic composite materials with the advantage of giving an indication on the crushing behaviour of bigger structural component made of the same material. For their modelling, the layered shell model was used. The resin material, which showed elastic-plastic material response during crushing, was modelled with discrete particles while bonding and delamination with tied-contact algorithm. Numerical results were also compared with experimental data obtained by crush tests. They showed good agreement for the Al absorbers. Since these tubes are, from the point of view of particles, a closed domain, the experimentally observed deformation modes could be successfully numerically reproduced. This mainly relied on the reproducibility of the crushing behaviour of the metallic structures and their well-known standard material parameters. Composite specimens on the other hand presented different deformation patterns.

Kurzfassung

Verbundstrukturen wie glasfaser- und kohlefaserverstärkte Rohre weisen unter axialer Crushing-Belastung ein hohes spezifisches Energieabsorptionsvermögen auf. Dem Ingenieur wird die Herausforderung gestellt, diese Materialeigenschaften für die Anwendung in Strukturen einzusetzen. Numerische Verfahren, die auf der Finite-Elemente-Methode (FEM) basieren, sind meistens nicht dazu geeignet, die Crushing-Front, die in spröden Verbundwerkstoffen beobachtet wird, genau zu simulieren. Diese Front spielt dennoch eine bedeutende Rolle bei dem Energieabsorptionsvermögen der Verbundstrukturen. Netzfremde Methoden hingegen stellen eine Alternative dar, in der die finiten Elemente durch Knoten oder Partikel ersetzt werden. Diese Methoden haben somit das Potenzial, das Fragmentationsverhalten von Verbundstrukturen zu simulieren. Sie sind jedoch numerisch weniger effizient und kostenspielig. Außerdem sind geeignete Materialmodelle und Versagenskriterien noch nicht etabliert. Daher besteht ein zunehmendes Interesse an der Kopplung dieser zwei unterschiedlichen numerischen Verfahren, welche die Vorteile jedes Verfahrens ausnutzen, ohne deren Nachteile mit einzubeziehen.

In der vorliegenden Arbeit wurde das netzfremde Smooth-Particle-Hydrodynamics (SPH) Verfahren für die Modellierung des Nachbruchverhaltens von Verbundstrukturen unter Crash- und Impaktbelastungen eingesetzt. Die numerischen Untersuchungen wurden mit Hilfe des expliziten Berechnungsprogramms PAM-CRASH durchgeführt. Da das SPH-Verfahren je nach ausgewähltem Algorithmus zur dynamischen Suche der umliegenden Partikel numerisch betrachtet kostenintensiver wird, wurden hierfür neue numerische Verfahren zur Minimierung der Rechenzeit vorgeschlagen. Diese verwendeten eine diskrete Partikel-Formulierung für die Modellierung der Versagenszone (direkte Kopplung) oder ersetzten die finiten Elemente durch diskrete Partikel für die Modellierung von Debris in der sich ausbreitenden Crushing-Front (semi-adaptive Kopplung). In beiden Fällen wurde die Kopplung durch die sliding interface condition realisiert.

Die Einsetzbarkeit des SPH-Verfahrens wurde zunächst an Hand von Benchmark Simulations-Beispielen getestet. Diese Beispiele trugen dazu bei, die numerische Antwort der diskreten Modellierung unter bestimmten Lastbedingungen zu verstehen. Die daraus resultierenden Ergebnisse wurden anschließend für die Simulation von Hochgeschwindigkeitsimpakt (HVI) an Sandwich-Verbundplatten herangezogen. Bei der Berechnung

wurden verschiedene Sandwich-Platten-Konfigurationen, Impaktorgeometrien und Impaktgeschwindigkeiten verwendet. Die Sandwich-Verbundplatten bestanden aus Kohlefaser/ Epoxy-Außenschalen und einem Kern aus Polyetherimide (PEI) oder aus einer Aramid Papierwabenstruktur (Nomex). Die Außenschalen wurden mit konventionellen mehrschichtigen Schalenelementen modelliert, der PEI-Kern mit diskreten Partikeln. Der Nomex-Kern wurde mit herkömmlichen Solid-Elementen mit eingebetteten diskreten Partikeln modelliert. Die numerischen Ergebnisse, die mittels FEM, SPH, direktem und semi-adaptiv gekoppeltem FEM/SPH-Verfahren gewonnen wurden, wurden mit experimentellen Ergebnissen aus Impakt-Tests verglichen und zeigten eine gute Übereinstimmung. Die vorgeschlagenen gekoppelten numerischen Verfahren ermöglichten eine bessere Beschreibung der Energieabsorption im Kern, wo Elementdistortion stattfindet. Aufgrund der erhöhten Rechenzeit und mit zunehmender Anzahl von angewandten Partikeln erwies sich der Einsatz des SPH-Verfahrens, wie in der Arbeit vorgeschlagen, beschränkt auf die Impakt-Versagenszone, als adäquat.

Zusätzlich wurde das Nachbruchverhalten von Aluminium- und Verbund-Crashrohren bestehend aus Kohlefasergewebe untersucht. Für die beiden Crashrohrtypen wurden die Rohrwände mit Schalenelementen modelliert. Diskrete und gekoppelte finite/diskrete Elemente wurden für die Beschreibung der Polystyrene-Schaumfüllung des metallischen Crashrohrs eingesetzt. Rohrsegmente wurden als Verbund-Crashrohre verwendet und ihr Crushing-Verhalten untersucht. Diese Segmente, bestehend aus Thermoset- und thermoplastischen Verbundwerkstoffen, wurden besonders für Crushing-Untersuchungen entwickelt und haben den Vorteil, dass sie einen guten Hinweis auf das Crushing-Verhalten größerer Strukturen gleicher Materialien geben. Zur Berechnung der Rohrsegmente wurden gestapelte Schalenelemente für mehrschichtige Verbundwerkstoffe verwendet. Das Harzmaterial, welches ein elastisch-plastisches Materialverhalten während Crushing aufwies, wurde mit diskreten Partikeln modelliert, Klebung und Delamination mit einem Tied-Contact Algorithmus. Auch hier wurden numerische und experimentelle Ergebnisse aus Stauchversuchen verglichen. Der Vergleich erbrachte eine sehr gute Übereinstimmung der Resultate für die Aluminium-Crashrohre. Da die untersuchten Crashrohre aus dem Blickwinkel der Partikel eine geschlossene Domäne darstellen, waren die experimentell beobachteten Deformationsmoden mit Erfolg numerisch reproduzierbar. Dies wurde im Wesentlichen durch die Reproduzierbarkeit des Crushing-Verhaltens der metallischen Strukturen und ihre bekannten Standard-Materialeigenschaften herbeigeführt. Im Gegensatz dazu wiesen die Verbund-Rohrsegmente probenabhängige unterschiedliche Verformungen auf.

Chapter 1

Introduction

1.1 Crashworthiness and Impact in Aerospace Structures

The use of composite materials and their structural components in commercial transport aircraft is attractive since reduced airframe weight enables better fuel economy and therefore lowers the operating costs. Especially the application of polymeric composite sandwich structures in aerospace industry has been continuously increasing as new fibre types, resin systems, adhesives, new lightweight core materials and advanced manufacturing techniques are being developed and introduced into the market. Composite sandwich construction consists of a lightweight core material sandwiched between two stiff facings. In terms of structural efficiency, with a small additional weight in the core it is possible to produce an enhanced shell structure compared with a monolithic composite laminate, particularly under transverse and bending loads.

In aircraft structures, sandwich materials may be used in ailerons, spoilers, passenger floors and numerous nacelles and fairings. The latest commercial aeroplane projects of Airbus and Boeing, the A380 (Fig. 1.1) and the 787 Dreamliner (Fig. 1.2), respectively, show the evolutionary growth in the use of composites materials. The main structure of Airbus A380 includes 25% of carbon-fibre-reinforced plastic (CFRP) structures, compared to 15% in the Airbus A340 launched in 2002.

A critical loading case in aircraft structures is impact from birds, hailstones and foreign objects such as tyre burst, runway debris and tool or component drops. Aircraft designers need therefore reliable methods for predicting the impact damage in aircraft components. Crashworthiness and impact resistance are challenging problems directly related to structural integrity and passenger safety. The vital importance of these themes motivated researchers to concentrate on efficiently designed structures or structural components to serve the optimal performance during an operation. Since composite structures are relatively more brittle than the metallic structures their impact resistance is low due to the thin outer composite skins.

Major monolithic Carbon Fiber Reinforced Plastic (CFRP) and Thermoplastics applications

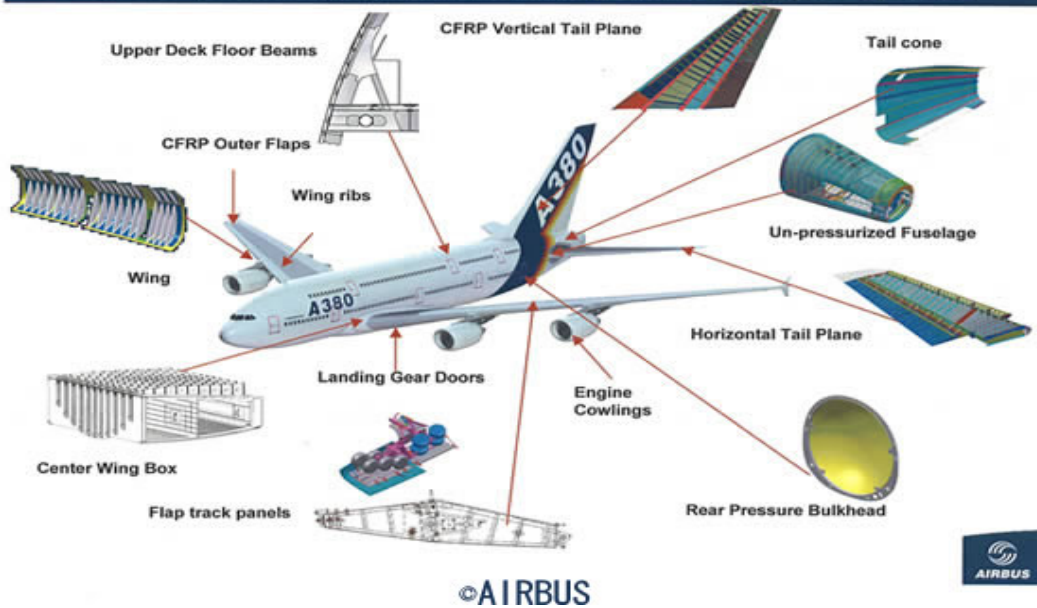


Figure 1.1: Composite parts used in Airbus 380 [1]

787 DREAMLINER Composite Solutions Applied Throughout the 787

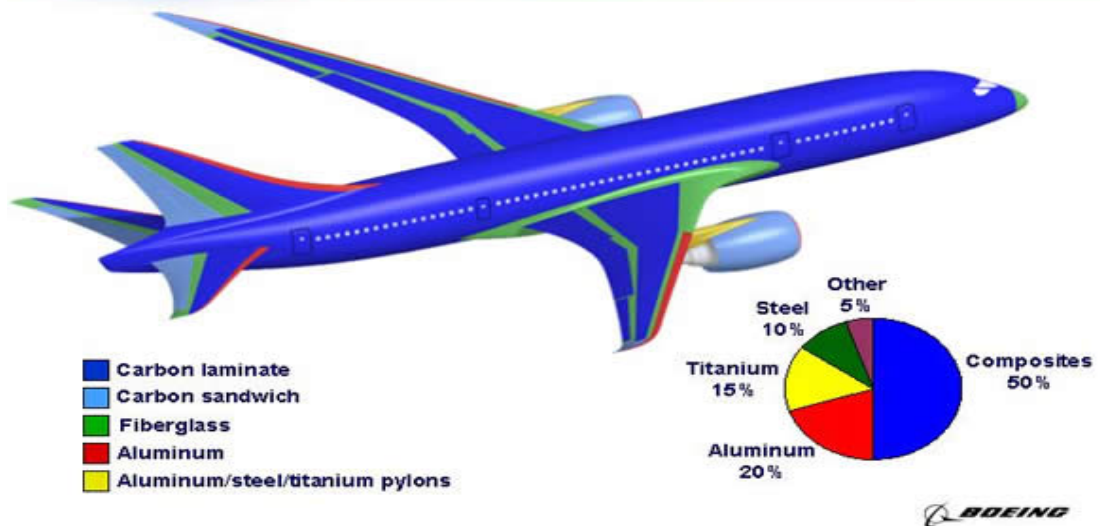


Figure 1.2: Composite parts used in Boeing 787 Dreamliner [2]



Figure 1.3: Possible impact loading cases on aircraft [3]

Laminated composite materials and sandwich structures, due to the stacking sequence of lamina, have very low stiffness and strength through the thickness direction, when compared with the in-plane properties, since no fibres may be present through the thickness. The sensitivity of laminated materials to out-of-plane loading is of prime importance and is being studied with different theoretical and experimental approaches. High velocity impact (HVI) causes surface damage that is relatively easily detected and therefore repairs may be undertaken. Low velocity impact can produce damage that is difficult to observe visually. Fig. 1.3 shows an overview of the most common impact scenarios.

When composite skin laminates are subjected to impact by a projectile, many fracture processes, with their associated energy absorbing capacities, can occur such as matrix cracking, fibre matrix debonding, delamination and fibre failure. Delamination is caused by the debonding of two adjacent plies of the laminate. In aeronautical applications, composite plates are sensitive to impact, a delamination occurs readily in composite laminates in impact. Delamination can cause significant reduction of structural integrity, especially in terms of strength and stiffness which often leads to catastrophic failure without advance warning. If the composite structure is subsequently loaded in compression, delaminations are likely to grow in various propagation modes and eventually cause structural failure by buckling.

Many composite components have curved shapes, tapered thickness and plies with

different layups, which will also make the delamination grow in a mixed-mode that depends on the extent of the initial crack. Therefore, delaminations in composite laminates generally grow under mixed-mode conditions. Interaction of failure modes and the effects of fibre type and layup, the matrix fibre resin bond and environmental effects result in complex failure modes. After fracture of the skin in sandwich structures an impacting projectile may damage and penetrate into the core. Low velocity impacts such as tool drop in which a large object falls onto the structure with low velocity during maintenance is an important concern, since these impacts can cause delamination damage which may be barely visible. The detection of such damages is difficult during routine inspections. The resultant damage may reduce the residual strength of the structure drastically. Low velocity impacts may induce localised deformations in sandwich structures. Most common damage mechanisms are fibre breaking, resin cracking, face sheet-core delamination, core crush, puncture etc.

For relatively low velocity projectiles, a sandwich panel may respond by bending and no damage occurs if the energy of the projectile can be accommodated by the elastic strain energy in the panel. HVIs are defined when the ratio between impact velocity and the velocity of compressive waves propagating through the thickness is larger than the maximum strain to failure in that direction. This implies that damage is introduced during the first few travels of the compressive wave through thickness when overall structural motion is not yet established. At higher impact velocities a critical condition is reached when a local contact stress exceeds a local material strength, which may be a laminate bending strength, core compression strength or interface delamination strength. Thus in order to improve durability and damage tolerance of sandwich structures, a structural analysis of skin, core and interface damage should be addressed within the design process.

Another important concern for the aircraft designer is the absorbed crash energy associated with the vertical component of the crash velocity, since significant energy from the horizontal component may be absorbed by friction during aircraft sliding on soil or water surfaces. Emphasis therefore is given on energy absorbing structures which absorb the vertical component of the impact energy. In the area of crashworthiness, an energy absorbing component is design to absorb the crash energy occurring in a controlled progressive manner. The loads on occupants should be minimised during a crash event (Fig. 1.4). However the type of aircraft affects the crashworthy design approach which is an optimisation process for a certain aircraft category. Small passenger airplanes and helicopters have very limited crushable airframes (ca. 200mm). Therefore the design of sub-floor elements such as bulkheads and beams is a key issue for the crash safety of these structures. Beside new designs, combinations of new materials are extensively used in aerospace structures.

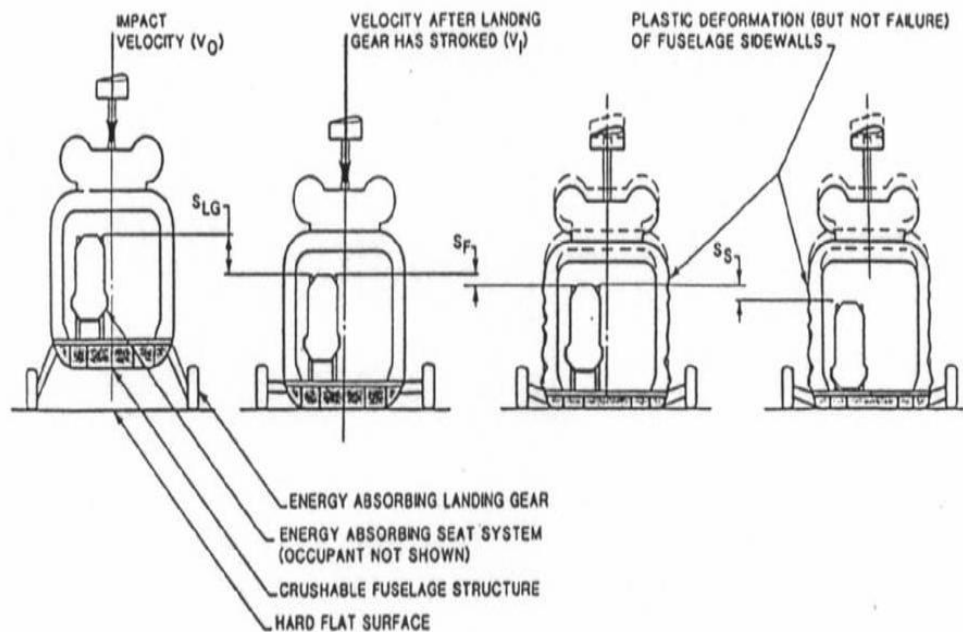


Figure 1.4: Energy absorption sequence during vertical crash of a crash-resistant aircraft system [4]

Concerning absorption of crash energy, composite designs show better mass specific performance than structural designs made of metal due to their high EA capabilities and lower density. Metallic energy absorbers absorb energy by plastic deformation and progressive folding failure modes. The folding pattern of the shell is governed by the processing buckling mode, which is dependent on the shell geometry and the dynamic loading conditions. High EA capability can be achieved in composite tubes and cones under axial compressive loads where brittle fracture and fragmentation of the composite into sub-laminates occurs. The fracture mode of polymer composite materials is progressive crushing, which proceeds under a high constant load. In progressive crushing of a tube, the failure often starts from a chamfered tube end and the crush zone propagates along the tube. The crushing energies are absorbed by the combination of various fracture mechanisms such as cracking, delamination and fibre fracture. Therefore the crushing of composites is complex, for example composites can crush by brittle fracturing, lamina bending and also in a progressive folding mode. The ideal progressive crushing mechanism in composites is therefore a balance between brittle fracture and lamina bending as this imparts the high EA. Such complex crushing mechanisms require careful design of the composite crush structures, and a significant amount of testing is therefore required to validate designs.

1.2 Industry Requirement

The understanding of composite structural components under static and dynamic loading conditions is extremely important for the further development of these structures. In order to reduce the development and certification costs, computational methods can be used to predict structural integrity under crash and impact loads. The development of software tools that can be used to predict the resulting damage from impact and crash which are directly related to the structural integrity and safety requirements of engineering structures is of interest to aircraft manufacturers. Despite extensive research and development of composite structures, their responses under static and dynamic loadings are still not fully understood. Although experimental tests under impact conditions provide considerable information about the tested specimen and their characteristic parameters, the deep understanding of the dynamic properties and failure behaviour of composite structures require test programs which are complex, destructive, time consuming and consequently expensive for industry.

Since aerospace industry demands reduced development and operating costs, there is strong interest in "Virtual Testing" to introduce simulation technology into testing technology aiming at "**Less Structural Test**" (complex, expensive and not very reproducible), "**More Material Test**" (relatively easy, cheap and generally reproducible). Impact of high velocity objects on aircraft structures is a damage scenario that must be evaluated during the development and certification of an aircraft. In every development phase of a new aircraft, an extensive and costly campaign of impact tests must be performed, in order to comply with certification requirements and ensure high standards of safety. The so-called discrete damage is part of the damage tolerance of the aircraft structure, together with the fatigue and corrosion, as required by regulations. That means that for all regions where foreign impact objects may represent a threat to the aircraft airworthiness, a substantiation procedure to show compliance with certification requirements becomes necessary. For example structural integrity after bird strike, which is one of the possible sources of impact, should be verified in numerous specific primary structure locations on wing leading edges and the front cockpit.

Beside the continuous development of new materials used in aerospace industry, new concepts and designs, the development of the existing computational methods and the establishment of new ones are important current themes. Validated finite element (FE) simulation tools are essential for the industry to reduce the development cycle in order to keep up with international competitors, since crash and impact tests on large aircraft structures are becoming too expensive to carry out at the development stage. If the behaviour of structures or components can be represented in a more realistic way, it can lead in the near future to a significant reduction in the number of tests that are

presently performed. Parallel to the increasing application of composite materials and composite structural components, the complexity of the new designs, demand for faster validation and certification processes requires continuous enhancement of these design analysis methods.

Therefore the main objective of the thesis is to develop improved failure models and associated numerical modelling techniques for simulating the failure of fibre-reinforced composite materials under dynamic crash and impact loads.

1.3 Plan of the Thesis

This thesis is divided into 6 chapters:

Chapter 1 has given an introduction into the importance of crashworthiness and impact in the aerospace industry, energy absorption (EA) phenomena and energy absorbing structures. Additionally it sets out the demand of industry concerning reduced development and operating costs and faster certification procedures.

Chapter 2 gives a more detailed literature review of crashworthiness and impact on aerospace structures and EA phenomena and energy absorbing structures.

Chapter 3 reports on the state-of-the-art of numerical modelling of crash and impact mechanisms and discusses the limitations of current Finite Element Method (FEM) based numerical tools such as time consuming mesh discretisation, element distortions which occur during large deformation, difficulties to simulate the damage and fracture of brittle materials with fragmentation failure modes. This is followed by an introduction to the alternative numerical "Meshless Methods". It also describes the theory of particle-based meshless methods such as Smooth Particle Hydrodynamics (SPH) Method and Discrete Element Method (DEM).

Chapter 4 points out the need concerning "coupling" in numerical models and focuses on the theory of several coupling methods, between classical FEM and meshless methods, proposed in the literature to maintain consistency and stability and to improve the efficiency of the meshless methods. Chapter 4 following the idea of "coupling" also focuses on "Direct Coupling" and "Semi-Adaptive Coupling (SAC) Technique". This chapter sets out the principles of abovementioned coupling techniques and illustrates the applicability of the proposed methods by means of benchmark simulations.

Since the main objective of the thesis is to develop improved failure models and associated numerical modelling techniques for simulating the failure of fibre-reinforced

composite materials under dynamic crash and impact loads, Chapter 5 shows the application of coupling techniques in material characterisation, such as compression behaviour of aramid paper honeycomb (Nomex) and polyetherimide (PEI) and high velocity impact (HVI) simulations on sandwich panels.

Chapter 6 shows how the techniques may be applied to model the crush behaviour of metal and composite energy absorbers, respectively. Although Chapter 5 and 6 focus on the numerical simulation, the results are also compared with the conducted experimental investigations.

Finally the conclusions which arise from the presented study were drawn.

Chapter 2

Literature Review

This chapter gives a literature review on crashworthiness and impact in aerospace structures with discussion of EA phenomena and energy absorbing structures. Some of the reviewed works here also consist of numerical investigations. Since the chapter aims at giving a brief overview about the conducted investigations, the details of the numerical works are not discussed here but referred to Chapter 3.

2.1 Energy Absorption and Energy Absorbing Structures

Crashworthiness and impact resistance are challenging engineering problems directly related to structural integrity and passenger safety. European Community Road Accident Database [5] has shown that the number of accidents in Europe has the same trend between 1991 and 2003 with the number of injuries remaining almost the same. However, the number of casualties decreased approximately 30%, showing an effective and increased use of passive protection safety systems (seat belts, airbags and etc.) and the active protection safety systems (sensors, anti-lock brakes and etc.). The vital importance of the crashworthiness in vehicles has motivated researchers to concentrate on the designing of novel structural components made of metallic and composite materials that are capable of absorbing the crash energy in a controlled manner.

Metal Crush Absorbers

Columnar structures including square and circular metal tubes are the examples of such components progressively absorb the large amount of crash energy through plastic structural collapse. It was first shown by Alexander [6] in 1960 that tubular structures under axial loads absorb the deformation energy almost at a constant load. He modelled analytically the concertina mode of deformation based on the plastic work required for bending and stretching of extensible thin cylinders. The fairly constant load is the result of the progressive folding which is a desired deformation mechanism from an efficient energy absorbing component. Since Alexander, many experimental and numerical investigations have been conducted aiming at determining and under-

standing the crushing behaviour of tubular structures and some of these have been recently reviewed by Alghamdi [7]. Among them, Andrews et al. [8] focused on the classification of the deformation modes as a function of the material properties, geometry and geometrical parameters such as diameter, wall thickness and length, of the crash tube absorber. They investigated the relation between the deformation mode and wall thickness/diameter and length/diameter ratios, see Fig. 2.1. They conducted crush tests on several tube samples with changing diameter, wall thickness and length and classified the crushing mode of the cylindrical tubes in seven groups:

1. **Concertina:** Axisymmetric and sequential or progressive folding starting at the end of the tube.
2. **Diamond:** Axisymmetric but sequential or progressive folding starting at the end of the tube.
3. **Euler:** Bending of tube as a strut.
4. **Concertina and 2-lobe and/or 3-lobe diamond (Mixed):** Folding first in the concertina mode changing to diamond configuration.
5. **Axisymmetric/concertina:** Simultaneous collapse along the length of the tube, axisymmetric single or multiple barreling of the tube.
6. **2-lobe diamond:** Simultaneous collapse along the tube in the form of the 2-lobe diamond configuration.
7. **Tilting of tube axis:** Shearing of tube on the platen surface in the form of the 2-lobe diamond configuration.

Abramowicz and Jones [9]- [11] and Wierzbicki et al. [12] modified the Alexander's model and proposed the average crushing load equations for the concertina mode of deformation. Pugsley and Macaulay [13] investigated the diamond mode of deformation of thin cylindrical columns having large diameter/wall thickness ratios. The deformation energy was assumed to be absorbed by plastic bending and shear of the diamond pattern and they proposed an equation for the average crushing load for diamond mode of deformation. Abramowicz and Wierzbicki [14] also addressed the same problem and gave an approximate expression for diamond mode deformation. Abramowicz and Jones [15] developed an expression for the mean crush force for the same deformation mode.

The filling of tubular structures with lightweight foams for a goal of increasing specific energy absorption (SEA) has also taken considerable interest. One of the earliest investigations on the crushing behaviour of thin-walled sections filled with lightweight

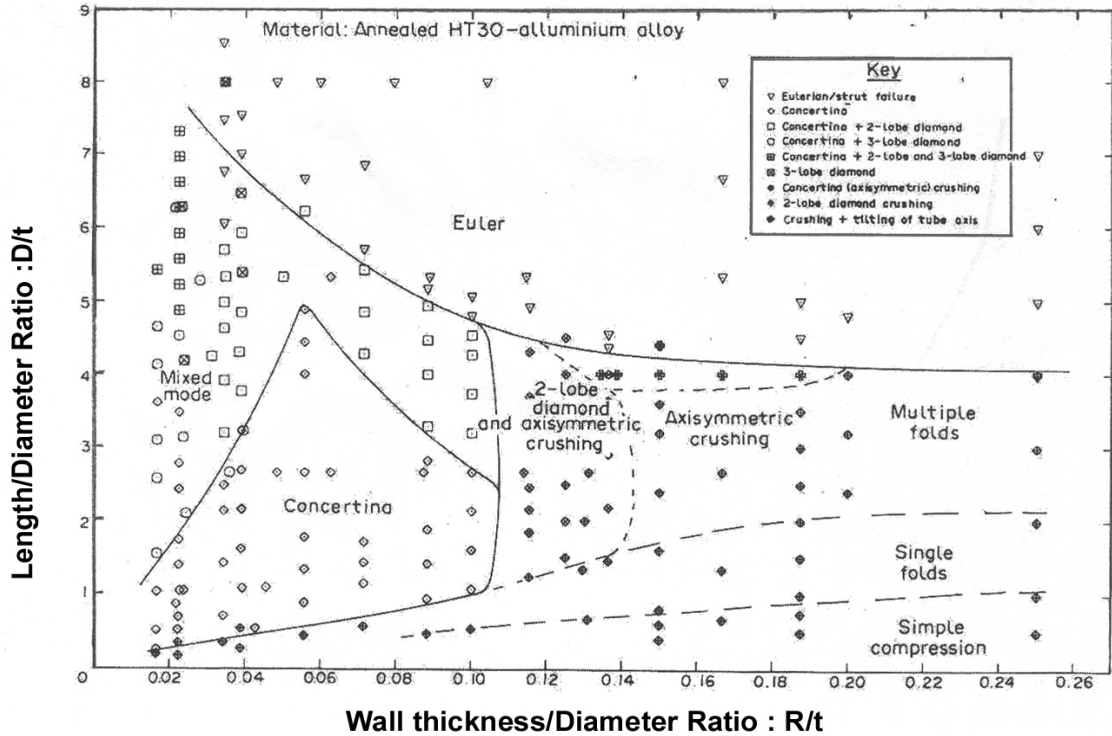


Figure 2.1: Classification chart for collapse modes and aluminum (Al) alloy tubes under axial compression [8]

polyurethane (PU) foam was conducted by Thornton [16], who pointed out that although noticeable increase in SEA was possible with foam filling, it was not weight effective when compared with the thickening of an unfilled tube wall. Lampinen and Jeryan [17] investigated the crushing of sheet metal tubes filled with low density PU foams and concluded that foam filling stabilizes the deformation of thin-walled tubes. The crushing behaviour of PU foam-filled thin-walled metal tubes was also investigated by Reid et al. [18], at quasi-static and dynamic deformation rates. It was concluded that tube wall interacts with the foam filler resulting in a greater tendency for the axisymmetric mode of deformation. They also concluded that the simple addition of the uniaxial foam contribution to the tube wall folding contribution gave the total average crushing load of a foam-filled tube. Guillow et al. [19] have recently pointed out that the average crushing loads of PU foam-filled Al thin-walled tubes were greater than the sum of the average crushing loads of empty tube (alone) and foam (alone), a result which contrasted with those of Reid et al. [18] and Reddy and Wall [20]. Seitzberger et al. [21] investigated the crushing behaviour of Al closed-cell foam-filled monotubal and bitubal arrangements of square, hexagonal and orthogonal cross-sections and concluded that mass related average load level can be improved by filling tubular members with Al foam. It was also pointed out in the same study that suitable foam vs. tube selection was important for the designing of efficient crush elements. Santosa and Wierzbicki [22]

investigated the crushing behaviour of Al honeycomb- and foam-filled box columns both numerically and experimentally and showed that the effect of filler on the tube crushing load was similar with the strong axis of the honeycomb along and normal to the compression axis, proving that both axial and lateral strength of the filler were effective in increasing the crushing load of the tube. Further, Santosa et al. [23] noted that the bonding between filler and tube wall increased the average crushing load of filled tubes over the unbounded filled tube when appropriate tube geometry and foam density were chosen. They also showed, both experimentally and numerically, that the strengthening of foam-filled tube average crushing load was 1.8 and 2.8 times of Al foam filler plateau load for the unbounded and bounded cases, respectively. Børvik et al. [24] noticed that during a crash event the crushing load was neither pure axial nor pure bending but rather a combination of two and conducted a series of axial and oblique quasi-static loading tests on the empty and Al foam-filled tubular columns. It was shown by the same authors that the peak load and EA decreased strongly with increasing loading angle.

Novel geometrical designs including the filling of tubular structures with lightweight metal and polymer foams have recently been taken considerable interest. Santosa et al. [23] investigated the axial crushing behaviour of lightweight Al foam- and Al honeycomb-filled square box columns at quasi-static rates. It was found that although honeycomb filling of box columns was more weight efficient in compression, it was less efficient than Al foam filling in compression-bending loading. A study on the bending collapse of thin-walled prismatic columns filled with Al foam and Al honeycomb further showed that columns filled with honeycomb and foam were more efficient in terms of SAE than the thickening of the column wall [25]. Kim and Wierzbicki [26] investigated the large planar and biaxial bending rotation response of square cross-section thin-walled beams partially and fully filled with Al foam. The characteristics of moment-rotation responses of the beams were investigated under cantilever bending and found to vary with the length of foam fillers. Kim [27] conducted crushing tests on an Al foam-filled front side rail and a sub-frame structure of a passenger car and showed that foam filling increased the EA efficiency. Chen and Nardini [28] investigated crushing behaviour of closed-top-hat foam-filled Al sections, including single-top-hat, double-top-hat and double-top-hat with a center plate. It was concluded in the same study that the thin-walled foam-filled members could be used as efficient crash energy absorbers. Seitzberger et al. [21], [29] investigated the axial crushing of foam-filled square, hexagonal, octagonal and bitubular steel tubes. It was reported that considerable improvements with respect to EA were obtained with foam filling particularly in bitubular configurations. Chen and Wierzbicki [30] studied the axial crushing of hollow multi-cell columns. The enhancement in the total crushing resistance of the columns increased, depending on the interaction between the foam filler and the column wall,

by the amounts of 140% and 180% of the foam filler strength for double- and triple-cell columns, respectively.

Although the effects of several fillers on SAE have been studied, the honeycomb filling has not been as extensively studied as other filler types. Santosa and Wierzbicki [22] investigated the axial crushing behaviour of Al honeycomb- and Al foam-filled box columns. They showed that the filling of box columns with Al honeycomb can be preferable to thickening of the column wall. They developed simple formulae for the relationship between mean crushing force and the strength of the filler. Additionally they found out that the presence of adhesive increases the EA compared to unbounded filling of the columns. In case of unidirectional loading Al honeycomb filling showed better crashworthy performance than the Al foam filling. In their extended study [25] they investigated the bending collapse of the filled columns. They concluded that the filling of columns with low density materials such as Al foam or Al honeycomb enhances the bending strength. Additionally the presence of adhesive results in higher bending response. In terms of SAE both filled designs showed better performance than the thickening of the column wall. Santosa and Wierzbicki [31] also investigated a novel double-wall sandwich column concept for axial crushing. The column consisted of lightweight Al foam and inner and outer shells made of Al in a sandwich design. They concluded that the double-wall sandwich column showed better crash performance than the single wall columns for the same weight. Later they focussed on the Al honeycomb- and Al foam-filled double-wall columnar structures and obtained 40-60% and 35-40% weight saving, respectively. Al honeycomb-filled double-wall designs show better performance depending on their relatively lower densities. Finally it was proven that the double-wall columns were an effective structural element for the axial crushing. A recent study on the honeycomb filling has been published by Zarei and Kröger [32]. They investigated the axial and oblique impact crash response of empty and Al honeycomb-filled square tubes. In the first part of their study they investigated the EA capability of several empty tube geometries including square, rectangular and circular tubes. Using Multidisciplinary Design Optimization (MDO) they aimed at maximizing the EA and the SAE. They concluded that the empty circular tubes have the best crashworthy response. In the second part of their study they concentrated on the crash response of honeycomb-filled circular tubes. Optimisation process has also been repeated for the second part of the study. They concluded that the honeycomb filling of tubes is an alternative way of increasing the EA capacity of the empty tubes instead of thickening the tube wall. The same results have been reported in the case of foam filling of Al tubes by Wierzbicki and Santosa [25].

Composite Energy Absorbers

Composite energy absorbers absorb crash energy by multiple fracture and fragmentation of the fibres. Due to the brittle nature of the fibres and thermoset resins, the composite crush behaviour tends to brittle fracture. Hull [33] defined the crushing deformation mode of the composite tubes under axial compression as:

1. **Euler Buckling:** Failing by buckling before the onset of any other failure mechanism. Euler buckling gives very low EA capacity.
2. **Shell Wall Buckling:** Progressive folding involves the formation of successive local buckles such that the tube folds axially in a manner similar to concertina.
3. **Brittle Fracture:** The overall failure mode will be one of the stable crushing with high levels of energy.

The brittle fracture mode is also called as high-energy-mode. Hull [33] and Farley and Jones [34] extended the brittle fracture into two sub-deformation mechanisms. Splaying (Hull) or lamina bending (Farley and Jones) mode is characterised by very long interlaminar, intralaminar and parallel-to-fibre cracks with little or no fracture of the axial lamina bundles, as shown schematically in Fig. 2.2. Beside crack growth which is the principal EA mechanism, the energy is also absorbed by bending response and frictional effects. The fragmentation (Hull) or transverse shearing (Farley and Jones) mode is characterised by a wedge-shaped laminate cross-section, with one or more short interlaminar and longitudinal cracks forming partial lamina bundles. The primary EA mechanism is fracture of the lamina bundles, with interlaminar and longitudinal crack growth as secondary contributors. Farley [35] and Hamada et al. [36] concluded that the fragmentation generally absorbs more energy than the splaying mode. Although most of the investigated structures were tubular conical shells were also investigated intensively [37]- [40]. Thornton and Edwards [41] report that square and rectangular tubes are generally less effective at absorbing energy than circular ones. These findings are supported by Mamalis et al. [38]. Similarly, Kindervater [42] reports that square and rectangular tubes have respectively 0.8 and 0.5 times the SAE of comparable circular specimens. This is generally attributed to the fact that corners tend to act as stress concentrators, leading to the formation of splitting cracks there. These splits tend to dominate the failure mechanism resulting in poor utilisation of the material as a whole. There are many research studies in fibre-reinforced plastic tubes made of unidirectional composites, knitted composites, sheet moulding compound (SMC) and other material systems and their effects on general behaviour, on environmental temperature, testing speed, geometries as a function of SAE have been discussed in detailed [43]- [49].

Thornton investigated the axial collapse of circular tubes made of carbon-, Kevlar-

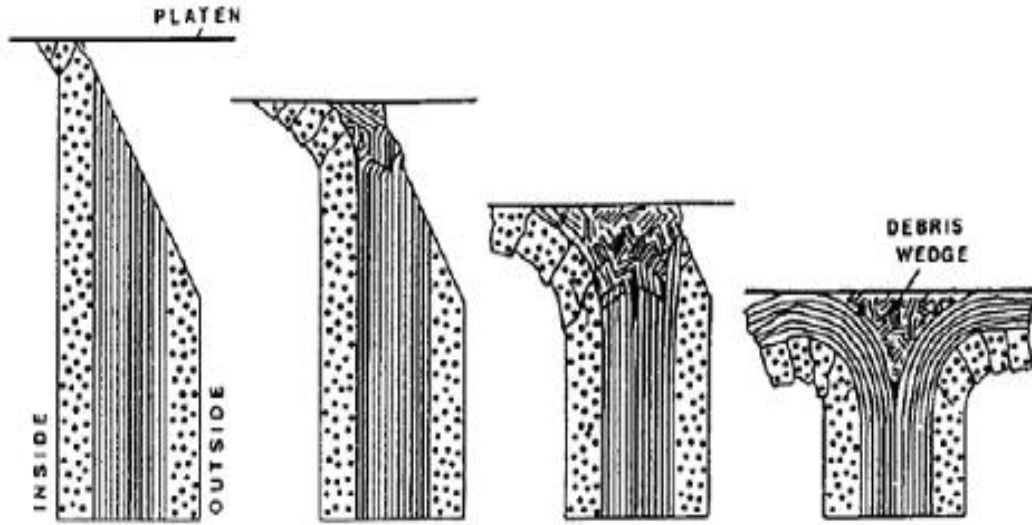


Figure 2.2: Schematic representation of the formation of the splaying/lamina bending mode crush zone based on macroscopic examination [33]

and glass-fibre-reinforced composite materials [50]. He also proposed a trigger mechanism to prevent catastrophic failure of brittle composite structures and to induce stable and progressive crush. The end modification or trigger of the composite tube creates a region of high stress from which stable crushing is then propagated. Triggers which have been shown to work well include chamfers (as in Figs. 2.2 and 2.3), slots, and especially tulip geometries. Czaplicki and Robertson [51] investigated the crushing behaviour of E-glass/polyester and E-glass/vinyl ester pultruded tubes. They used two different kinds of trigger, namely bevel and tulip. With the tulip trigger almost a double SAE value has been reached. Additionally they concluded that the crushing was more controlled and predictable. Crushing over metal dies or cones is another way of triggering stable collapse [43].

The failure of a composite profile under axial compressive loading occurs usually in catastrophic brittle failure unless triggered to initiate progressive triggering. The triggering mechanism consists mainly of machining a special geometry on one of the ends of the profile. If the required failure mode of the structure is not triggered the peak load occurs before the crushing is established. A high peak load results in high accelerations under dynamic loads which are undesirable. Therefore the triggering is a very important issue for the EA of the composite materials. Thuis and Metz [52] investigated two different laminates and triggers for the crashworthy composite cylinders made of hybrid carbon/aramid fabric. They concluded that the cylinders which failed in splaying mode can absorb more energy than the cylinders which failed in fragmentation. They also pointed out that the trigger configuration affects the failure mode of the composite energy absorbers. They obtained the highest EA capability with the chamfer type trigger. Later Jiménez et al. [53] also investigated the effect of trigger

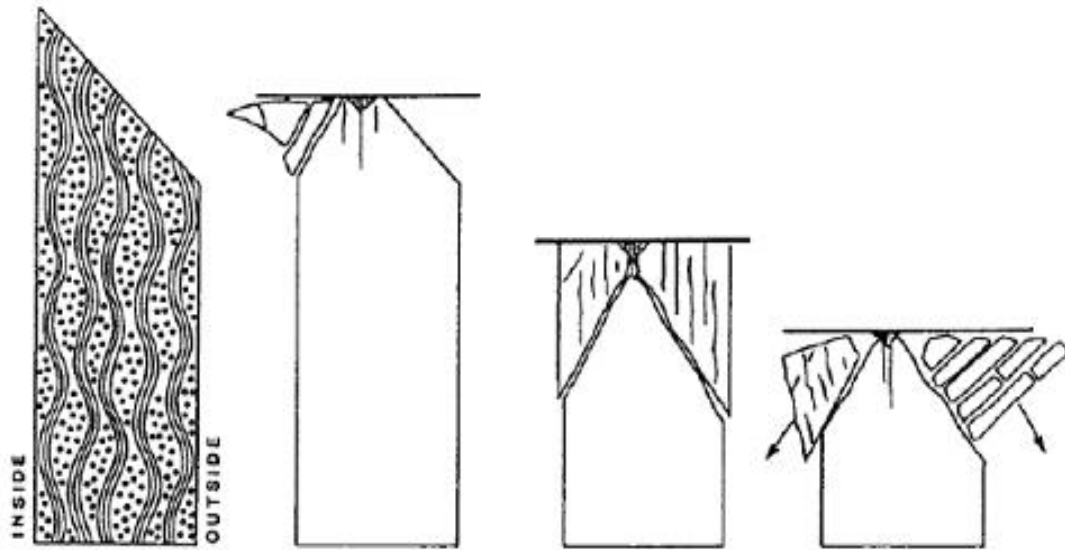


Figure 2.3: Schematic representation of the formation of the fragmentation/transverse shearing mode crush zone based on macroscopic examination [33]

on unidirectional box sections made of E-glass/polyester pultrusion. They concluded that the trigger geometry has a very big influence on the results. When the bevel type trigger used different bevel angles the SAE may vary ca. 25%. As mentioned above the friction mechanism can contribute to the EA capability of the composite energy absorber. Fairfull and Hull [54] investigated the energy absorbed by the frictional process associated with the axial compression. Both the frictional effects within the crush zone of the material and those caused by the crushed composite sliding across the test plates were considered. They concluded that the frictional process can account for more than 50% of the total energy absorbed by the progressive crushing.

Later Mamalis et al. [55] reviewed the investigations on the crashworthiness of composite structures. In order to enhance the crashworthy capability of composite structures Harte et al. [56] suggested the foam filling of the braided tubes made of glass fibre/epoxy with polymer foam cores. They optimised the SAE with respect to relative density and geometry. They concluded that the foam-filled braided tubes exhibit higher SAE capability than the combination of the composite tube and the polymeric foam core.

Metallic-Composite Energy Absorbers

In order to enhance the EA of the composite crash absorbers hybrid designs were also investigated intensively. Some of these hybrid designs consisted of metal and composite tubes or hybrids of different types of composite materials. Farley [57] studied the EA capability of carbon fibre/epoxy composite material and glass fibre/epoxy composite

material and carbon fibre/epoxy composite material and Kevlar/epoxy composite material.

Shin et al. [58] investigated the EA capability of axial crush and bending collapse of Al/glass-fibre-reinforced plastic (GFRP) hybrid tubes with different ply orientations. They found out that in axial crushing the hybrid tube with 90° fibre orientation to the tube axis showed the best EA capability among all designs studied. During crushing composite plies prevented the Al tubes from folding. The failure of the hybrid tube was stable and progressive without any trigger. In case of bending collapse, the hybrid tube which consists of an Al tube with $0^\circ/90^\circ$ ply orientation composite tube showed the best performance. The hybrid tube showed the effect of interaction between the Al and composite tube since the EA capability was higher than the sum of each individual.

El-Hage et al. [59] produced hybrid tubes containing Al tubes and a filament-wound E-glass-fibre-reinforced/epoxy overwrap and observed that the hybrid tubes have significantly higher EA than either the composite tubes or the Al tubes. Song et al. [60] performed quasi-static and impact tests on E-glass/epoxy wrapped circular Al, steel and copper tubes. Babbage and Mallick [61] investigated the static axial crushing behaviour of empty and epoxy foam-filled Al/filament-wound E-glass-fibre-reinforced/epoxy composite tubes. The composite overwrap increased the peak-load, average crushing load and SAE values of Al square and circular tubes. Epoxy foam filling of round Al/composite hybrid tubes further improved the axial crush performance of the empty circular hybrid tubes, while foam filling of square hybrid tubes resulted in the failure of Al tube either via buckling or tearing at the corners due to the prevention of tube inward folding by the foam filler. Güden et al. [62] studied the effect of Al closed-cell foam filling on the quasi-static crushing behaviour of an E-glass woven fabric polyester composite tube and thin-walled Al/polyester composite hybrid tube. For comparison, empty Al, empty composite and empty hybrid tubes were also tested. Empty composite and empty hybrid tubes crushed predominantly in progressive crushing mode, without applying any triggering mechanism. Foam filling was found to be ineffective in increasing the crushing loads of the composite tubes over the sum of the crushing loads of empty composite tube and foam. However, foam filling stabilised the composite progressive crushing mode. In empty hybrid tubes, the deformation mode of the inner Al tube was found to be a more complex form of the diamond mode of deformation of empty Al tubes, leading to higher crushing load values than the sum of the crushing load values of empty composite tube and empty metal tube. The foam filling of hybrid tubes however resulted in axial splitting of the outer composite tube due to the resistance imposed by the foam filler to Al tube inward folding and hence it was ineffective in increasing crushing load and SAE values over those of empty hybrid tubes.

2.2 Crashworthiness and Impact in Aerospace Structures

As stated in Chapter 1 composite sandwich structures are attractive for large integral low weight shell structures under transverse and bending loads. An important drawback of aerospace structural sandwich components is their relatively low resistance to impact damage due to the thin outer composite skins. Most common damage mechanisms in composites, such as matrix cracking, debonding and fibre failure, may appear individually or interact, resulting in complex skin failure modes under impact. After fracture of the skin, the impacting object may damage and penetrate into the core. If impact speed is low, sandwich panels may respond by bending and little damage occurs if the kinetic energy of the impacting object is accommodated by the elastic strain energy level of the panel. At higher impact velocities a critical condition is reached when local contact stress exceeds local strength, leading to laminate bending failure, core/skin interface delamination and core compression strength failure. Core deformation and failure are therefore decisive factors for the EA capability of sandwich panels. Although the major damage mechanisms such as matrix cracking, debonding and fibre failure may appear individually, their interaction and the effects of fibre type and lay-up, distribution and geometrical nature, additionally the type and state of the matrix fibre resin bond and environmental effects result in complex failure modes. Despite extensive research and development of sandwich structures, their impact response is still not fully understood.

A review by Abrate [63] demonstrated the recent research efforts aimed to understand the impact response of the sandwich structures. Rhodes [64] conducted impact tests on a range of systems and showed that the enhancement in the strength of the core material can serve to increase the impact resistance of the sandwich panel. Mines et al. [65] investigated the impact response of the polymer composite sandwich structures with Al honeycomb core. They showed that the impact energy of the projectile is mostly absorbed by the localised impact damage zone around the point of the impact. They also concluded that the perforation resistance of these structures increases with the strain rate. Charles and Guedra-Degeorges [66] showed that the dent depth around the impact point increases with impact energy until a maximum value is reached. Cantwell et al. [67] pointed out that during a low velocity impact event the skin shearing was the primary EA mechanism under localised impact conditions. Abrate [68] defined an energy-balance model in which the impact energy of the projectile is defined as the summation of the energy stored in bending and shear deformations and the energy used to create the local deformations (skin and core) in the impact zone. Hazizan and Cantwell [69] developed and applied an energy-balance model similar to Abrate to predict the impact response of a foam-based sandwich structure. They varied the impact energy of the projectile and the mechanical properties of the foam core to investigate

the accuracy of their model. They concluded that the dynamic response of the sandwich structure depends on the elastic properties of the foam core material. They also showed that the energy-balance model based on the dissipation of the impact energy during impact is effective to predict the low velocity impact response of sandwich structures in the elastic regime. Raju et al. [70] pointed out that the small coupons used in the material characterisation test for composite materials do not behave the same way as the large structures made of these materials. They focussed on the in-plane dimensional effect and thickness effect of the composite plates. They found out that the thickness effect is much more significant than the in-plane dimensional effect.

Beside the efforts to have a better understanding of the deformation mechanisms mentioned above several researchers studied the effect of impactor on impact damage. Among them, Horigan et al. [71] investigated the impact response of sandwich structures with glass-fibre-reinforced/epoxy skins. They showed that the hard projectile results in deeper and more severe damage than the soft projectile. Cantwell and Morton [72] studied the effect of impactor mass on the impact force and the resulting damage area for low velocity impacts. They showed that the damage initiation energy increases with an increase in the impactor mass. Ambur and Kemmerly [73] investigated the effect of impactor mass on the low velocity impact response of the laminated composite plates. They pointed out that the damage area is a nonlinear function of the impactor mass. Beside impactor mass the shape of impactor is also an important factor on the impact response. Mitrevski et al. [74] investigated the effect of impactor shape on low velocity impact of composite thin plates. The observations show that the specimen impacted by the conical impactor absorbed most energy as a result of the depth of local penetration. The hemispherical impactor produced the highest peak force and the shortest impact duration.

Laminated composite materials and sandwich structures, due to the stacking sequence of lamina, have very low stiffness and strength through the thickness direction, when compared with the in-plane properties, since no reinforcing are usually present through the thickness. One strategy of achieving this is to add reinforcement pins to the foam core, with the ends of the pins embedded in woven carbon fibre face sheets. This construction technique gives excellent bonding of the pins to the face sheets, and thereby increases the delamination strength and toughness between face sheets and core. The improved through-thickness properties have been demonstrated in a number of preliminary experimental investigations. For example, low velocity impact experiments on composite skin sandwich panels with foam cores reinforced by metallic pins indicate that these sandwich structures over improved impact and delamination resistance [75]-[79]. C artie and Fleck [80] studied the titanium and carbon fibre pins inserted into the polymer foam core of a sandwich panel in order to increase the through-thickness

strength. They showed that the foam core stabilizes the pins against elastic buckling and the pin-reinforced core has a strength and EA capacity in excess of the individual contributions from the foam and unsupported pins. The pin reinforcement increased the stiffness, strength and EA of the conventional foam material.

Chapter 3

Numerical Modelling of Crush and Impact Mechanisms

Currently there are several numerical methods used to analyse the response of engineering structures to applied loads. The most common numerical methods are:

- **Finite Difference Method (FDM)** is where the derivatives of the local operator in the field equations are replaced by finite differences using so-called finite difference "stars" over neighbouring grid points.
- **Finite Volume Method (FVM)** starts from the weak form (energy, functional) of the field equations; the weight functions are selected in such a way that only a boundary integral over a cell or patch has to be evaluated. Most often used in Computational Fluid Dynamics (CFD).
- **Finite Element Method (FEM)** is based on the weak form, mostly as Galerkin Method where the trial and test functions are taken from the same function space and restricted to a local area, named finite element (FE).
- **Boundary Element Method (BEM)** uses fundamental solutions satisfying the domain equations and restricts the approximation to the boundary terms thus reducing the discretisation order by one.
- **Meshless Methods** are usually based on the weak form where the field is approximated over a certain meshless area using random controlling points.

Among these methods the classical numerical methods such as FEM, FDM or BEM solve partial differential equation (PDE)s of continuum mechanics; hence, they can consider only a small number of discontinuities and cannot encompass the processes which involve discontinuous states such as fracture and fragmentation of materials. FEM is a well-suited numerical tool to take into account the complexity of the geometries, the nonlinear behaviour laws and the contact modelling in the study of such problems. The Lagrangian algorithm is in its essence relatively simple and well-suited for impact

problems between solids. But it has drawbacks when the mesh is subjected to large deformations and distortions. Remeshing is thus required during the computation. The Eulerian or Eulerian-Lagrangian formulation helps avoid these large distortions but is more difficult to set up and presents difficulties when the boundary conditions are of Lagrangian kind. As an alternative to FEM, Meshless Methods have been developed and applied to numerical simulations involving extensive material flow and fracture. Meshless Methods replace FEs by a set of nodes or particles within the problem domain as well as sets of nodes scattered on the boundaries of the domain to represent the problem domain and its boundaries.

This chapter reports on the state-of-the-art of numerical modelling of crash and impact mechanisms and discusses the limitations of current FEM-based numerical tools such as time consuming mesh discretisation, element distortions which occur during large deformation, difficulties to simulate the damage and fracture of material into a large number of fragments and gives an introduction about the alternative numerical class "Meshless Methods". It also contains theory of particle-based, meshless methods such as SPH Method and DEM.

3.1 Finite Element Method

State-of-the Art

The most popular numerical method FEM is well-established numerical technique, which has been used to obtain numerical solution of various problems in the area of engineering and science. Currently several well-developed FEM software packages are commercially available. For crash and impact simulations FEM dominates. The current modelling approaches using FEM for the structural crash and impact problems being considered in this thesis are listed below:

Modelling Metallic Crash Absorbers

- For the modelling of the thin-walled tubes shell elements which represents the middle surface are used.
- The compression plates for loading tube structures are modelled using solid elements and are assumed to be rigid.
- For the material modelling elastic-plastic material models for Al and steel are selected.

- In case of filling such as Al foam filling the filler material is modelled with solid elements.
- Since fillers such as Al foam and honeycombs are discontinuous materials the homogenisation technique is applied. The material response of this inhomogeneous material is replaced with a homogenised material with the same effective properties for the element volume.
- In case of non-adhesion a sliding contact with friction is assumed between the column wall and the filler, in presence of adhesive bonds a tied-contact between the column wall and the filler is used.
- The folding process is supported by a user-defined self-contact definition to prevent interpenetration of shell elements.
- For thin-walled metal sections, in order to model the experimentally observed deformation modes a mesh coupling technique is chosen (coarse mesh for undeformed zone/fine mesh for deformed zone).
- An adaptive mesh refinement option is chosen for the regions with severe deformation.
- The fracture behaviour (for filler) is modelled by removing the elements on reaching a failure strain threshold.
- In order to speed up a quasi-static process using an explicit numerical code the mass densities are scaled up.

Modelling the Crashworthy of Composite Crash Absorbers

- For the modelling of the thin-walled tubes shell elements which represent the middle surface are used. Some detailed models in which the resin is modelled using solid elements are also presented.
- For the composite laminates multi-layered shell models are used.
- The compression plates for loading tube structures are modelled using solid elements and are assumed to be rigid.
- Since the material responses of the composite materials are anisotropic it is difficult to find a symmetry plane for discretisation.
- In case of foam filling the foam material is modelled with solid elements. For the crushing of the foam core an element removal technique is applied at final fracture.

- A self contact algorithm is defined on the mesh interfaces to prevent interpenetration of the elements and to provide the friction between the parts of the specimen during deformation.
- For composite tubes different failure models used are:

Chang-Chang Failure Criterion, which is a modified version of the Hashin failure criteria in which the tensile fibre failure, compressive fibre failure, tensile matrix failure and compressive matrix failure are separately considered.

Tsai-Wu Criterion, in which element is eliminated if the maximum effective strain is equal to the predefined threshold.

Smooth Failure Surface which is based on an anisotropic continuum damage formulation, which describes a gradual degradation of the elastic material properties.

Composite Bi-phase Model which defines the degradation functions according to strain criteria treating fibre and resin phase separately. An elastic damaging material law allows the modelling of material damage separately in each phase via reduced material stiffness.

- In order to obtain a progressive crushing which is obtained in experiments by triggering, the failure strength of the elements in the crush front is reduced.
- The discretisation of the composite section is changed at the crush front to model the trigger geometry (bevel, tulip and chamfer) for progressive numerical crushing.
- For the modelling of the hybrid tubes, consisting of Al and composite tubes, in case of non-adhesion sliding contact with friction is assumed between the columns walls, in presence of adhesion a tied-contact between the columns walls are used.
- In order to speed up a quasi-static process using an explicit numerical tool the mass densities are scaled up.

Modelling the Impact Mechanism of Sandwich Panels

- Two different approaches are used for the modelling of the honeycomb core sandwich structures. One approach utilises standard solid elements (homogenised model) for the core and shell elements for the facings (Fig. 3.1). The second approach models the honeycomb core using shell elements (unit cell model) (Fig. 3.2).
- Two different approaches are used for the modelling of the interface (bonding) between the facings and the core material. Both approaches use tied-contact. One allows the breakage of the contact depending on the transverse and shear component of the interface stresses. For the case when skin debonding is not significant a tied-contact without failure is used.

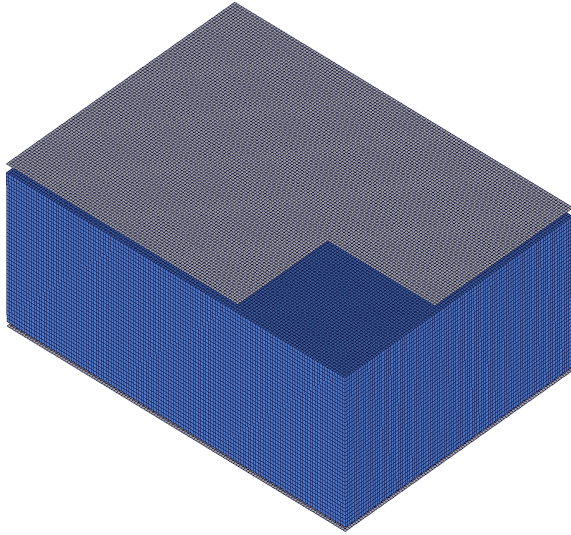


Figure 3.1: Homogenised core modelling

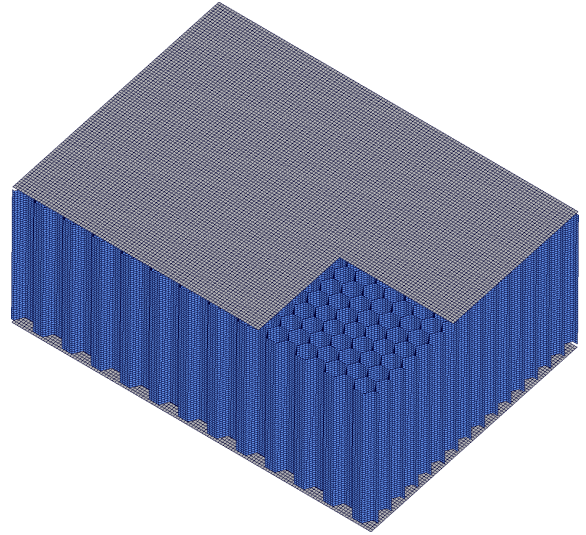


Figure 3.2: Unit cell core modelling

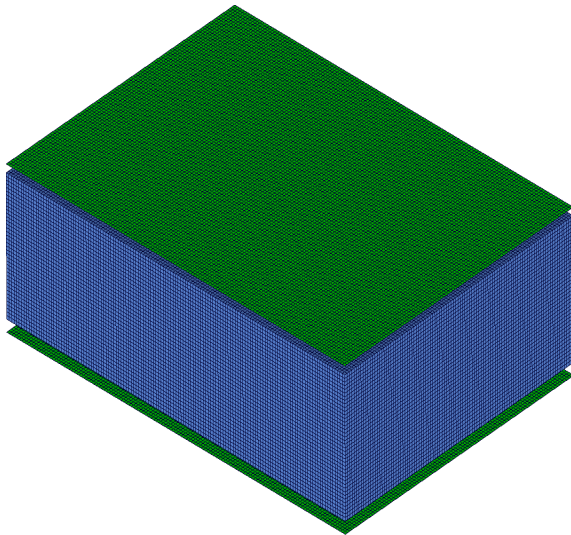


Figure 3.3: Layered shell model for facings

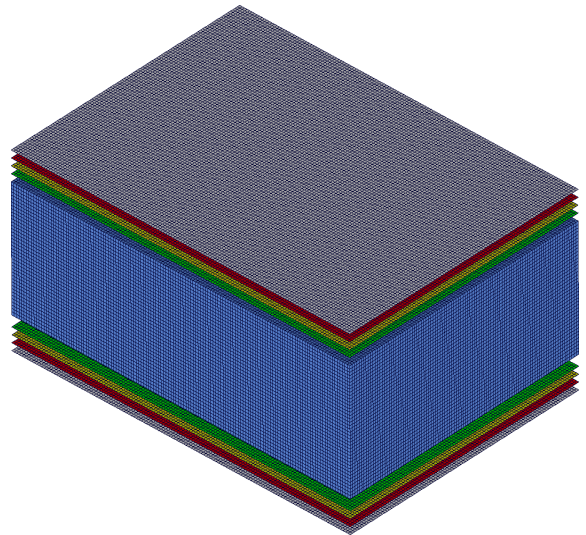


Figure 3.4: Stacked shell model for facings

- For the delamination modelling of the skin laminate there are two approaches. One approach uses a layered shell model without delamination (Fig. 3.3), the second one considers the interaction between adjacent stacked shells and the delamination failure between these layers is included in the model (Fig. 3.4).
- For metallic facings an elastic-plastic material law is assumed.
- For composite facings different failure models are used as discussed above.
- For the impact damage and penetration zone finer discretisation is used.
- The impactor modelling is also an important issue. For hailstone impactor solid elements with rigid material properties are used.
- For tyre burst a detailed fibre-reinforced rubber model with bar (reinforcement) and solid (rubber matrix) are used.
- For bird impact case solid elements were initially used. The most common pure FE-based modelling technique for the bird model is ALE (Arbitrary Lagrangian Eulerian) in which the bird and the surrounding air modelled as fluid using an Eulerian mesh and the bird applies load to the Lagrangian discretised target structure. The coupling realises via an ALE algorithm. The latest trend is the meshless modelling (SPH Method discussed later) of the bird impactor.
- For validation studies the sandwich panels were mounted on a ring force transducer and the interaction force between the load cell and the sandwich panel was measured during impact. For the determination of the resultant force numerically the sandwich panel models are located on a rigid ring, which represents this load cell.

The above listed points are the currently used modelling approaches used in the thesis for the crush and impact simulation using FEM. Another important issue is the correct choice of the numerical time integration algorithm. Implicit algorithms require iterative solutions for each time increment unlike explicit schemes. Using an implicit time scheme to find the displacements at each time step is generally more accurate as compared to the explicit integration method, although it requires more computational time. For the explicit time scheme, the displacements are solved by direct numerical integration of the equations, meaning that prior to numerical integration no transformation of the equations is required. Furthermore, both linear and nonlinear material behaviour can be considered in dynamic analysis. Implicit integration is generally used for the simulations of static responses and moderately nonlinear behaviour whilst the explicit integration is used for the dynamic response, fast dynamic loading, such as crash and impact and highly nonlinear behaviour. Most of the commercial codes available in the market, such as PAM-CRASH, LS-DYNA, ABAQUS, NASTRAN, have

explicit solvers for such problems. Recent work of Noels et al. [81], [82] propose a combined implicit/explicit integration for the dynamic loading cases. The proposed scheme integrates some time intervals with an implicit integration and others with an explicit one. Since it is the out of scope of this thesis the combined implicit/explicit integration approach will not be further discussed here.

Modelling of HVI and crash scenarios involving material failure and large deformation using classical FEM is complex. Although the FEM is established as an effective tool for predicting structural behaviour in different loading conditions, FEM is less reliable for large deformations and structural failure modelling under dynamic loads. Additionally it is difficult to simulate structural failure containing the fracture of material into fragments since FEM is based on a continuum mechanics formulation requiring element connectivity. The elements can either be totally eroded or remain in one piece. This may misrepresent the fracture path, especially for brittle materials. FEM uses Element Elimination Technique (EET) [83] which is based on the quasi-removal of damaged elements which satisfy some imposed failure condition. The FE solver computes local values in the structure in the following succession: first, nodal displacements are calculated, then, element strains, thereafter, element stresses, and finally, nodal forces. As a result of this chain, the reaction forces are calculated for each node of the FE mesh. After applying the external displacements, nonequilibrium state of the structure is established. Since the stiffness matrix depends on the displacements in the nodes, the displacements are corrected in several iterative steps until force equilibrium is established. When the structure is in equilibrium, the code decides for each FE whether it has to be eliminated or not, based on the elimination criteria being applied. To eliminate an element, all components of the stress tensors in this element are set to zero. As a result, all forces in this element become zero as well, and therefore, this element stops to transmit load to neighbouring non-eliminated elements. So, the element elimination does not mean that an eliminated element is really removed from the FE mesh, but stops to interact with neighbouring elements. In solving the problem the tangential stiffness matrix should be corrected after the element elimination. This is done by setting Young's modulus of eliminated elements to be equal to zero [83]. Another drawback of the EET is adjustment of the elimination threshold. Since element elimination limit may be a non-physical parameter it is very difficult to predict and measure.

The enhancement of existing numerical methods based on FEM is a current research theme. Remesh or adaptive remeshing approaches have been proposed for handling these types of problems in FEM. Adaptive remeshing procedures can be summarised in the following four steps: determination of the error estimator or error threshold to define remeshing criteria, remeshing of the deformed body, mapping the state variables and history dependent variables from the deformed state into new one and restart of

the simulation. Although it looks very promising method, it is computationally very expensive since the procedure for determining the error estimation takes time. For this purpose several complex, robust and adaptive mesh generation processors have to be developed. However, these processors are only workable for 2D problems. There are no reliable processors available for creating hexahedral meshes for 3D problems due to the technical difficulty. Adaptive processors require mappings of field variables between meshes in successive stages in solving the problem. This mapping process often leads to additional computation as well as a degradation of accuracy. In addition, for large 3D problems, the computational cost of remeshing at each step becomes very high, even if an adaptive scheme is available.

3.2 Other Alternative Methods

As an alternative to FEM, meshless methods have been developed and applied to numerical simulations involving material failure and damage. Meshless methods replace FEs by a set of nodes or particles within the problem domain and its boundaries. This feature makes meshless methods very effective since mesh connectivity is not as critical as in FEM. There are several meshless methods and new meshless methods are being developed in current research. A class of meshless methods is the particle-based computational methods which are a very general class of Lagrangian computational techniques for simulating the motion of fluids, solids and granular materials. These can be subdivided into meshless continuum methods for solving systems of PDEs (including SPH Method, Particle in Cell, Partition-of-Unity Methods, etc.) and methods for simulating discrete-particle systems (such as DEM and its many variants).

Particle-based methods require a predefinition of particles for material volumes and masses. The algorithm will then carry out the analyses even if the problem domain undergoes extremely large deformation and separation such as fragmentation. SPH Method and DEM belong to this category. Particle-based methods suffer from problems in the imposition of boundary conditions. In addition, predefining the particles still technically requires some kind of initial mesh. Since the thesis focus is particle-based meshless methods, only SPH Method and DEM are discussed in detail here.

3.3 Review of Particle-based Meshless Methods

Discrete Element Method (DEM)

The DEM is an explicit numerical model which approximates the mechanical behaviour of an assembly of arbitrary shaped particles. Having its roots in molecular dynamics, Cundall and Strack [84] used this method to describe the behaviour of particles in granular materials for the first time. These particles displace independently from each

other and interact only at contact points. They are assumed to be rigid bodies therefore their deformation during contact is neglected. Particles are allowed to overlap during contact. This is referred to as soft-contact approach.

The force between particles during contact is calculated with mechanical elements like springs and dashpots. For an oblique contact the contact force is decomposed in normal and tangential direction. For each direction a linear spring and a dashpot are used. Interface friction is realised with a frictional slider. The frictional slider represents a Coulomb-type of friction. The properties of the mechanical elements are referred to as micro parameters. When a virtual material is calibrated the spring stiffness damping and friction coefficient as well as the particle size have to be adjusted. The spring constant is proportional to the Young's modulus and inversely proportional to the particle diameter.

The method is based upon the principles of mechanics for multibody dynamics where each of the bodies under consideration as well as the interbody medium can be modelled using the DE discretisation techniques. The distinct element solution scheme assumes each of its constituents as the separate entity and applies the Newton's second law of motion for translation motion, and force-displacement law at contacts. Newton's law is used to determine the motion of each particle arising from the contact and body forces acting upon it and the force displacement law is used to update the contact forces arising from the relative motion at each contact. For rotational motion it is used to compute the moment effects. These calculations are adopted at each time step, for each particle. This individual particle method allows deletion of the contact with adjacent particles when it experiences the strength equivalent to the bonding strength. This process shows the fragmentation behaviour of the crushing system, as in reality. The DEM works in the principle similar to the time marching scheme of an explicit FE solution. The way of assigning different properties to individual particles (elements) in DEM is much simpler than that of the FEM. Hence, simple laws of contact and laws of motion in the DEM can be considered as an effective method to understand the cracking and fragmentation mechanism of the complex material, such as concrete.

It is particularly suited for studying granular flows, but a couple of drawbacks still exist. At first, the high computational cost has to be mentioned, especially if a realistic number of grains and realistic shapes are used. The force between two particles can be calculated from the strength of the contact between them. The resultant force on a particle is the vector sum of the forces exerted by each of its neighbours. Once the resultant force on each particle has been computed, it is a simple procedure to compute a velocity and position increment for each particle. Finally, the list of which particles are in contact must be re-computed. Every particle's force interaction, acceleration

and movement are calculated individually at each time step. The assumptions underlying the method are only correct and the numerical scheme stable if no disturbance can travel beyond the immediate neighbours of a particle within one time step. This generally means that the time step must be limited to a very small value, thus making the DEM extremely computationally expensive.

DEM has been used in several applications mostly in civil and process engineering and environmental sciences. Among them Kun and Hermann studied the shock fragmentation behaviour of solids [85]- [87]. The concrete cracking was also an interesting application area of DEM. Masuya et al. [88] investigated the structural behaviour of concrete members under impact. The model that they proposed was two dimensional. D'Addetta et al. and Hentz et al. used DEM for the micromechanical modelling of concrete cracking [89]- [90]. Both works aimed at the structural response of the concrete using three dimensional models. Later D'Addetta et al. extended their numerical model for the modelling of the granular assemblies [91]- [92]. Since the nature of DEM is very suitable for the crack problems, Wittel et al. studied the transverse cracking of the cross-ply laminates [93]- [94] and a natural fibre composite soft-wood using DEM [95]. The modelling of bird flow and deformation for a bird strike impact simulation is one of the drawbacks of the FEM. Petrinic and Duffin [96] introduced a DE-based numerical algorithm for the predictive modelling of the bird strike on aircraft structure. For the experimental part of the study gelatine impactors were impacted against a rigid plate. Comparing the gelatine spread over the flat surface of the target and the length of continuously eroding projectile, they obtained satisfactory results with their numerical discrete particle-based tool.

Smooth Particle Hydrodynamics (SPH) Method

SPH Method, also called Free Lagrange Method, is one of the earliest particle methods in computational mechanics. SPH Method was developed and advanced by Lucy [97] and Gingold and Monaghan [98] to solve astrophysical problems in 3D open space. Since its invention, SPH Method has been heavily studied and extended to dynamic response with material strength [99], [100], [101], fracture simulation [102], impact simulation [103], [104], brittle solids [105], and metal forming simulation [106]. Parallel to the introduction of the SPH Method solver in commercial codes and their continuous improvement, SPH Method found several application areas in industry. In the automobile industry the SPH Method is used for the tank sloshing simulations [107]. Anghileri et al. also visited the topic and they simulated the water sloshing in a tank (helicopter) during the impact with ground. Currently SPH Method is becoming a standard simulation tool for bird strike phenomena in aircraft structures [108]- [111].

SPH Method has also been explored for simulating dynamic fluid flows by several researchers. An important application area of SPH Method in aerospace engineering is the ditching simulation and impact on soil ground. SPH Method has been used as an alternative to FEM for soil ground modelling in [112] and for water modelling in [113]- [114]. Pentecôte and Kohlgrüber described in [115] a modelling procedure for simulating the aircraft impact on water. They have also used SPH Method and coupled FEM/SPH Method for the water modelling. Differing from the other studies, they pointed out that the presence of an air layer between the structure and the water surface strongly cushions the forces acting on the structure. Using SPH Method and coupled FEM/SPH Method they obtained promising results and suggested some improvements for better correlations. Naghipour et al. [116] studied the impact response of an energy absorber on coarse soil and rigid ground using both FEM and SPH Method. They pointed out the difficulties of soil ground modelling with FEM and proposed an alternative SPH Method-based model. Comparing the experimental crash response of a metal energy absorber with that of SPH Method-based model satisfactory agreement was obtained.

As a meshless, particle method of pure Lagrangian nature, SPH Method uses smoothed particles as interpolation points to represent materials at discrete locations, so it can easily trace material interfaces, free surfaces, and moving boundaries. The meshless nature of SPH Method overcomes difficulties due to large deformations because SPH Method uses particles or points rather than mesh as a computational frame to interpolate. These features of SPH Method make it attractive, as can be seen from the large literature that has emerged during the last decade.

SPH Method is a Lagrangian technique which allows the numerical grid to be embedded in the material as it deforms which reduces some of the material interface problems associated with Eulerian codes. Furthermore, the ability to handle severe distortions allows the SPH Method to be applied to problems with large deformations or severe element distortions. The SPH Method is generally not as efficient as FEM for structural response applications due to the high computational costs for particle methods. On the other hand the advantage of SPH Method is that it is possible for both severe distortions and normal structural responses to be performed with a single Lagrangian code.

As aforementioned SPH Method is a meshless method which uses a Lagrangian frame. Smooth hydrodynamics variables are computed using a pseudo-particle interpolation method. Although SPH Method uses particle-based representation differing from DEM, each smooth particle has a mass, density, velocity and internal energy which are derived by interpolation or from constitutive relations. It can be used with great advantage to

model bulk materials with no cohesion, such as sand, liquid, gases, or in situations with perforation, as in HVI, or mixing, as in ditching. However it can be computationally much more expensive than classical solid elements in a FE mesh. A smooth particle, similarly to a FE, has its own shape functions, re-constructed at each cycle from its dynamic connectivities. Localisation and information transformation from one particle to another are achieved through the notion of an interpolation distance called the smoothing length. A particle is said to have a contributing neighbour, when another particle lies within the sphere of influence of it. In such case, the particle which lies within the sphere of influence is said to be connected to the central particle. The sphere of influence of a particle is a multiple of its smoothing length. The multiplication factor depends on the type of kernel used to construct the smooth particle shape functions. PAM-CRASH SPH option contains four most frequently used interpolation kernels. These are: W4-Bspline, Q-Gaussian, Quadratic, Quatic. An excellent comparison of these kernel interpolation functions can be found in [117].

First point to be considered is that the foundation of SPH Method is interpolation theory. Second point is that the conservation laws of continuum dynamics, in the form of PDEs, are transformed into integral equations in a weak formulation of the field equations. Computational information is known only at discrete points, so that the integrals are evaluated as sums over neighbouring particles. SPH Method is based on two interpolation approximations: Kernel approximation and particle approximation. Considering the function $f(x)$ in Eq 3.1, value at a point of $f(x)$ over a domain could be extracted from its integral using the delta function (δ) as a filter,

$$f(x) = \int f(x')\delta(x - x')dx'. \quad (3.1)$$

One can define delta function as follows:

$$\int \delta(x - x')dx' = 1. \quad (3.2)$$

As $h \rightarrow 0$, $\delta(x - x')$ can be replaced by with a kernel function $W(x - x', h)$ which has a support domain determined by the parameter h ,

$$\lim_{h \rightarrow 0} W(x - x', h) = \delta(x - x'). \quad (3.3)$$

Therefore Eq 3.3 yields to following:

$$f(x) = \int f(x')W(x - x', h)dx'. \quad (3.4)$$

Since domain is represented by discrete particles, the summation of the contributions of each discrete particle within the kernel approximation range results the smoothed value of $f(x)$ at a point (particle approximation), as

$$f(x) = \sum_{j=1}^N \left(\frac{m_j}{\rho_j} \right) f_j W(x - x', h) \quad (3.5)$$

in which N represents the number of discrete particles, m_j and ρ_j stand for mass and the density of the particle j , respectively.

Approximation of Smoothing Function

Any numerical approximation should represent the physical equations such as differential conservation equations, as the number of particles tends to infinity and as the smoothing length tends to zero. By using Taylor series expansion it can be understood that how accurate is an SPH function and how well it represents the real behaviour of the material.

Suppose that f is a smooth function then applying the Taylor series expansion:

$$f(x') = f(x) + f'(x)(x' - x) + \frac{1}{2}f''(x)(x' - x)^2 + \dots \quad (3.6)$$

$$f(x') = \sum_{k=0}^n \frac{(-1)^k h^k f^{(k)}(x)}{k!} \left(\frac{x - x'}{h} \right)^k + r_n \left(\frac{x - x'}{h} \right), \quad (3.7)$$

where $(r_n(x' - x)/h)$ is the remainder after approximating the derivative to order k . Substituting Eqn 3.7 into Eqn 3.4 leads to;

$$f(x) = \sum_{k=0}^n A_k f^{(k)}(x) + r_n \left(\frac{x - x'}{h} \right) \quad (3.8)$$

where ;

$$A_k = \frac{(-1)^k h^k}{k!} \int \left(\frac{x - x'}{h} \right)^k W(x - x', h) dx' \quad (3.9)$$

At last comparing the left and right hand sides of Eqn 3.8, one can obtain the coefficients A as;

$$\begin{aligned} A_0 &= \int W(x - x', h) dx' = 1 \\ A_1 &= h \int \left(\frac{x - x'}{h} \right) W(x - x', h) dx' = 0 \\ &\cdot \\ &\cdot \\ &\cdot \\ A_n &= \frac{(-1)^n h^n}{n!} \int \left(\frac{x - x'}{h} \right)^n W(x - x', h) dx' = 0 \end{aligned} \quad (3.10)$$

or alternatively the expressions above can be simplified as, in terms of moments, ;

$$\begin{aligned} M_0 &= \int W(x - x', h) dx' = 1 \\ M_1 &= \int (x - x') W(x - x', h) dx' = 0 \\ &\cdot \\ &\cdot \\ &\cdot \\ M_n &= \int (x - x')^n W(x - x', h) dx' = 0. \end{aligned} \quad (3.11)$$

Approximation of Derivatives

The approximation of the first derivative can be obtained by replacing the function f with its derivative;

$$f'(x) = \int f'(x')W(x-x',h)dx'. \quad (3.12)$$

Reformulating Eqn 3.12 using integration by parts one obtains;

$$f'(x) = \int_S f(x')W(x-x',h) \cdot \vec{n} ds - \int f(x')W'(x-x',h)dx', \quad (3.13)$$

\vec{n} is the unit vector of the surface and the first integral is carried on the surface S of the computational domain. Using again the Taylor series expansion yields ;

$$f'(x) = \int_S f(x')W(x-x',h) \cdot \vec{n} ds + \sum_{k=0}^n A'_k f^{(k)}(x) + r_n \left(\frac{x-x'}{h} \right), \quad (3.14)$$

$$A'_k = \frac{(-1)^{k+1}h^k}{k!} \int \left(\frac{x-x'}{h} \right)^k W'(x-x',h)dx'. \quad (3.15)$$

And finally the simplified coefficients can be calculated as ;

$$\begin{aligned} M'_0 &= \int W'(x-x',h)dx' = 0 \\ M'_1 &= \int (x-x')W'(x-x',h)dx' = 1 \\ &\cdot \\ &\cdot \\ M'_n &= \int (x-x')^n W'(x-x',h)dx' = 0 \end{aligned} \quad (3.16)$$

$$W_S(x-x',h) = 0. \quad (3.17)$$

Eqn 3.17 defines the smoothing function value on the surface to be zero, which determines the surface integration $\int_S f(x')W(x-x',h) \cdot \vec{n} ds$ vanish for arbitrarily selected function $f(x)$. The first expression in Eqn 3.16 is actually another representation of Eqn 3.17 as can be observed from the following expression:

$$\begin{aligned} \int W'(x-x',h)dx' &= \int 1.W(x-x',h) \cdot \vec{n} ds - \\ \int (1)'W(x-x',h)dx' &= \int_S W(x-x',h) \cdot \vec{n} ds = 0. \end{aligned} \quad (3.18)$$

The approximation of the second derivative can be obtained similarly to the first derivative and the simplified coefficients can be derived as ;

$$\begin{aligned} M''_0 &= \int W''(x-x',h)dx' = 0 \\ M''_1 &= \int (x-x')W''(x-x',h)dx' = 0 \\ M''_2 &= \int (x-x')^2 W''(x-x',h)dx' = 2 \\ &\cdot \\ &\cdot \\ M''_n &= \int (x-x')^n W''(x-x',h)dx' = 0 \end{aligned} \quad (3.19)$$

$$W_S(x - x', h) = 0 \quad (3.20)$$

$$W'_S(x - x', h) = 0 \quad (3.21)$$

The last two equations determine the surface term to vanish for an arbitrary selected function f and its first derivative. In other words;

$$\begin{aligned} \int W''(x - x', h) dx' &= \int_S 1 \cdot W'(x - x', h) \cdot \vec{n} ds - \\ \int (1)' W'(x - x', h) dx' &= \int_S W'(x - x', h) \cdot \vec{n} ds = 0 \end{aligned} \quad (3.22)$$

So it can be seen the derivatives in SPH Method are computed via analytic differentiation of smoothing function and there is no need for grid generation. It is also clear that the previously discussed requirements on the smoothing function are the representations of SPH approximations for a function and its derivatives. As an illustration the compact supportness property of the smoothing function is also a constituent of the surface Eqns. 3.20- 3.21. Consequently approximating the smoothing function and its derivatives allows estimations of accelerations, strain rates, etc. in continuum equations and plays a very important role in forming the basis of SPH Method.

3.4 Conservation Laws in SPH Method

The second point of consideration is the form of conservation laws in SPH Method. General laws of conservation in continuum mechanics are:

$$\frac{\partial \rho}{\partial t} = \rho \nabla \cdot u \quad (3.23)$$

$$\frac{\partial u}{\partial t} = \frac{1}{\rho} \nabla \cdot \sigma \quad (3.24)$$

$$\frac{\partial E}{\partial t} = \frac{1}{\rho} \sigma : \nabla \otimes u \quad (3.25)$$

In the above equations variables are the scalar density ρ and specific internal energy E , the velocity field u , and the stress tensor, σ . Independent variables are the spatial position x , the time t and the total time derivative $\frac{\partial}{\partial t}$ is taken in the moving Lagrangian frame. Taking into consideration the smoothing function and its derivative, the conservation equations of continuum mechanics after transformation of Equations 3.23- 3.25 into particle formulations yield the following set of SPH equations [118].

The Continuity Equation:

$$\frac{\partial \rho_i}{\partial t} = \rho_i \sum_{j=1} \frac{m_j}{\rho_j} (u_i - u_j) \cdot \nabla W_{ij} \quad (3.26)$$

The Momentum Equation:

$$\frac{\partial u_i}{\partial t} = - \sum_j m_j \left(\frac{\sigma_i}{\rho_i^2} + \frac{\sigma_j}{\rho_j^2} + Q_{ij} \right) \cdot \nabla W_{ij} \quad (3.27)$$

The Energy Equation:

$$\frac{\partial E_i}{\partial t} = - \sum_j m_j (u_j - u_i) \left(\frac{\sigma_i}{\rho_i^2} + \frac{1}{2} Q_{ij} \right) \cdot \nabla W_{ij} \quad (3.28)$$

All the summations above are over neighbouring j particles. A given particle i has a density change determined by Eqn 3.26, an acceleration obtained from Eqn 3.27, and an internal energy change given by Eqn 3.28. The Q term represents the artificial viscous pressure.

SPH Method can be used as an efficient solution technique to overcome the deficiencies of classical FEM. However SPH Method suffers from the following problems:

- **Tensile Instability:** Tensile instability is the situation where particles are under a certain tensile stress state, and the motion of the particles becomes unstable. Since the topological connectivity in SPH Method is not as critical as in FEM, in tensile loading the discrete particles can lose the smoothing interaction and artificial or numerical cracks can be obtained. This issue will be discussed in Chapter 4.
- **Zero Energy Mode:** The zero energy mode has been discovered in both FDM and FEM computations. A comprehensive discussion of the subject can be found in the book by Belytschko et al. [119]. The reason that SPH Method suffers similar zero energy mode deficiency is due to the fact that the derivatives of kinematic variables are evaluated at particle points by analytical differentiation rather than by differentiation of interpolants. In many cases, the kernel function reaches a maximum at its nodal position, and its spatial derivatives become zero.
- **Corrective SPH Method:** As an interpolation among moving particles, SPH Method is not a partition of unity, which means that SPH interpolants cannot represent rigid body motion correctly. This problem was first noticed by Liu et al. [120]- [122].

- **Boundary Conditions:** SPH Method, and in fact particle methods in general, has difficulties in enforcing essential boundary conditions. For SPH Method, some effort has been devoted to address the issue. Takeda's image particle method [123] is designed to satisfy a no-slip boundary condition; it is further generalised by Morris et al. [124] to satisfy boundary conditions along a curved boundary. Based on the same philosophy, Randles and Libersky [118] proposed a so-called ghost particle method in which the problem domain is bounded by artificially generated neighbour boundary particles.

Li and Liu [125] discussed in detail the abovementioned problems and reported on the efforts to overcome these problems.

Chapter 4

Coupling between Finite Element Method and Meshless Methods

4.1 Need for Coupling

The particle-based meshless methods have great potential for the engineering problems involving large deformation and fragmentation; however they use a computationally expensive dynamic neighbouring search algorithm. Consequently coupling methods have been proposed to improve the efficiency of meshless methods. There is a great interest in combining two different numerical methods, because such coupling could exploit the potential of each method while avoiding their deficiencies. Several techniques have been proposed in the literature [126]- [138] to couple different numerical methods, such as combining the FEM with the BEM [126]- [127], the FEM with the Element Free Galerkin (EFG) Method [128]- [131], the EFG with the BEM [132], the FEM with the Meshless Local Petrov-Galerkin (MLPG) Method [133] and the FEM with the DEM [134]- [137]. As Chen and Raju state [138], in coupling methods the analysis domain is divided into two regions and each method is used in a region where it is more efficient. At the interface between the regions, the continuity of the primary variable and the balance of the secondary variables need to be maintained. One technique which is commonly used in the coupling methods [139]- [143] is defining a transition region between the two regions. In the transition region, a ramp transition function is chosen to combine the trial functions (shape functions) of the two numerical methods. This technique is straightforward and widely used in coupling different numerical methods. Using this technique, the continuity condition of the primary variable is satisfied. However, the reciprocity condition of the secondary variables is not guaranteed. Other techniques, such as Lagrange Multipliers Method [144], a Hierarchical Mixed Approximation Method [145], and a method that comprises both FE and EFG Method shape functions in the interface region [146] have also been presented recently.

In this chapter coupling phenomena divided into two groups: Direct coupling (coupling of discrete particles with other elements through force and displacement function)

and adaptive coupling (the progressive replacement of elements with discrete particles during simulation).

4.2 Principles of Direct Coupling

Direct coupling methodology in which FEs and discrete particles are coupled via displacement or force compatibility is used very commonly. In these coupling method, the condition of displacement compatibility must be satisfied. In a coupled method it is ideal to satisfy both the displacement and force equilibrium conditions. The displacement compatibility is the most important in these two requirements and must be satisfied in a coupled method although the force equilibrium condition can not be exactly satisfied in some coupled methods [147].

One of the first coupling procedures for meshless particle methods and FEs was proposed by Attaway et al. [148]. They developed a master-slave coupling for fluid-structure interactions; the fluid was discretised with particles, the structure was modelled with FEs. Their algorithm is based on a common master-slave coupling with penalty forces; in every time step they checked whether particles penetrate element faces. The calculated forces that prevent the interpenetration are always normal to the corresponding element surface. Sliding between particles and elements in tangential direction is allowed. A similar approach was proposed by Johnson [149] and Johnson et al. [150]. In addition, they developed transition elements where particles are fixed to FE nodes. This allows for a rigid coupling in the sense that tensile and shear forces are transferred through the interface. Sauer et al. [151] noted the numerical instabilities in the central processing unit (CPU) intensive SPH Method and applied moving least squares correction methodology to improve the consistency of the meshless SPH approximation. De Vuyst et al. [152] have recently presented a contact based algorithm allowing a frictionless sliding contact between FEs and particles and simulated a projectile impact to an Al target and a ditching problem between a cylinder and water surface. Such coupling methods would exploit the potential of each method while avoiding their deficiencies.

4.3 Principles of Adaptive Coupling

Johnson et al. in [153] established the idea of adaptive coupling with the following sentences: "A long term objective is to allow the user to define almost any impact problem with a standard FE grid, and then to allow the standard elements to be converted to SPH nodes as the standard elements become distorted. Although this approach has been demonstrated, more work is required to increase the accuracy and robustness for a wider range of problems". Later Johnson and Stryk [154] introduced a conversion algorithm which automatically converts the distorted elements into meshless

particles during dynamic deformation. Their method is based on the replacement of distorted FEs which reached the user-defined plastic strain value. After the element was removed from the solution cycle all the element variables such as velocity, stress, strain, internal energy, damage etc. are attached to the replacing particle. They applied the methodology into 3D hypervelocity impact simulations and obtained promising results. Cottrell et al. [155] also studied the same conversion technique. However their conversion technique differs from that of Johnson et al. Additional to the conversion threshold such as plastic strain a critical time step criterion has been chosen as a supplementary control for element conversion. Also the proposed method contains an adaptive remeshing approach. If the deformed element has a critical time step then element conversion can be delayed until an adaptive remeshing takes place and a more geometrically conditioned element can then be put forward as candidate for conversion. Another different point between the works of Cottrell et al. and Johnson et al. is the material parameters of the created meshless particles. In Cottrell et al.'s model the material state variables are not transferred from the removed elements to the created meshless particles. Johnson et al.'s method considers just the particles at the surface; however Cottrell et al.'s model considers the whole model. They concluded that the addition of adaptive remeshing approach provides superior mass conservation than using a purely erosive methodology. Beissel et al. [156] used the methodology that Johnson and Stryk [154] introduced and simulated the characteristics of debris-cloud formation due to hypervelocity impact and obtained satisfactorily results.

4.4 Principles of Semi-Adaptive Coupling

As mentioned in Chapter 3 EET is very common approach to model the material fracture in numerical simulations. The EET is based on the removal of the elements reaching a critical strain threshold. If they are not removed at failure (in case of compression), the element compression strain distorts the element geometry severe that the element length in the load direction becomes very small, which in explicit code simulations significantly reduces the time step and eventually causes error termination. Further, small changes in the strain elimination threshold can change the crushing mechanism drastically and introduce mesh dependency. Therefore it is numerically not effective. In the case of impact the failed material is contained mostly in the impact damage zone and contributed to the damage resistance (friction) after the initial failure. Since FEM is not a suitable tool because of its topological connectivity to model fragmentation behaviour, meshless methods are proposed as an alternative. Especially particle-based meshless methods are very efficient tools since the fragments of the materials can be modelled using discrete particles. The adaptive coupling is a powerful numerical technique however it is not yet possible to use this method with the commercial explicit tools available in the market. Therefore an alternative approach

called Semi-Adaptive Coupling Technique (SAC) is proposed in this thesis to model the fragmentation behaviour more realistically. This technique consists in embedding the discrete smoothed particles based on SPH Method inside the conventional solid elements. On eliminating the solid element at a suitable damage state, the SPH particles remain, thus replacing the FE mesh by a discrete particle formulation in the failure region or damage zone. Here element equivalent shear strain is the elimination criterion used as adaptivity threshold. The FEs are enriched with additional particles. For one-to-one enrichment the DE is situated at the center of each element. However it is also possible to enrich a conventional element with a number n of discrete particles. The discrete particles are connected to FE with tied-contact to ensure the displacement compatibility. One important point is the mass conservation. Since the particle enrichment brings extra mass to the original component modelled with FEs the mass must be re-distributed between the conventional FEs and discrete particles to fulfill the mass conservation issue.

4.5 Benchmark Simulations

This section aims at showing the possible applications of SPH and its coupling with the conventional FEM for the simulation of structural response with some benchmark problems. SPH particles are generated with a simple transformation of FE mesh into mass points. Fig. 4.1 illustrates aforementioned transformation sequentially. Firstly, classical FE mesh is generated. Later the elements which will be transformed into SPH particles are selected and with a SOLID TO SNODE option previously selected elements are transformed into particles (Fig. 4.1). Finally the SPH properties, such as particle smoothing length to radius ratio, minimum and maximum smoothing length, anti-crossing force parameter, of the transformed particles are introduced and through a sliding interface condition, combination or so to say coupling applied. As it is mentioned above, sliding interface achieves combination of different mesh discretisations with a tied kinematic constraint type contact.

Since from-mesh-transformed particles reside in the center of the previously existing mesh, the different mesh pattern case is fulfilled automatically. Smooth particles can be subjected to constraints or loads as if they were nodes. In particular, FEM/SPH coupling is achieved by the use of penalty contacts, where the particles are slave nodes. In particle meshless methods, construction of a neighbouring search algorithm or generally speaking search algorithm is a difficult issue. PAM-CRASH SPH option uses the sorting method to sort the nodes in one direction and to investigate all pairs within a certain distance from this axis. The search distance is automatically determined by the program.

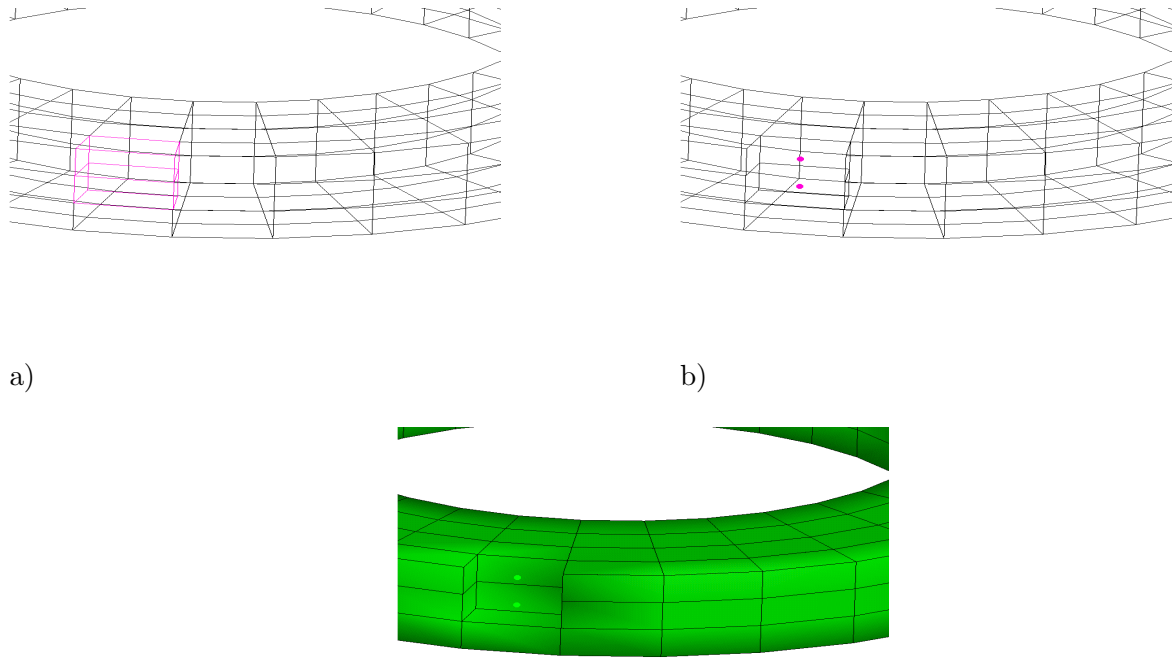


Figure 4.1: a) Selection of the FEs for the conversion into SPH particles, b) conversion of the FEs into SPH particles and c) final discretisation of the FEM/SPH coupling

Since here a commercial code, PAM-CRASH whose source code is not available, was used, coupling was applied through a sliding interface condition. The mesh patterns or both discretisations are combined with a tied kinematic constraint type contact, which connects two contact interfaces defined on two meshed parts of a structure that are close to each other, but whose respective FE grids are not necessarily matching.

Fig. 4.2 shows the compression of an elastic-plastic foam block modelled with discrete SPH particles. In this example discrete particles are compressed between two rigid plates with a constant velocity. Discrete particles enable a stable computation under compression loads up to very high compression strains. Since the compressed specimen undergoes large deformations FEM-based models can suffer from element distortion and/or hourglassing. Therefore the discrete modelling can overcome such problems since the particles are semi-independent the topological connectivity is not as critical as in FEM. The previous example contains only discrete SPH particles and under compression loads give stable computation. The aim of the thesis is the effective application of discrete particles with classical FEs. In Fig. 4.3 a tension specimen modelled using both discrete particles and FEs via coupling. The specimen kept constraint from its lower edge (FE edge) and pulled with a constant velocity from its upper bound (SPH edge). Here the purpose is to see the effectivity of the interaction between the DEs, coupling interface and FEs. Fig. 4.3 shows that the applied tension load creates

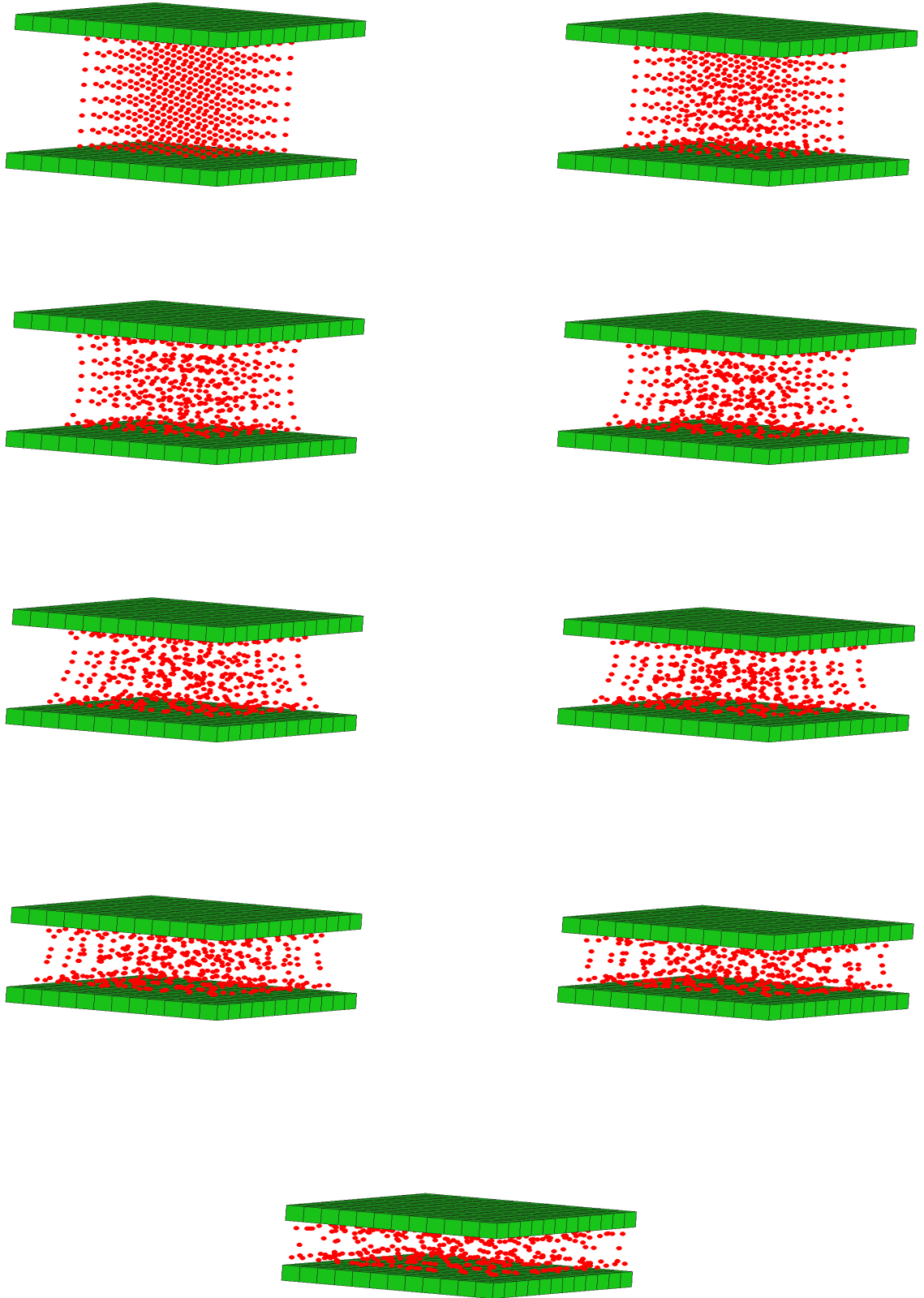


Figure 4.2: Compression of foam block modelled with discrete particles

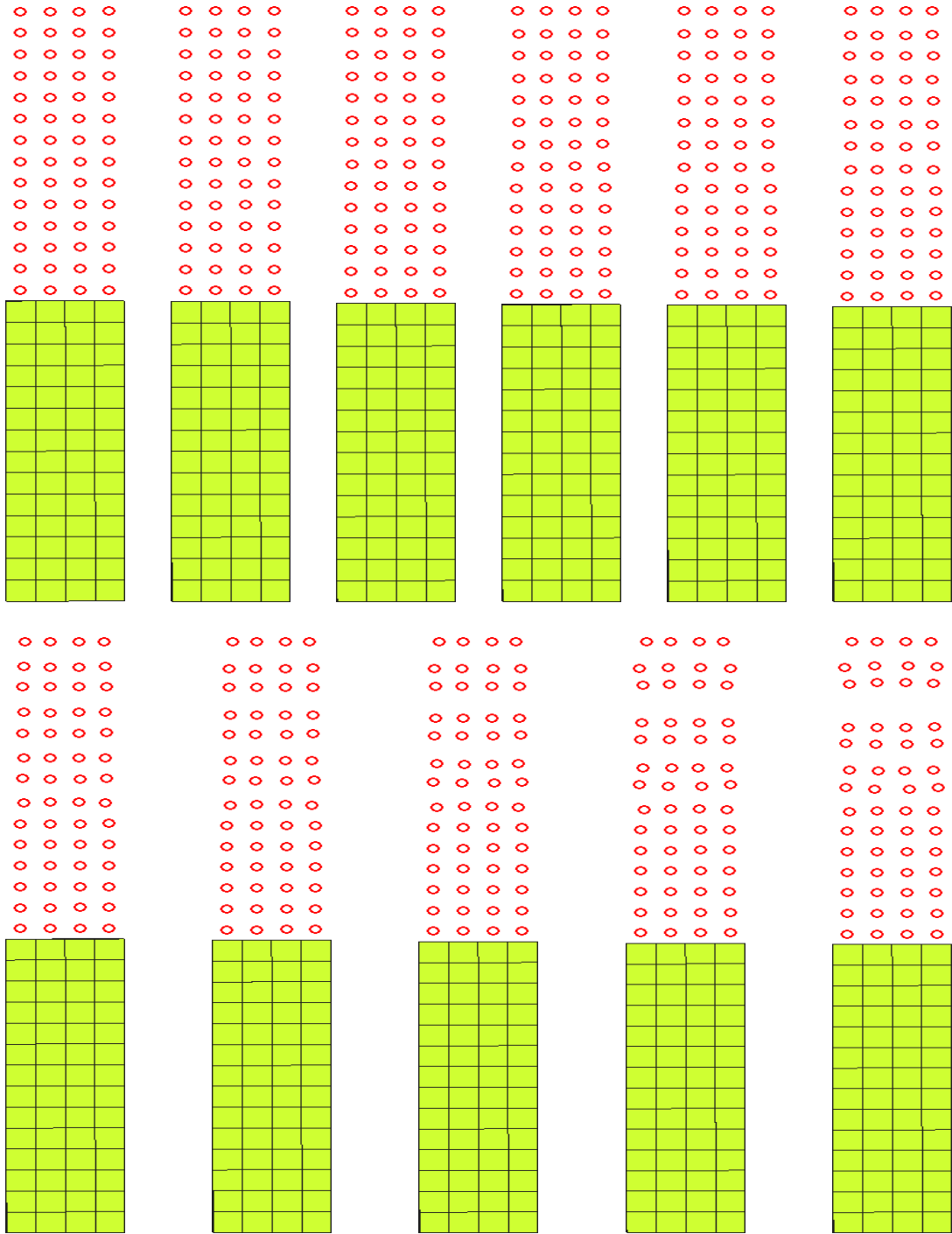


Figure 4.3: Tension test of the flat specimen modelled with FEM/SPH coupling

numerical cracks on the upper bound of the specimen. Although the material model chosen for both discretisations (FEM and SPH) is elastic-plastic without damage, when the distance between two adjacent particles or particle layers exceeds the smoothing length the interaction is lost and particles inside the same domain move independently in contrast to FEM which is based on topological connectivity. As mentioned before the tensile instability results in the depicted numerical cracks. Therefore one can see that DE modelling, pure or its direct coupling with FEM, for tension load case is a problematic issue and it requires specific treatment to overcome the tensile instability.

Fig. 4.4 shows the impact of a rigid impactor onto a composite sandwich plate in which facings are modelled with shell elements whilst the solid elements used for the core. Here the damage for the solid and shell elements of the composite plate are realised by EET. The elements which reach predefined element elimination threshold (here the shear strain) are eliminated from the solution cycle in order to obtain stable computation. However this methodology is not a realistic solution approach as discussed in Chapter 3. Fig. 4.5 shows the discrete-particle-enriched sandwich core. Here solid elements of the composite plate is enriched (entirely) with 1 (Fig. 4.5a) and 4 (locally) (Fig. 4.5b) discrete particles which represent the fragments of its mother element. The coupling between the FE and discrete particle is realised via tied-contact which satisfies the displacement compatibility. Figs. 4.5b-c show the local enriched version of the same impact problem. Here since the damage zone is the region in which the complex damage modes occur just the solid elements in the damage zone are enriched with 4 particles. Again a tied interface between the particles and the FEs has been used.

For the last two examples the switch from FEs to discrete particles is achieved via SAC. One can see the contribution of the discrete particles in the damage zone after EET eliminates the damaged elements from the solution cycle. The elements in the damage zone are eliminated and the DEs replace them therefore they can still carry the impact load (Figs. 4.6 and 4.7).

Although the coupling between SPH and FEM is not preferred for the problems which involve tension Fig. 4.8 shows the robustness of the tied coupling interface between the elements and the discrete particles. As mentioned before particles can be embedded into the classical FEs. In the case of tension as in Fig. 4.8, the particles can carry the tension load, move with the element nodes (displacement compatibility) in the same displacement field. In this example for both particles and FEs elastic-plastic material model without damage has been used. In case of tension this coupling methodology based on SAC can be combined with an EET-based damage. Therefore discrete particles can continue to carry the tension load for some certain additional time.

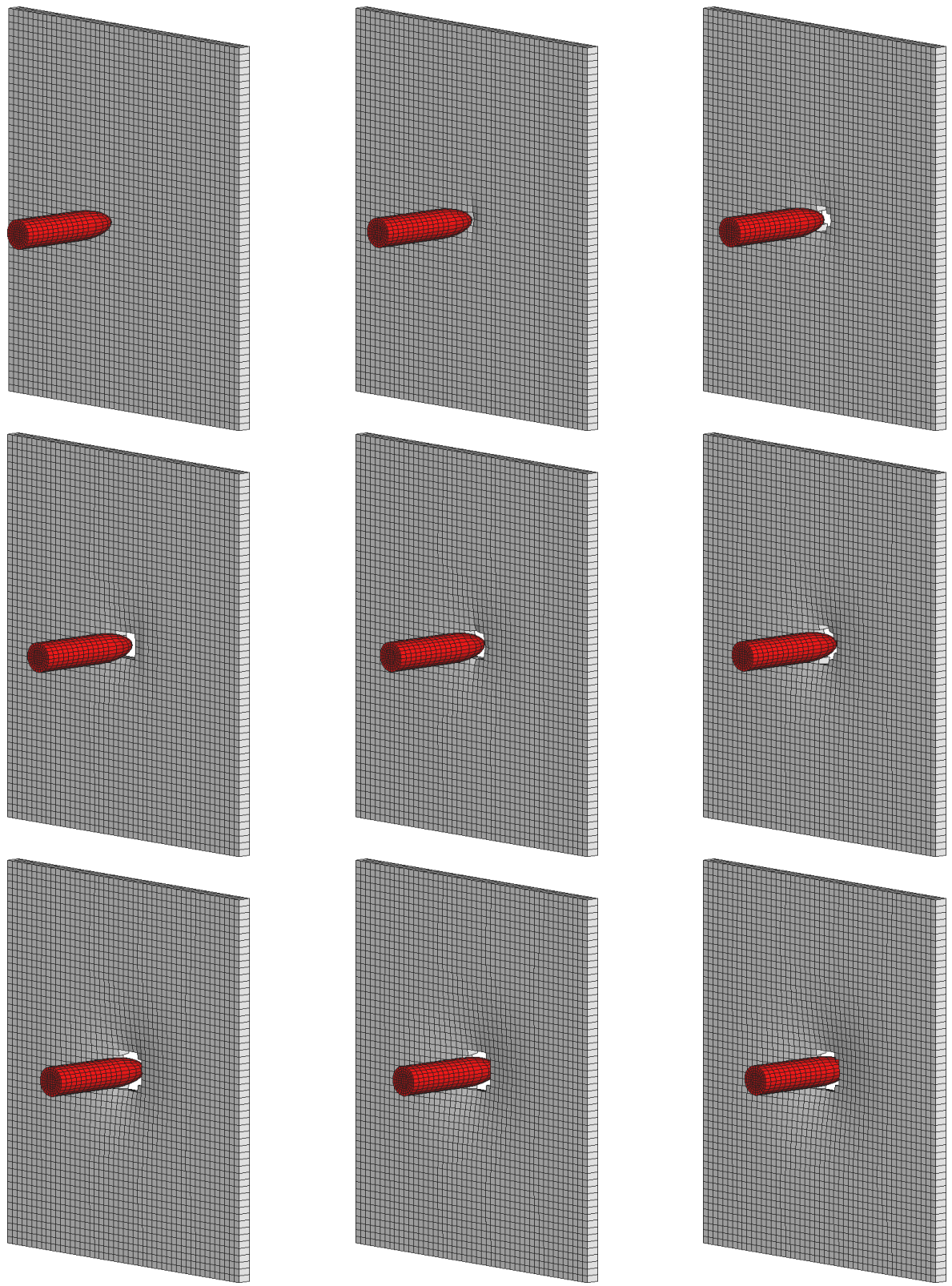


Figure 4.4: Impact of a rigid impactor on a composite sandwich plate using EET-based damage model

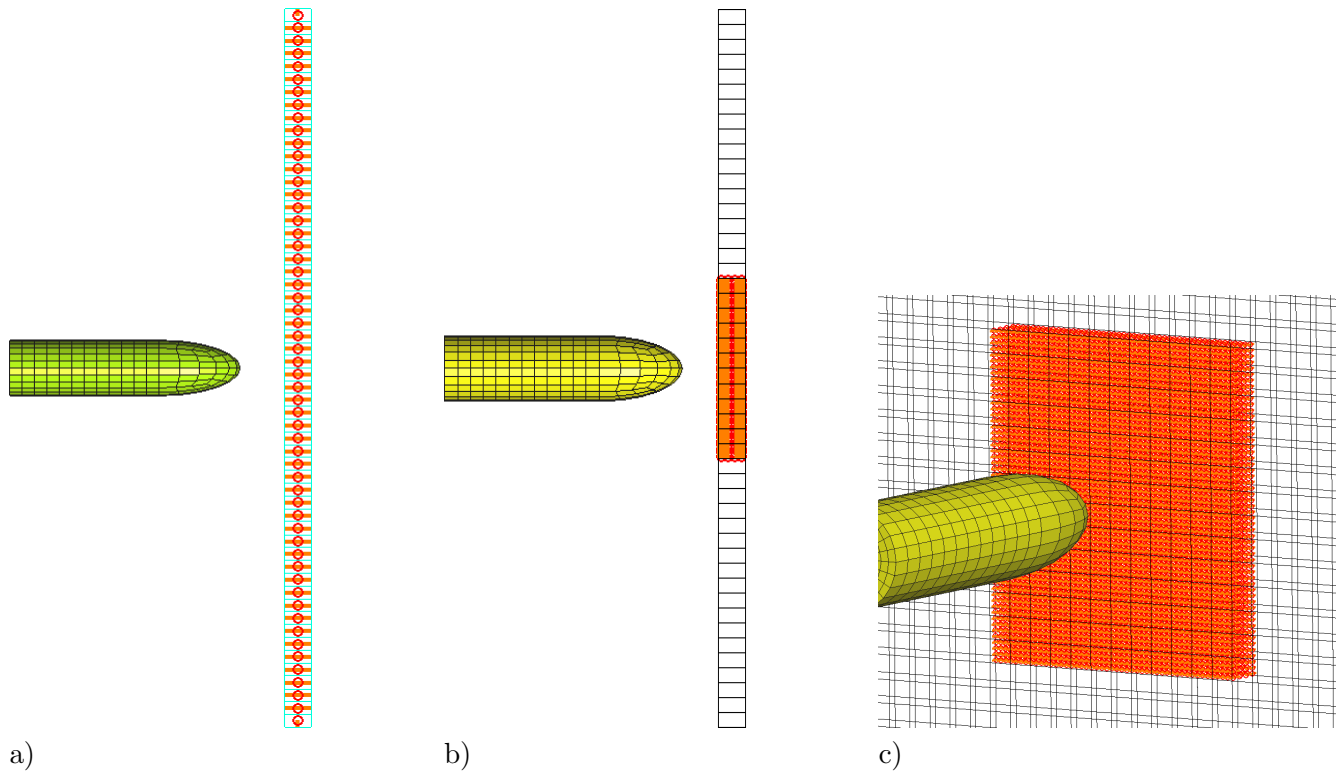


Figure 4.5: Enrichment of composite sandwich core with a) global enrichment with 1 particle , b) local enrichment with 4 particles and c) detailed view of impact damage zone

These benchmark simulations with the SAC of SPH particles and FE meshes have demonstrated the feasibility of this numerical technique. This will now be applied in Chapters 5 and 6 to model failure of metal, hybrid and composite structural elements under crash and impact loads, where conventional FEM techniques alone are unsuitable due to the extensive material fragmentation and failure.

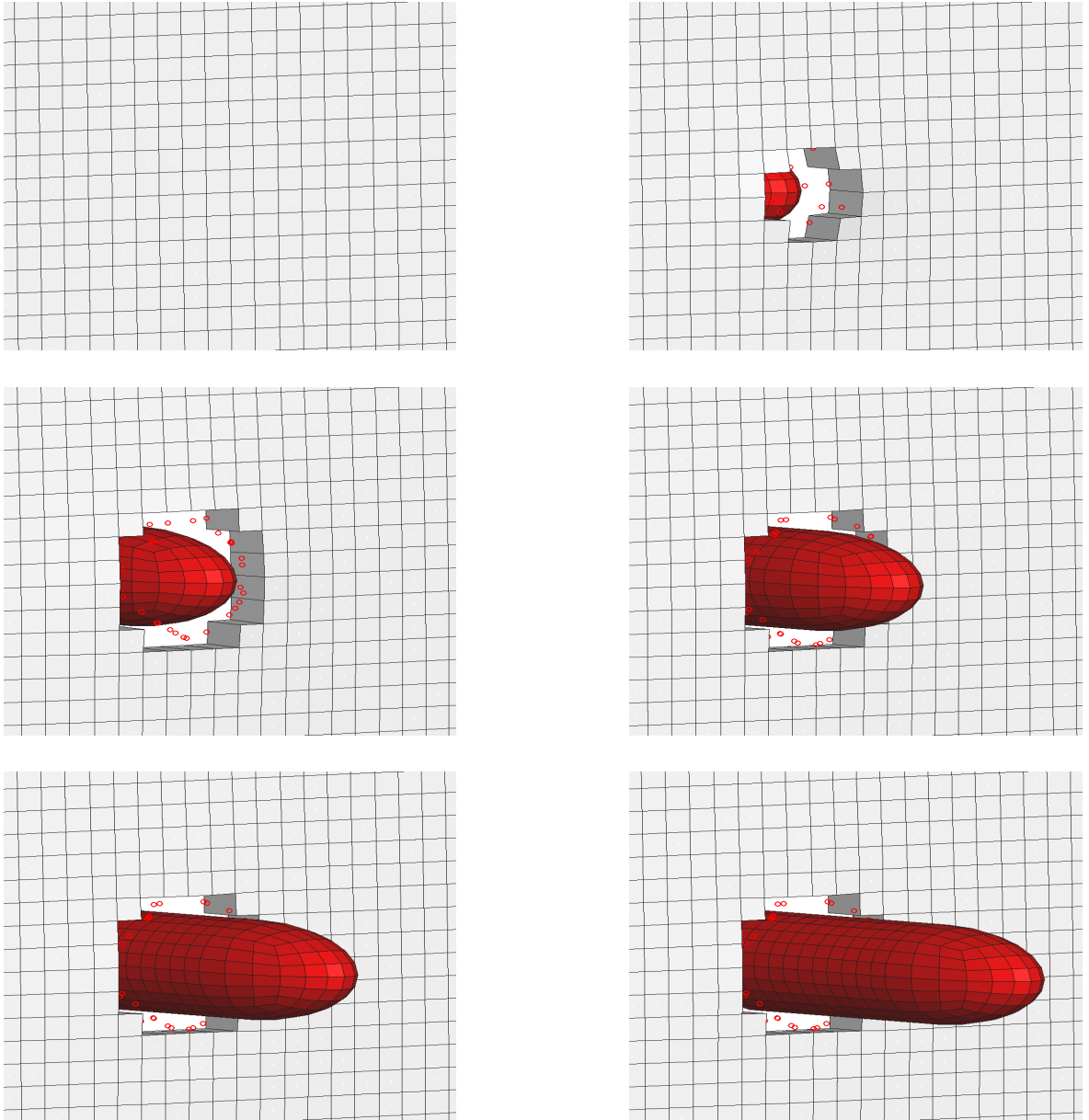


Figure 4.6: Impact of a rigid impactor on a composite sandwich plate using SAC-based damage model (1 discrete particle for 1 FE)

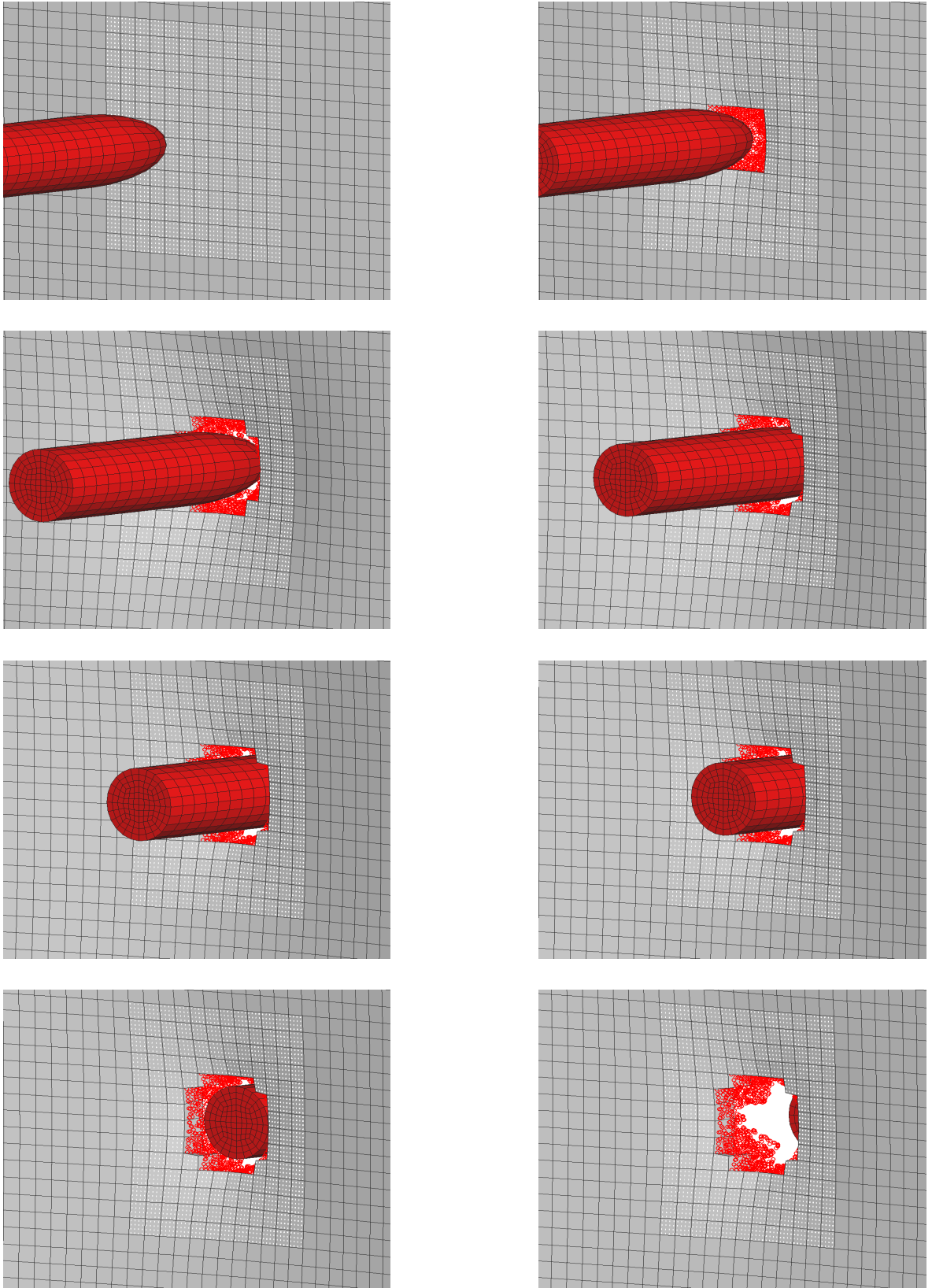


Figure 4.7: Impact of a rigid impactor on a composite sandwich plate using SAC-based damage model (4 discrete particles for 1 FE)

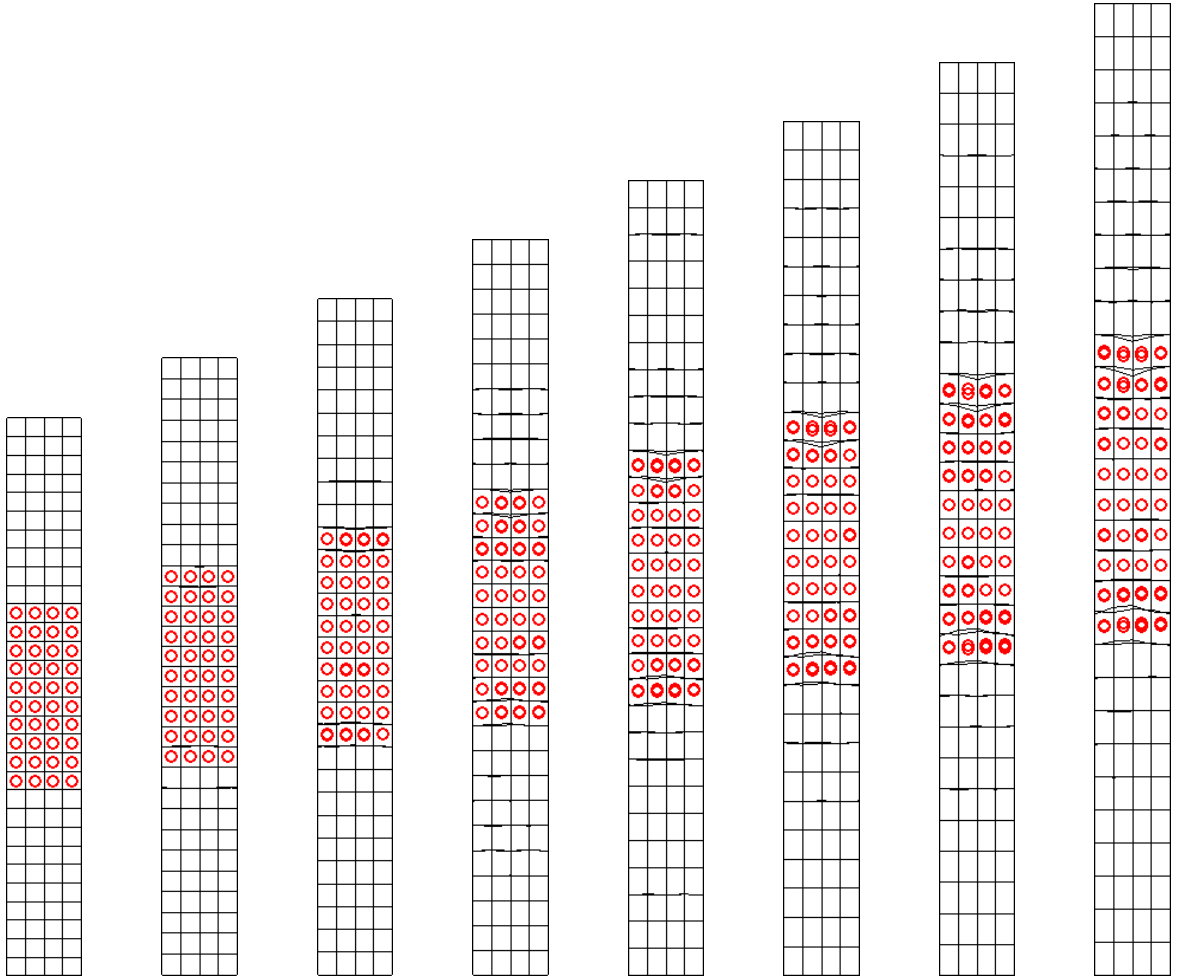


Figure 4.8: Tension test of the flat specimen modelled with FEM/SPH coupling (Discrete particles are embedded in FEs)

Chapter 5

Application of Meshless Methods in Impact Simulations

Chapter 5 aims at showing the efficiency and advantages of meshless SPH Method, direct-coupled FEM/SPH Method and semi-adaptive-coupled FEM/SPH Method for HVI simulations on composite sandwich panels.

First the chapter gives a short overview about the reference model in which FEs were used alone. Later numerical results, such as core deformation mode, penetration depth and impact force pulses of the reference model and those from the proposed alternative methods were compared with experimental investigations.

5.1 Experimental HVI Investigations

Deutsches Zentrum für Luft- und Raumfahrt e.V. (DLR) carries out High Velocity (HV) gas gun impact tests, aiming to determine failure modes, impact resistance, contact force-time curves and total energy dissipation of impact events. In these tests different projectiles, namely hard and soft, are fired against a test structure or against a plate specimen mounted on a load cell. Hard projectiles, representative of runway and engine debris impactors and soft projectiles, representative of bird strike or burst tyre rubber fragments, are possible impact scenarios for an aircraft structure [157]. The test results and observations may be used as experimental outputs for the validation of impact simulations done by FE codes on a range of composite structures. A series of test cases has been developed to investigate the critical parameters associated with the effective modelling of composite and sandwich panels used in aircraft components. Since the impact velocity can be varied, it is possible to simulate in the laboratory actual impacts at high velocities and observe structural failure modes. Impact velocity is varied in gas gun tests by changing the pressure in the pressure vessel and calibration curves for vessel pressure and projectile velocity are used to achieve the required impact velocity. Test data is used to specify appropriate materials for applications involving impact and to design impact resistant structures. An important result of a HVI test is



Figure 5.1: Concrete projectiles (26 ϕ mm x 37mm and 30 ϕ mm x 50mm)



Figure 5.2: Damage to sandwich plate after impact

to define modes of failure and failure thresholds, such as kinetic energy to cause damage to skin and core. Impact loads as functions of time may be recorded in an impact test, if the impacted structure is mounted on a load cell. A HV impact test program was carried out at the DLR in which several sandwich plates were tested with different projectiles, representative of stones and runway debris.

Two typical concrete projectiles manufactured as cylinders with a spherical end from B25 concrete are shown in Fig. 5.1. In this chapter the impact test results are based on a projectile with 26mm in diameter, 37mm in length and mass of 36.4g. Sandwich plates were manufactured with PEI foam or Nomex honeycomb core, 33mm thick, with [0/45/0/45]₂ carbon fibre fabric/epoxy facings with a nominal thickness of 1.6mm. The projectiles are placed in 50mm diameter PU sabots which are the exact diameter of the gas gun barrel and fired at the panels so that the rounded end impacts the panel surface.

A nominal impact velocity of 60m/s was chosen, which corresponds to the maximum expected impact velocity of runway debris on an aircraft structure during start and landing. The actual impact velocity is measured optically using two light beams set 100mm apart, which are broken by the passage of the projectile. The first light beam triggers the transient recorder to start and the time taken for the projectile to reach the second light beam is measured.

Under these impact conditions the concrete projectiles will usually damage the skin laminate and penetrate into the PEI or Nomex core before being stopped by the sandwich panel as is seen in Fig. 5.2. Quantitative test data are difficult to obtain in HV gas gun tests, since it is not possible to instrument the projectile which is the procedure adopted in low velocity drop tower tests. The DLR has developed a procedure which

measures the resultant force pulse on the panel specimen by mounting it on a ring load cell, with the impact position on the panel aligned with the centre point of the load cell ring.

Modelling Composites Properties

For metals there is extensive information in the literature on dynamic materials properties at large strains and high strain rates, and appropriate constitutive equations have been implemented into FE codes for structural impact simulations. For composite materials dynamic failure behaviour is very complex due to the different fibres and matrices available, the different fibre reinforcement types such as unidirectional (UD) fibres and fabrics, the possibility of both fibre- or matrix-dominated failure modes, and the rate dependence of the polymer resin properties. Thus at present there are no universally accepted materials laws modelling damage arising in crash and impact of composites. It was considered that a homogeneous orthotropic elastic damaging material was an appropriate model for UD and fabric laminates, as this is applicable to brittle materials whose properties are degraded by micro cracking. Constitutive laws for orthotropic elastic materials with internal damage parameters are described here, and take the general form

$$\epsilon = S\sigma \quad (5.1)$$

where σ and ϵ are vectors of stress and strain and S is the elastic compliance matrix. In the plane stress case required here to characterise the properties of composite plies or shell elements with orthotropic symmetry axes (x_1, x_2) , the in-plane stress and strain components are

$$\sigma = \begin{pmatrix} \sigma_{11} \\ \sigma_{22} \\ \sigma_{12} \end{pmatrix} \quad \epsilon = \begin{pmatrix} \epsilon_{11} \\ \epsilon_{22} \\ 2\epsilon_{12} \end{pmatrix} \quad (5.2)$$

Using a strain equivalent damage mechanics formulation, the elastic compliance matrix S may then be written :

$$\mathbf{S} = \begin{pmatrix} \frac{1}{E_1(1-d_1)} & \frac{-\nu_{12}}{E_1} & 0 \\ \frac{-\nu_{12}}{E_1} & \frac{1}{E_2(1-d_2)} & 0 \\ 0 & 0 & \frac{1}{G_{12}(1-d_{12})} \end{pmatrix} \quad (5.3)$$

where ν_{12} is the principal Poisson's ratio, which for simplicity is assumed not to be degraded. This general plane stress form for an orthotropic elastic material with damage has 3 scalar damage parameters d_1, d_2, d_{12} and 4 "undamaged" elastic constants: the Young's moduli in the principal orthotropy directions E_1, E_2 , the in-plane shear modulus G_{12} , and the principal Poisson's ratio ν_{12} . The damage parameters have values $0 \leq d_i \leq 1$ and represent modulus reductions under different loading conditions due to progressive damage in the material. Thus for UD plies with fibres in the x_1 direction, d_1 is associated with damage or failure in the fibres, d_2 transverse to the fibres, and

d_{12} with in-plane shear failure. For fabric reinforcements then d_2 is associated with the second fibre direction. In order to proceed further evolution equations are required which relate the damage parameters to other state variables. Several different models have been proposed in the literature. In [158] and [159] it is postulated that the damage parameters are functions of strain energy release rates in the material, and this method has been developed further in the [160], to include plasticity and rate effects in damage evolution.

This chapter is concerned with the application of PAM-CRASH, a commercial explicit FE crash code [161], to analyse the crash response of composite structures. The code contains several materials models and special elements for laminated composite materials. The damage mechanics formulation outlined above is currently being implemented and tested in the code along with a new approach to delamination modelling in stacked shell elements described in [159]. The crash simulations of composite aircraft components reported in [158] and [162] are based on alternative models in which it is supposed that damage evolution is dependent on the strain invariants, which can be determined from measured stress-strain curves. The elastic damaging materials law for fabric reinforcements may be modelled in PAM-CRASH as a "degenerate bi-phase" model in which the UD fibre phase is omitted, and the matrix phase is assumed to be orthotropic. If the simplifying assumption is made that $d_1 = d_2 = d_{12} = d$, the composite fabric ply has orthotropic stiffness properties, but a single "isotropic" damage function d which degrades all the stiffness constants equally. The code does however allow different damage functions in tension and compression. This model has been found to be easy to apply and appropriate for quasi-isotropic laminates, which are commonly used in aircraft structures. An improved bi-phase model in [162] has been developed and implemented, which allows two independent fibre directions in plies and may be used when orthotropic damage effects are more significant.

It is necessary to determine parameters for the chosen composites model from measured stress-strain curves. Uniaxial stress-strain curves are assumed to have a damage evolution equation which is a bilinear function of strain, in which there are two damage constants d_1 and d_u to be determined, (note d_1 here should not be confused with the damage parameter d_1). Typical uniaxial stress-strain curves have the general form shown Fig. 5.3, where ϵ_i is strain at the onset of initial damage, ϵ_1 is the strain at the peak failure stress, and ϵ_u is a limiting strain above which the stress is assumed to take a constant value σ_u .

Measured test data for fabric composites are used to calibrate the materials model and to determine the damage parameters d_1 and d_u for the analysis. The parameter d_1 is related to the departure from linearity at the first "knee" in the stress-strain curves,

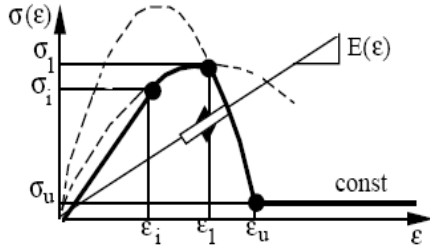


Figure 5.3: Stress-strain diagram

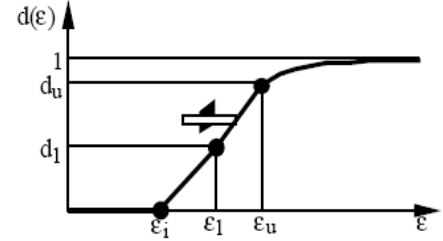


Figure 5.4: Corresponding fracturing damage function

and is thus small in tension, whilst the parameter d_u determines the residual stress value σ_u shown in Fig. 5.4. For the FE analysis it is not good practice to reduce the material stresses directly to zero at material fracture, as this may lead to numerical instabilities. Thus under tensile stresses typically $d_u \approx 0.95$, indicating that the element is nearly fully damaged, whilst in compression $d_u \approx 0.5$ to model the residual compression crushing stresses. In this way it is possible to attribute measured crush stresses to shell elements under axial compression load so that EA in composite structures may be simulated with shells. Materials rate dependence is not included in the modelling presented here.

Modelling of Sandwich Core Materials

Modelling of PEI Foam Core

Foams are one of the most common forms of core materials in composite sandwich structures. They can be manufactured from a variety of synthetic polymers including polyvinyl chloride (PVC), polystyrene (PS), polyurethane (PU), polymethyl methacrylamide (acrylic), polyetherimide (PEI) and styreneacrylonitrile (SAN). Foam core materials are widely used in automotive and aerospace applications for energy absorbers, sound dampers and for cushioning. Because of their high energy absorbing capability structural foams are very important in vehicle crashworthiness. However foam-cored sandwich structures are susceptible to in-plane shear and core compression failure, buckling instability and face sheet-to-core debonding. The core must be capable of taking a compressive loading without premature failure. This helps to prevent the thin skins from wrinkling and failing in a buckling mode.

FE modelling of foam materials becomes important in the prediction of sandwich behaviour. Although foams are promising materials, their mechanical properties have not been studied as extensively as other commonly used engineering materials. Thus different approaches are available to define the behaviour of foam materials [163]- [164].

The DLR carried out compression tests on PEI foam core and a typical stress-strain

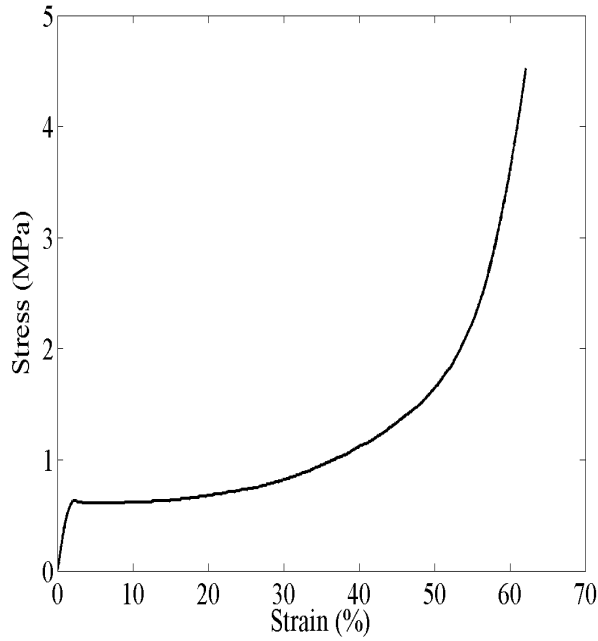


Figure 5.5: Stress-strain plot of PEI foam core

curve is shown in Fig. 5.5. To model this behaviour in PAM-CRASH a crushable foam solid, namely PAM-CRASH Material Model 2 [161], was used. The elastic behaviour of this material is described by the shear modulus and the initial tangent modulus. The inelastic behaviour exhibits both, volumetric (bulk) plasticity and deviatoric (shear) plasticity. The coupling between both parts of the material response is established via a pressure (p) dependent von Mises (J_2 plasticity) yield surface.

$$\phi_s = J_2 - (a_0 + a_1 p + a_2 p^2) = 0 \quad (5.4)$$

where

$$J_2 = \frac{1}{2} S_{ij} S_{ij} = \frac{1}{3} \sigma_Y^2 \quad (5.5)$$

is the second invariant of the deviatoric stress tensor on the yield surface. a_0 , a_1 and a_2 are user-specified material parameters, which are linked to the user-specified pressure cutoff for tensile fracture.

Volumetric Plasticity

The volumetric plasticity is computed first. It is governed by the volumetric yield function

$$\phi_v(p) = p - f_p(\epsilon_v) \quad (5.6)$$

where the $f_p(\epsilon_v)$ is a user-specified volumetric strain-stress curve. The curve must be specified such that its slope is nowhere greater than the unloading bulk modulus, K_o .

Deviatoric Plasticity

The deviatoric plasticity part of the response is calculated next, using a conventional plasticity theory with radial return. The program evaluates trial deviatoric stresses as

$$S_{trial} = S_n + 2G\Delta e_n. \quad (5.7)$$

where $\Delta[e_{ij}]_n = [e_{ij}]_n\Delta t_n$ is the increment of the deviatoric strain tensor. Using the trial stress, the program calculates $J_{2,trial}$ and compares it with the present yield level of $J_2 = a_0 + a_1p + a_2p^2$. If the trial value exceeds the yield value of J_2 , a simple radial return is performed to obtain the stresses

$$S_{n+1} = (J_2/J_{2,trial})^{\frac{1}{2}}S_{trial} \quad (5.8)$$

at the end of this time step. The total stress is calculated from

$$\sigma_{n+1} = S_{n+1} - p_{n+1}\delta. \quad (5.9)$$

Modelling of Aramid Paper Honeycomb (Nomex) Core

Nomex honeycomb is made from Nomex paper, a form of paper-based on aramid fibres rather than cellulose fibres. The initial paper honeycomb is usually dipped in a phenolic resin to produce a honeycomb core with high compression strength and good fire resistance.

The honeycomb core properties depend on the size of the cells and the thickness and strength of the web material. They can give stiff and very light sandwich laminates with composite skins and high-performance resin systems such as epoxy provided that the necessary adhesion to the laminate skins can be achieved.

For the material modelling of Nomex a homogenised model for solid elements has been adopted. Fig. 5.6 shows the compression behaviour of the Nomex honeycomb as measured in tests at the DLR. In PAM-CRASH a nonlinear fibre bi-phase solid, namely PAM-CRASH Material Model 31 [161], was chosen to simulate the material response. PAM-CRASH Material Model 31 corresponds to highly anisotropic and nonlinear honeycomb cores which the through thickness compression properties are modelled as elastic-plastic.

5.2 Numerical Modelling of HVI Simulations - FEM

The FE simulations were carried out for two kinds of sandwich plate mounted on a ring load cell and impacted at the centre by a cylinder projectile. Fig. 5.7a illustrates the

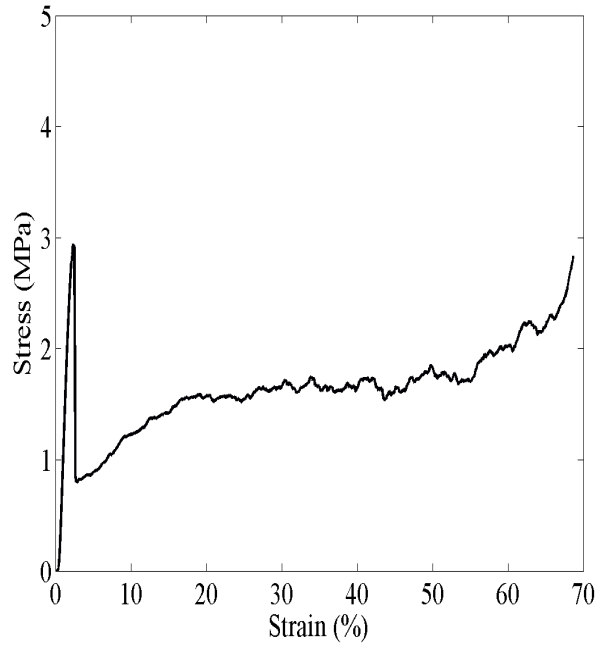
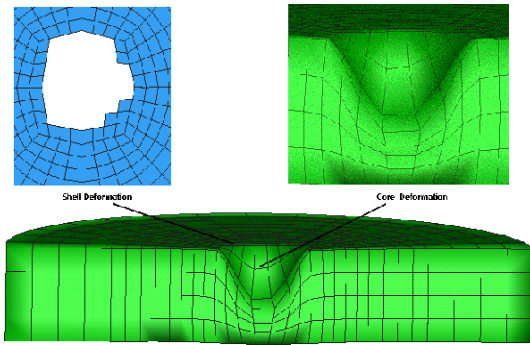


Figure 5.6: Stress-strain plot of Nomex core

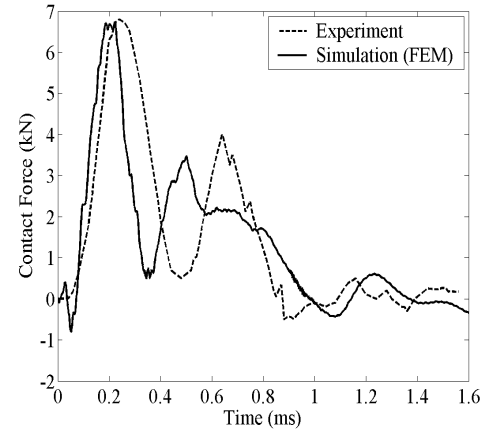
final state of the impact simulation in which the projectile is modelled as rigid. One can see the large deformation on the PEI core. The core material under impact load shows a classical elastic-plastic response. Contact force history in Fig. 5.7b shows that the impact model proposed in this work provides reasonable accurate contact force history of HVI on sandwich structures.

As one can observe, the first peak load is about 7kN and the second peak load is about 4kN. When the projectile impacts the upper skin of sandwich plate the first peak load is obtained. Depending the EA mechanism of the sandwich plate and the system dynamics, the projectile loses some kinetic energy and this results in a lower second peak. The same procedure was followed for the simulation of impact on Nomex core sandwich plate as shown in Fig. 5.8a. Fig. 5.8b shows the same double peak characteristic however with different peak values which are a little lower than those from the impact on PEI core sandwich plate.

The contact force history plot can give us information about the EA capability of sandwich plates. However kinetic and internal energy history plots illustrate this phenomena more clearly. Figs. 5.9a-b show the kinetic/internal energy history of the PEI and Nomex core sandwich plates, respectively. For both cases, which have the same initial velocity, projectile kinetic energy after impact is absorbed as internal energy in the skins and core. In the two plots, the internal energy levels that the upper and lower skins absorb after impact are almost the same. However, the level of internal energy

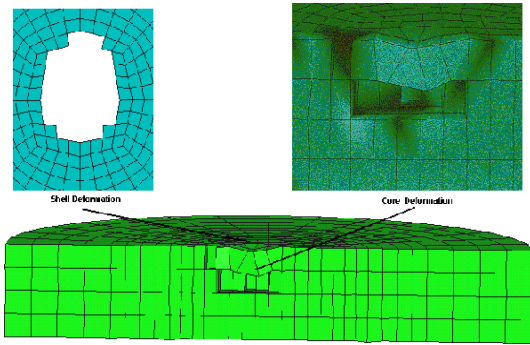


a)

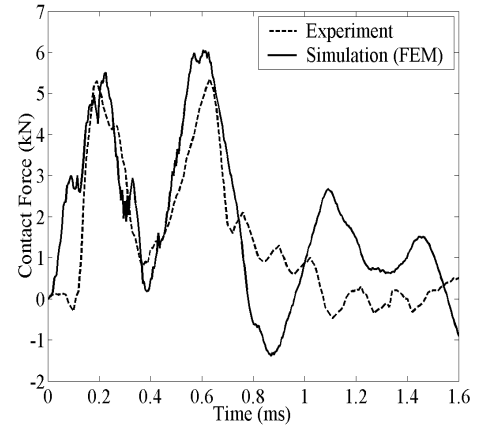


b)

Figure 5.7: a) Final state of PEI core sandwich plate, b) comparison of the contact force history plots

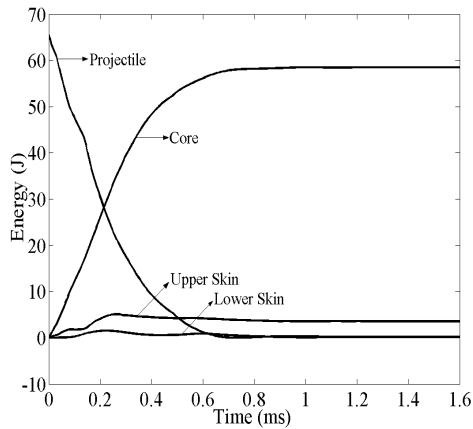


a)

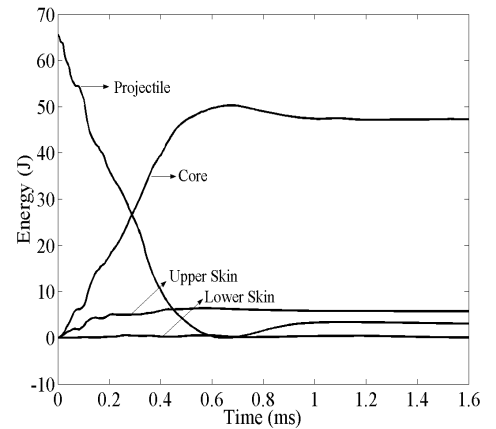


b)

Figure 5.8: a) Final state of Nomex core sandwich plate, b) comparison of the contact force history plots



a)



b)

Figure 5.9: Kinetic and internal energy history plot for a) PEI core sandwich plate, b) Nomex core sandwich plate

that PEI core dissipates is higher than that of Nomex core.

5.3 Discussion - FEM

The numerical impact models based on FEs provide reasonable accurate details of HVI on sandwich structures including impact force, displacement, velocity and energy response and damage development during impact. Good agreement was obtained with impact loads for PEI and Nomex core sandwich panels. Although the existing numerical model is generally good at predicting failure modes in composite structures, further refinement is needed for better quantitative correlations.

5.4 Numerical Modelling of HVI Simulations - SPH and Direct-Coupled FEM/SPH Method

The proposed FE mesh-based model can be used for accurate prediction of failure modes in sandwich panels. However topological element connectivity in FEM can lead to numerical instabilities (for higher velocities) and further enhancement is needed for better quantitative correlations. Following this idea, carbon fibre/epoxy facings were modelled with standard layered shell elements, whilst SPH particles are used for the PEI core where extensive crushing and fracture by the rigid impactor occur. Use of solid elements here leads to aforementioned difficulties with excessive distortion. Beside the advantages of its meshless nature, as a result of the dynamic neighbouring search algorithm, the SPH Method is computationally expensive. One alternative numerical solution technique that is commonly used is coupling. Since SPH Method uses Lagrangian framework, a possible coupling between SPH Method and standard Lagrangian FEM is straightforward. This means (for impact problems) a coupling between discrete smoothed particles for the parts where large deformation occurs and FEs for the parts where small deformation takes place is possible. Such coupling would exploit the potential of each method while avoiding their deficiencies. In this approach, coupling was applied through a sliding interface condition. The mesh patterns or both discretisations can be combined with a tied kinematic constraint contact that connects two contact interfaces defined on two meshed parts of a structure that are close to each other but whose respective discretisation grids are not necessarily matching. Discrete SPH particles are generated with a simple transformation of FE mesh into mass points.

Meshless Modelling of PEI Foam Core

In order to overcome the high mesh distortion which causes numerical problems with the time step assignment in explicit codes, the elements are replaced by interacting particles. In the pure SPH approach all FE meshes of the PEI core are replaced by SPH particles, and in the direct-coupled FEM/SPH approach the highly distorted local

damage zone is replaced by particles. The material response assigned for discrete SPH particles is an isotropic elastic-plastic-hydrodynamics solid material model in which the pressure-volume relation is modelled by an equation of state (EOS). This material model was originally developed for ballistic impact in metals and describes an isotropic elastic-plastic material at low pressure, whose properties are defined by the shear modulus and tangent modulus or effective plastic stresses and effective plastic strains. Additionally with EOS describes the “hydrodynamic” pressure-volume behaviour at high pressures. In this case it is given as following:

$$p = C_0 + C_1\nu + C_2\nu^2 + C_3\nu^3 \quad \nu = \frac{\rho}{\rho_0} - 1 \quad (5.10)$$

C_0, C_1, C_2, C_3 are material constants, ν is a dimensionless compressibility parameter defined in terms of the ratio current density, ρ , to initial density, ρ_0 . The polynomial form is an established approximation of the observed EOS for many materials, see for examples [165], with the feature that it reduces to a dilatational elastic materials law with bulk modulus C_1 when $C_0=C_2=C_3=0$.

To make a qualitative comparison between FEM, SPH Method and direct-coupled FEM/SPH Method, impact simulations were carried out for a sandwich composite panel mounted on a ring load cell and impact at the centre. Normal impact from a rigid impactor was considered at nominal impact velocity of 60m/s, which corresponds to the typical impact speed of runway debris on an aircraft structure during start and landing.

Here three different approaches have been used to model the impact damage on PEI core sandwich panels, as analysed previously by the FEM. In all three cases impactors first damage the upper skin and penetrate into the sandwich core. Figs. 5.10a and 5.11a show the maximum penetration and post-impact core deformation with pure FEM. One can observe the large deformation on the PEI core. The core material under impact load shows classical elastic-plastic response. FEM approximations are continuum-based approximations and the topological connectivity in FEM is very critical. The modelling of core deformation with higher impact velocities can cause element distortion problems resulting in error termination. Therefore the core has been modelled using discrete SPH particles. Figs. 5.10b and 5.11b show the maximum penetration and core deformation for the numerical impact simulation with SPH Method. In SPH Method the topological connectivity is not as critical as in FEM and the core deformation can be modelled without having element distortion problem. Since in SPH Method the number of discrete particles and the domain of influence of each particle are decisive for the CPU times, direct-coupled FEM/SPH Method, which combines the faster computation nature of FEM and accuracy of SPH Method, is proposed. Figs. 5.10c and 5.11c show the maximum penetration and post-impact core deformation with proposed

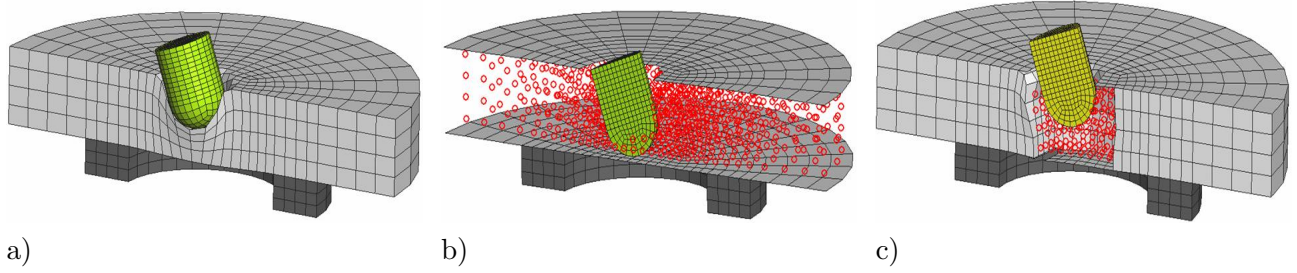


Figure 5.10: Numerical HVI model: a) FEM, b) SPH and c) direct-coupled FEM/SPH model

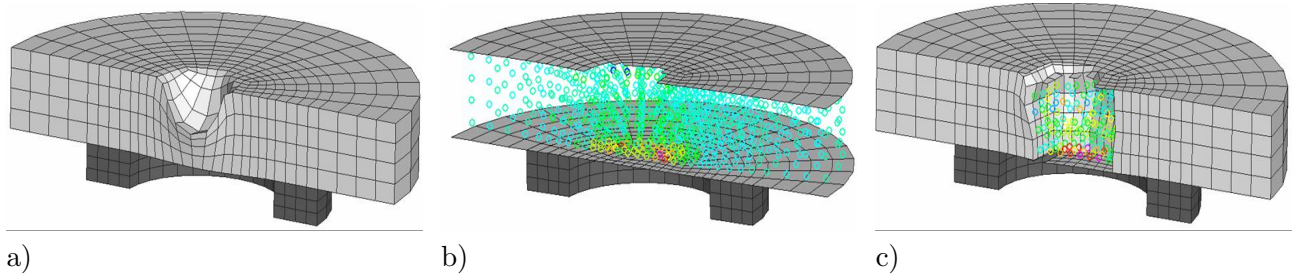


Figure 5.11: Maximum core penetration for a) FEM, b) SPH and c) direct-coupled FEM/SPH model

direct-coupled approach. Here one can observe the interaction between the FEM-based and SPH Method-based modelled impact damage zone. After damaging the upper skin the impactor penetrates into the sandwich core. In both SPH Method and direct-coupled FEM/SPH Method the impactor compresses the particles in the damage zone and its kinetic energy is absorbed by the particles in the damage zone. However one can observe that the penetration of the impactor in the pure SPH Method is larger than the pure FEM and direct-coupled FEM/SPH Method. In experimental investigation the maximum penetration value has been measured as 25mm. The maximum penetration values are 20, 32 and 19.5mm, respectively, in the example computed here.

Contact force history comparison between experimental analysis and FEM simulation in Fig. 5.12a shows that the proposed FEM model provides reasonable accurate contact force history of HVI on sandwich panel. As one can observe from the experimental curve, the first peak load is about 7kN and the second peak is about 4kN. Depending on the EA mechanism of the sandwich plate, the projectile loses its kinetic energy and resulting in a lower second peak. Proposed FEM model estimates especially the first peak value accurately, which is very critical value for impact scenarios. However as Figs. 5.10a and 5.11a show, FEM model produces very severe deformation on core which can lead to numerical errors, inaccurate results and numerical instabilities for higher velocities. In the SPH Method depending on the deformation mechanism neighbouring particles can separate and as Fig. 5.11b illustrates core deformation is more realistic than that of FEM.

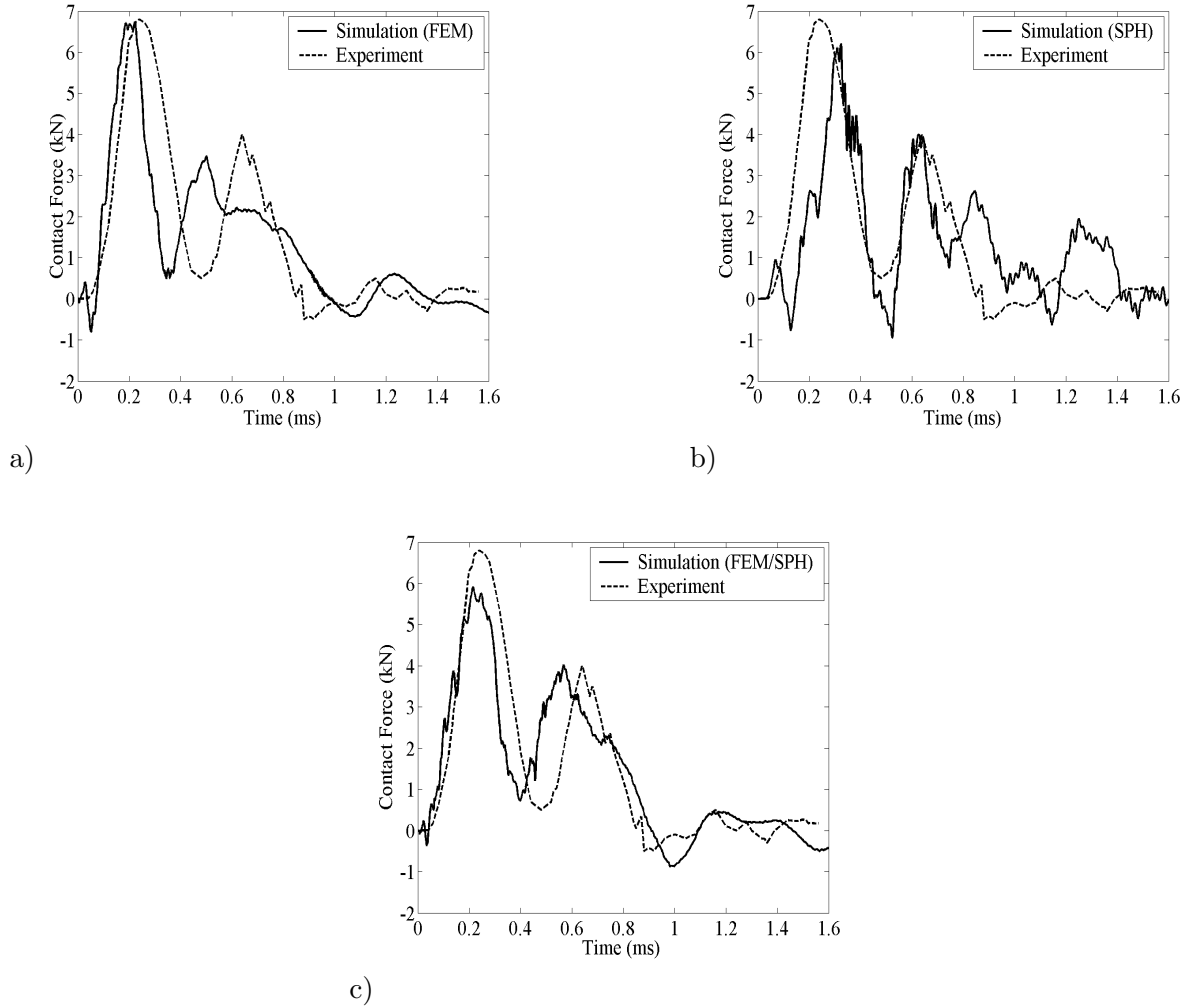


Figure 5.12: Contact force history of a) FEM vs. Experiment, b) SPH vs. Experiment and c) FEM/SPH vs. Experiment

Fig. 5.12b shows that the proposed SPH model for the sandwich core approximates the experimental impact force pulse quite accurately. However the initiation of the peak force is later than the experimental one and the pulse is more oscillatory than the FEM results and the experimental pulse. Fig. 5.12c shows the comparison of the contact force histories between experimental and numerical simulation with direct-coupled FEM/SPH Method. Here one can observe that the numerical pulse is not as oscillatory as in the SPH case since the topological connectivity is still in use outside the damage zone. The direct-coupled FEM/SPH Method approximates the impact pulse more accurately. The pulse duration which is important as well as the peak force value is very similar to the experimental one and better than the approximations produced by the pure SPH Method. Additional to the PEI core sandwich panels the accuracy of direct-coupled FEM/SPH Method has been tested in three different impact cases using



Figure 5.13: Glass impactors

a demonstrator sandwich panel with a hybrid PEI/Nomex core. The sandwich panel had thickness of 33mm, composed of 1.6mm carbon fibre/epoxy skins, with 10mm PEI foam next to the upper skin and 20mm Nomex core next to the lower skin. In this concept the PEI foam acts as a loadspreader in impact to generate more uniform impact loads into the honeycomb core. Three different impact scenarios have been chosen in which glass impactors (Fig. 5.13) with 21 and 29mm diameter were fired with the impact velocities of 65.8 , 95.1 and 108m/s. Therefore the efficiency of the direct-coupled FEM/SPH Method can be tested in a range of impact velocities showing different damage modes.

For the first comparison an impact case with a glass ball impactor 29mm in diameter and impact velocity of 65.8m/s has been chosen. The impactor damages the upper skin introduces an impact load on the core and bounces back, (Fig. 5.14a). In the second scenario an impactor 21mm in diameter has been impacted on the plate with an impact velocity of 108m/s. The impactor damages the upper skin, penetrates into the core and since its remaining kinetic energy is absorbed by the core it resides inside the sandwich plate. The damage zone is smaller that the previous case since the diameter of the impactor is smaller (Fig. 5.14b). In the last case a glass ball impactor 29mm in diameter and with an impact velocity of 95.1 m/s has been tested. The impactor damages the upper skin, penetrates into the core and since its kinetic energy was not absorbed completely by the core it continues its movement and damages the lower skin (Figs. 5.14c, 5.14d).

Since the hybrid core consists of both Nomex and PEI foam, the Nomex core has been modelled using classical FEs with discrete particles used for the PEI layer. For the Nomex layer a nonlinear fibre bi-phase material model with element elimination technique has been used, as discussed above. This technique eliminates the elements which reach a prescribed element strain threshold value. Note that Nomex is orthotropic in its



a)



b)



c)

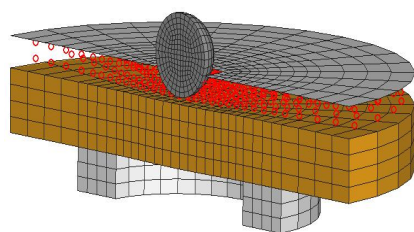


d)

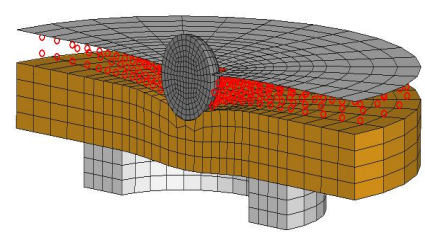
Figure 5.14: a) Impact damage on upper skin, b) damage on upper skin and core, c) damage on upper skin and core and d) backside damage

mechanical properties and is thus less suitable for a particle model which is intrinsically isotropic in the SPH formulation used here. Figs. 5.15a-d show the states of impact for the impact case with impactor 29mm in diameter and 65.8m/s impact velocity. The impactor damages the upper skin and compressed the PEI core. Discrete SPH particles are compressed together and the impactor damages the Nomex core. After crushing at small area in the Nomex core, the impactor bounces back. The damage area in the numerical investigation is larger than the experimental cases because of the element elimination technique used for modelling the damage of the composite skins. In the tests the damaged composite skin fragments and it continues to carry reduced loads.

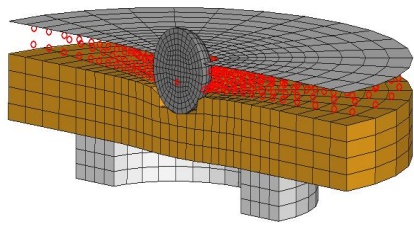
Figs. 5.16a-d show the states of numerical impact simulation in which an impactor



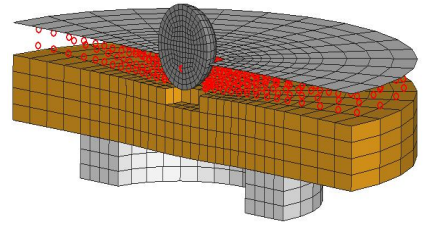
a)



b)

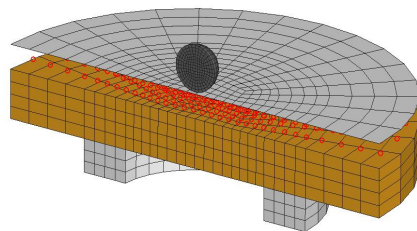


c)

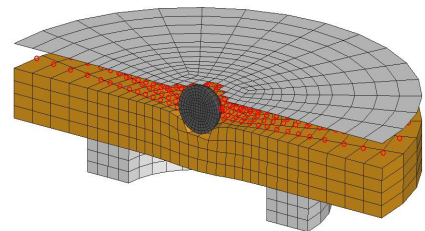


d)

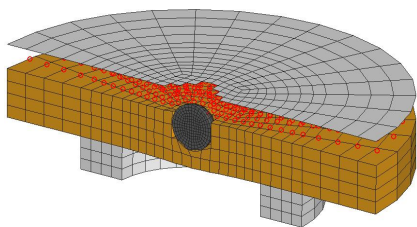
Figure 5.15: Impact states $V_o = 65.8\text{m/s}$: a) $t=0.16\text{ms}$, b) $t=0.36\text{ms}$, c) $t=0.72\text{ms}$ and d) $t=1.20\text{ms}$



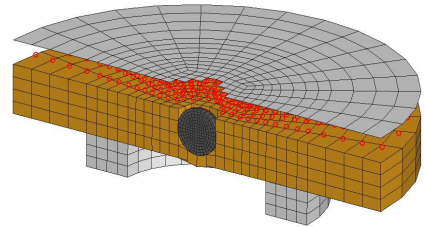
a)



b)

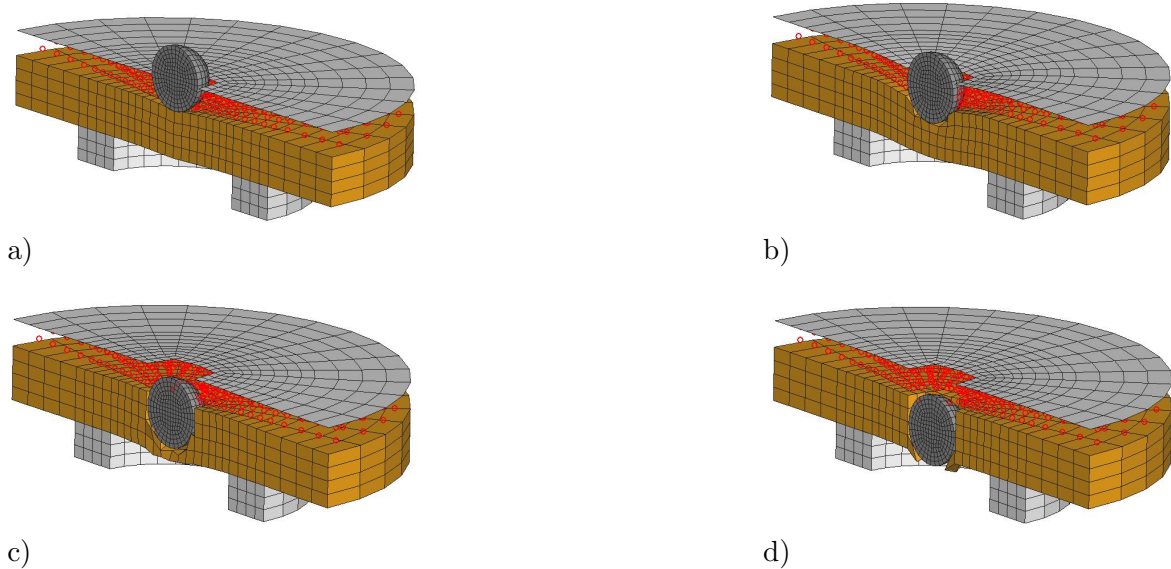


c)



d)

Figure 5.16: Impact states $V_o = 108\text{m/s}$: a) $t=0.16\text{ms}$, b) $t=0.20\text{ms}$, c) $t=0.36\text{ms}$ and d) $t=0.80\text{ms}$



21mm in diameter and with an impact velocity of 108m/s. The impactor damages the skin and firstly penetrates into the PEI core. The discrete particles are compressed together and since the kinetic energy of the impactor is not yet zero, it continues its movement. It penetrates into the Nomex core and causes a large deformation. During this deformation process the residual kinetic energy of the impactor absorbed by the Nomex core and impactor resides inside the sandwich plate. The same impact failure was observed in the experimental impact test. Figs. 5.17a-e show the last impact case in which an impactor 29mm in diameter with 95.1m/s impact velocity impact onto a hybrid core sandwich plate. The same impact stages can be also observed in this case. However the residual kinetic energy of the impactor is not absorbed by the Nomex core and the impactor continues its movement. The impactor damages the lower skin and rear face damage occurs. Fig. 5.17f shows the side view of the damage zone. Here one can also observe the deformation in the damage zone modelled with discrete particles. Again in this impact case the proposed direct-coupled FEM/SPH approximates the impact scenario very accurate and realistically.



Figure 5.17: Impact states $V_o = 95.1\text{m/s}$: a) $t=0.16\text{ms}$, b) $t=0.28\text{ms}$, c) $t=0.52\text{ms}$, d) $t=0.88\text{ms}$, e) $t=1.00\text{ms}$ and f) backside damage, side view

5.5 Discussion - SPH and Direct-Coupled FEM/SPH Method

In this work the results of impact simulations carried out for a sandwich composite plate with carbon fibre fabric/epoxy face skins and PEI foam core using SPH and FEM/SPH Method have been presented. The deformation pattern and the contact force histories obtained with pure SPH and direct-coupled FEM/SPH Method have been compared with that of experimental and pure FEM-based numerical results. The two approaches give quite accurate results. However since the computational time depends on the domain modelled by discrete particles, a direct-coupled FEM/SPH Method has been shown to be a good alternative for the numerical simulations where large deformation and element distortion are critical. Later to show the efficiency of the direct-coupled FEM/SPH Method in different velocity ranges three impact scenarios in which a hybrid core consisting of PEI and Nomex sandwich plate impacted by spherical glass impactors have been modelled. The direct-coupled FEM/SPH Method reproduces the impact failure modes and observed damage on the sandwich plates to a good approximation. The results demonstrated the capability of meshless SPH Method and its combination with FEM to be an effective candidate to overcome the drawbacks of FEM for modelling fragmentation failures in impact. The following work studies extensions of the method using a SAC of SPH and FEM and applying this to study crush response in composite energy absorbing structural elements.

5.6 Numerical Modelling of HVI Simulations - Semi-Adaptive Coupling

In this section for the prediction of impact damage of Nomex core sandwich panels under HVIs have been investigated using the proposed SAC technique. In the crush failure zone the FEs are replaced by the discrete particles during the impact. Here the transverse shear strain is used as adaptivity threshold. The numerical impact force and maximum penetration values are compared with those from experimental tests.

As mentioned in Chapter 3 for the modelling of cellular materials several modelling techniques are available, among them unit cell models and homogenised models. However computational expenses for unit cell finite honeycomb models increase rapidly as the number of cells increase. Additionally the unit cell models are highly mesh-dependent. In order to show mesh dependency of the crush behaviour two unit cell models with mm and 0.5mm mesh sizes have been used. Fig. 5.18 shows the deformation stages of the quasi-static compression test.

At low strains Nomex honeycomb deforms elastically then cell walls buckle. Compared to Al honeycomb Nomex honeycomb is relatively brittle. Therefore cell walls start to fracture after reaching a critical load value. As in the crushing of Al honey-

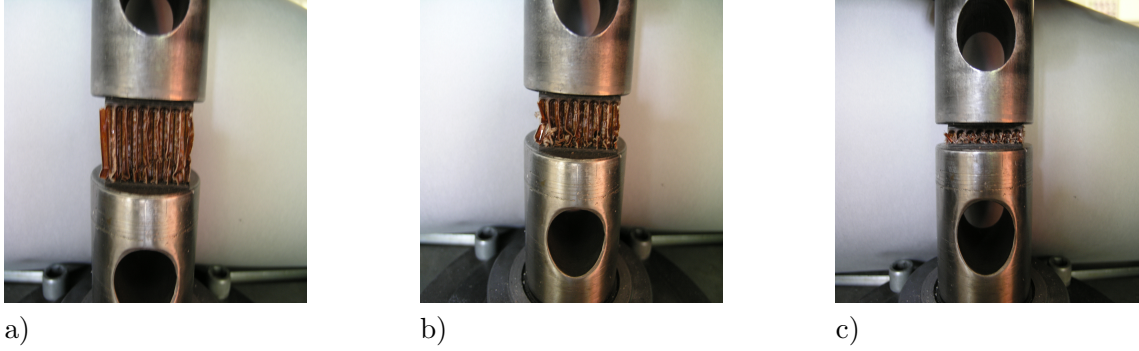


Figure 5.18: Stages of quasi-static compression test of Nomex honeycomb: a) buckling initiation, b) progressive folding and c) densification

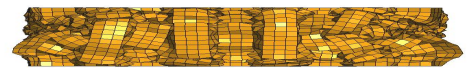
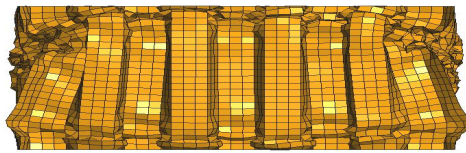
comb, cell walls collapse until densification. Fig. 5.19 shows the comparison between the experimental and numerical deformation patterns of the Nomex honeycomb using the micromechanical model. As one can see the deformation mode is global collapse which can be observed from the simulation results with 1mm elements. The numerical model with 0.5mm elements produces progressive collapse which was not observed in the experimental analysis. It should be remembered that the element thickness is 0.13mm, so that the use of thin shell elements of length 0.5mm here is questionable, and could cause different failure behaviour. The failure behaviour obtained by the micromechanical model with 1mm elements is comparable to experimental observations and this mesh size was used in the subsequent analysis.

As mentioned above in reality after reaching a critical load value, cell walls fracture under compression. In the micromechanical model since an elastic-plastic material model was used, the cell wall fracture was not highlighted by the numerical model. Fig. 5.20 shows the comparison between the load-displacement curves obtained by experiment and the numerical micromechanical model with 1mm mesh size. The micromechanical model gives reasonable agreement with the experimental crushing response. However since fracture is not included in the numerical model, the first peak load value predicted is due to local plastic folding which is lower and wider than the experimental one caused by brittle fracture of the aramid paper. However if unit cell modelling technique is applied on real aircraft structures such as composite fuselage core or leading edge the computational expense is the biggest drawback of this modelling technique.

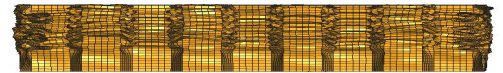
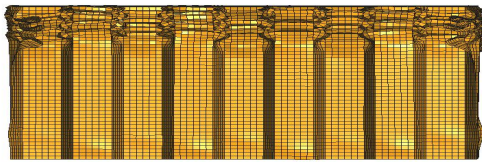
For the reasons given above the micromechanical model is computationally very expensive and is not suitable for structural analysis. Therefore the homogenised core model has been considered based on solid elements. However the material model proposed for the homogenised model uses EET for modelling of the cell wall fracture. The EET is based on the removal of the solid core elements reaching a critical strain threshold. If they are not removed at failure, the element compression strain distorts the element



a)



b)



c)

Figure 5.19: Stages of quasi-static compression of Nomex honeycomb at 30% and 60% compressive strain a) experiment (initial and 60% deformation), b) FE analysis with 1mm and c) 0.5mm element size

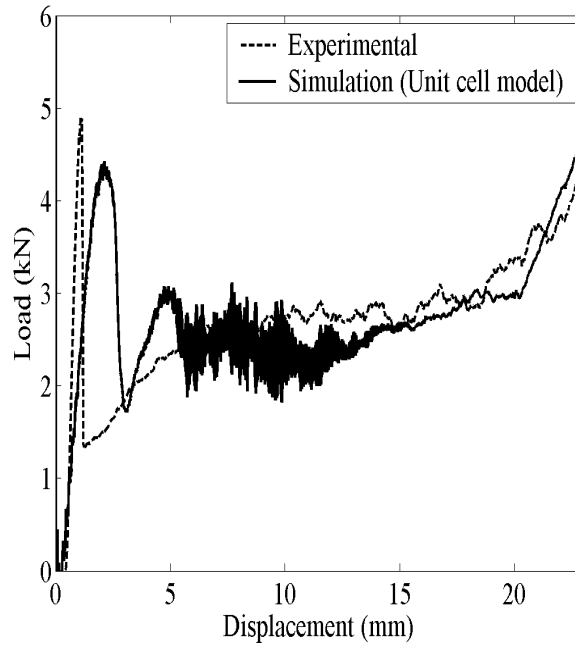


Figure 5.20: Comparison between the load-displacement curves obtained by experiment and the numerical model using micromechanical model of Nomex honeycomb in compression

geometry so much that the element length in the load direction becomes very small, which in explicit code simulations significantly reduces the time step and eventually causes run termination. Further, small changes in the strain elimination threshold can change the crushing mechanism drastically and introduce mesh dependency. Therefore it is numerically not effective. Hence the SAC technique described in Chapter 4 is applied to model the crushing behaviour of Nomex honeycomb more efficiently [166]. In this method when a critical element compression strain is reached the solid element is eliminated and replaced by discrete particles in an SPH formulation with an associated plastic compression crush materials law. The SAC technique is appropriate for modelling the Nomex core, which is orthotropic and hence not really suited to the SPH formulation used above for PEI foam cores. With the SAC technique it is possible to have orthotropic solid elements with correct mechanical properties, which are eliminated on reaching their failure strain and become replaced by SPH particles, which then have an isotropic elastic-plastic crush behaviour.

5.7 Discussion - Semi-Adaptive-Coupled FEM/SPH Method

Fig. 5.21 shows the comparison between the experimental and numerical stress-strain history of Nomex honeycomb core under through-thickness compression loads. The homogenised model can model the initial peak and plateau load value correctly. However

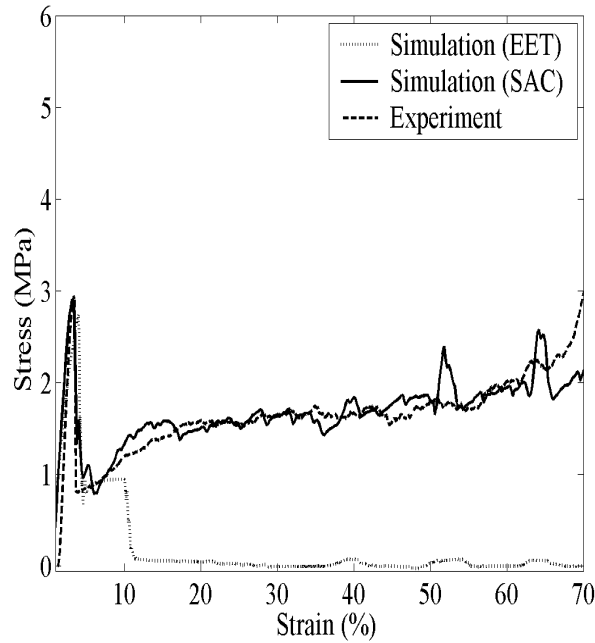


Figure 5.21: Comparison between the experimental and numerical stress-strain history of Nomex honeycomb under compression

after the elimination of the FEs at compression failure strains of about 10% the measured contact force drops down drastically and this causes lost contact information. In the SAC technique discrete particles replace the fragmented FEs after elimination and can model the crushing behaviour of Nomex honeycomb very accurately (Fig. 5.22), which shows the predicted crush deformation with the SAC model. The solid elements are eliminated at a predefined shear strain threshold. Then the damaged solid elements are replaced by discrete particles which are crushed further. The solid elements not converted into discrete particles have not yet reached the element elimination strain threshold. This hybrid modelling technique has few solid elements compared with the microscale models above and is thus suitable for efficient numerical analysis of honeycomb barriers and larger sandwich structures in crash or impact where the honeycomb core is severely crushed and has an EA function.

After having a stable crush model the technique has been applied to impact problem in which a projectile impacts on a composite sandwich panel. Here carbon fibre/epoxy facings were modelled with standard layered shell elements, whilst a homogenised model was used for the initial state of the Nomex honeycomb and SPH particles for the fragment representation. In this method when a critical element compression strain is reached the solid element is eliminated and replaced by discrete particles in an SPH formulation with an associated plastic compression crush materials law.

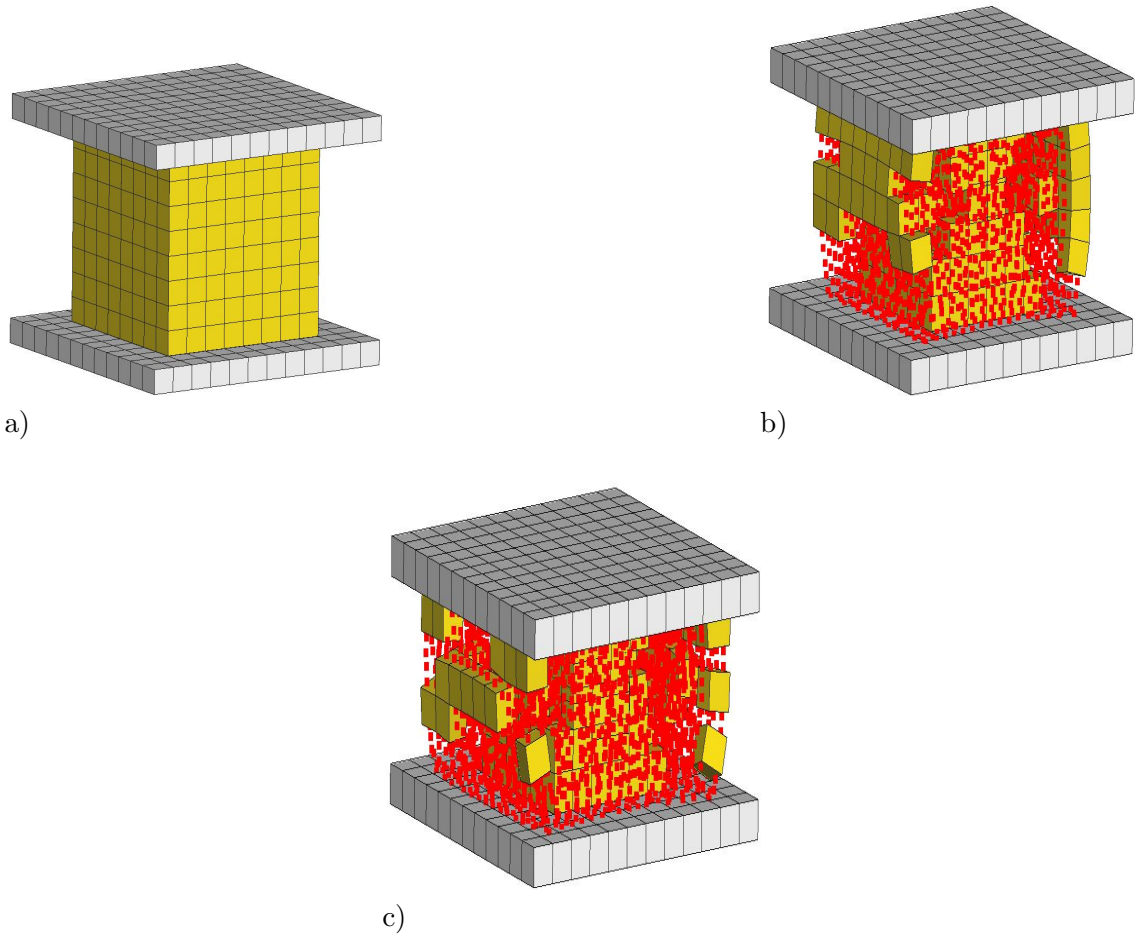


Figure 5.22: Application of SAC technique for modelling of Nomex honeycomb crush behaviour: a) homogenised FE model, b) 30% and c) 50% compression of core showing eliminated solids replaced by SPH particles

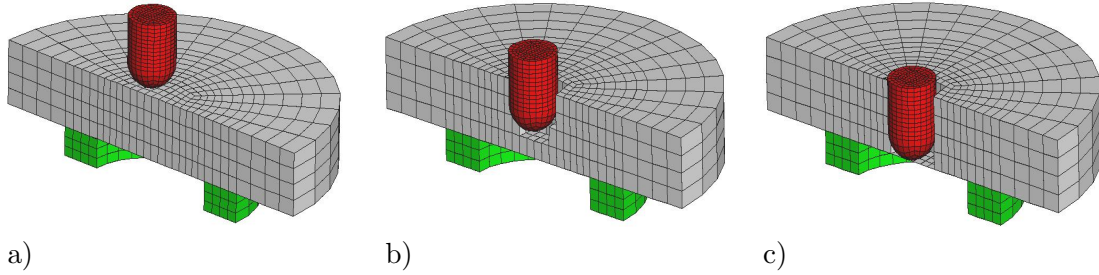


Figure 5.23: Numerical views of impact simulation using homogenised models: a) initial state, b) $t=0.4\text{ms}$ and c) $t=0.6\text{ms}$

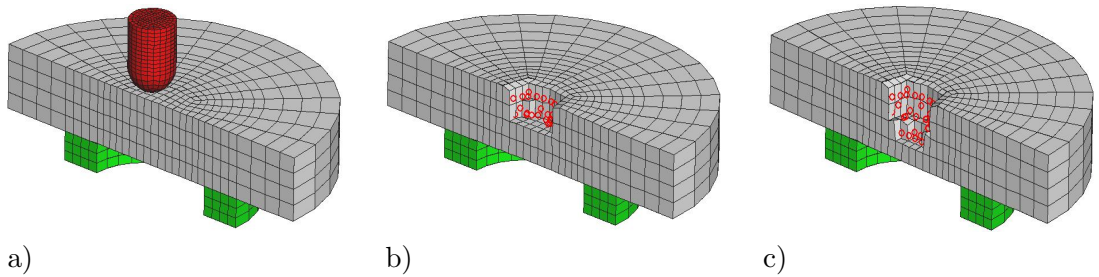


Figure 5.24: Numerical views of impact simulation using SAC technique: a) initial state, b) $t=0.4\text{ms}$ and c) $t=0.6\text{ms}$

Fig. 5.23 shows the numerical simulations of the impact test using homogenised FEM model with low strain threshold. After damaging the upper skin, the impactor penetrates into the Nomex honeycomb. Since the strain threshold is low, the homogenised core can not carry the impactor compression load and eliminates solid elements at further stages of the simulation. Hence the impactor reaches the lower skin and damages it. However in experimental investigations the lower skin damage was not observed. Just upper facing damage and core crushing were obtained.

Fig. 5.24 shows the stages of HVI simulation using SAC. Here homogenised Nomex honeycomb core has the same elimination threshold as in previous simulation. After the elimination of the FEs discrete particles represent the fragmented core debris and continue carrying compressive impact load.

The impactor now damages the upper skin, penetrates into the core and since its kinetic energy is absorbed by the upper skin and the core it does not reach the lower skin, agreeing with the test (Fig. 5.24). Fig. 5.25 shows the comparison of experimental and SAC-based numerical contact force histories. The proposed model estimates the first impact force peak as 5.4kN and the second one as 3kN . The experimental values are for these two peaks are 5.3kN and 3kN , respectively. Additionally the maximum penetration of the impact were also compared. The maximum penetration values for experimental and numerical investigations was also compared. The maximum penetration values for experimental and numerical investigations are 25mm and 27mm ,

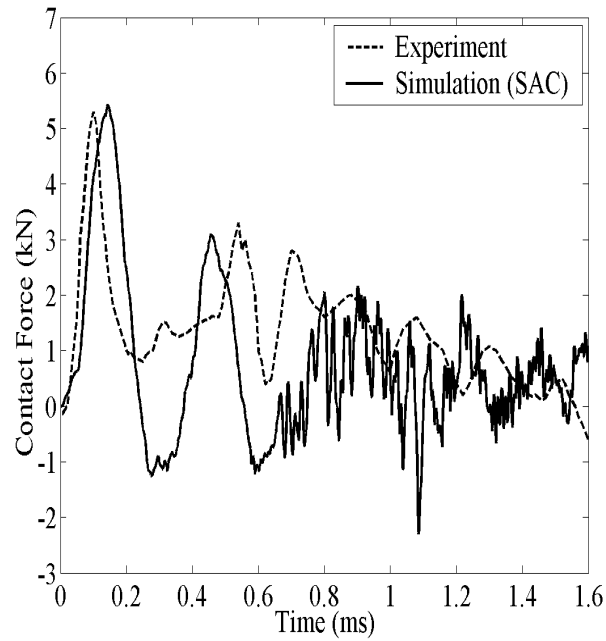


Figure 5.25: Comparison of experimental and SAC-based numerical contact force histories

respectively, which are in close agreement.

5.8 Final Discussion

In this section a new approach called SAC Technique has been proposed to model the impact damage response of the sandwich core previously modelled using EET. SAC Technique replaces the eliminated core elements which reaches the elimination threshold by discrete particles and allow stable computation. The efficiency of the approach was tested under both quasi-static compression and HVI loading and showed good correlations with the experimentally conducted investigations.

Chapter 6

Application of Meshless Methods in Crash and Energy Absorbing Structures

This chapter reports experimental and numerical analysis of quasi-static crushing of foam-filled Al thin-walled tubes and composite energy absorbers made of carbon-fibre-reinforced composites. It aims at showing the efficiency of alternative modelling approaches such as SPH Method, direct-coupled FEM/SPH and semi-adaptive-coupled FEM/SPH Method.

For both crashworthy analyses first the FE-based models are presented. Then to study the effectiveness of meshless methods for the foam-filled Al thin-walled tubes the SPH Method and direct-coupled FEM/SPH Method are used. Finally the composite energy absorbers are modelled with the SPH Method.

6.1 Experimental Investigations on Empty and Foam-filled Aluminum Crash Absorbers

In this section firstly the crashworthy analysis of empty and PS foam-filled single tube absorbers (height: 40mm and diameter: 25mm) is presented. In the first part of the study the foam filler is discretised using solid FEs. Later the above mentioned alternative SPH modelling approaches are used for the problem and the results compared with that of FEM.

Secondly, after obtaining a stable numerical model the crashworthy analysis of foam-filled (PS and Al foam) bitubular configurations (height: 27mm) are investigated. Bitubular arrangements have been chosen since they are the good representations of double-walled energy absorbing structures. Three different bitubular configurations were tested. These are shown in Fig. 6.1 and coded as BPH (interior: 25mm-diameter empty tube and exterior: 35mm-diameter PS foam-filled tube), BPP (interior: 25mm-

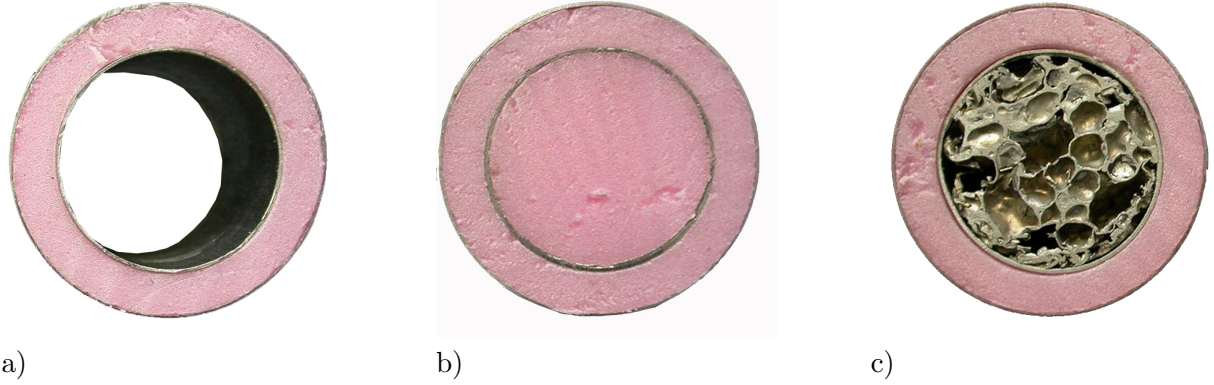


Figure 6.1: Bitubular configurations a) BPH, b) BPP and c) BPA

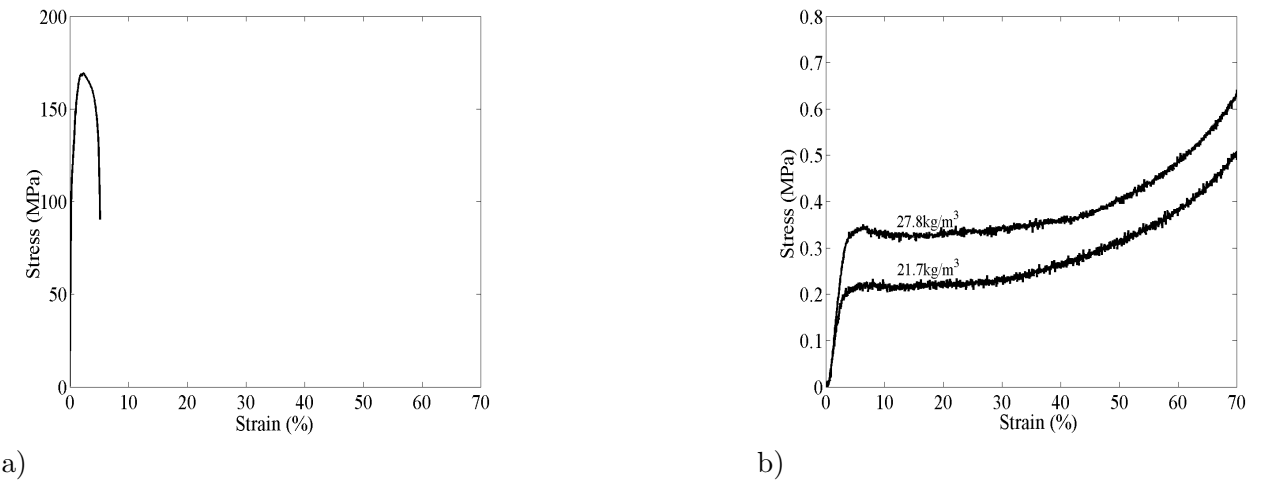


Figure 6.2: a) Tensional engineering stress-strain curve of Al tube material, b) quasi-static compression stress-strain curve of PS foam fillers

diameter PS foam-filled tube and exterior: 35mm-diameter PS foam-filled tube) and BPA (interior: 25mm-diameter Al foam-filled tube and exterior: 35mm-diameter PS foam-filled tube)

For the first part of the study the selected Al thin-walled tubes (99.7% Al), produced by Metalum Company of Turkey using a cold deep drawing process, were 25mm in outer diameter with a wall thickness of 0.29mm.

A typical quasi-static (10^{-3}s^{-1}) engineering tensile stress-strain curve of the tube wall material tested in accordance with ASTM B557M standard is shown in Fig. 6.2a. The relatively high strain hardening, seen in the inelastic deformation region of the curve, is most likely due to the cold forming process applied. Tubes were filled and tested without any heat treatment applied.

Thin-walled Al tubes were filled with a commercially available extruded PS foam

sheets manufactured by Izocam Company in two different average densities: 21.7 and 27.8kg/m³. PS foams are currently used as the filler in the inner layer of motorcyclist's helmets for impact-protection function, but their capabilities in thin-walled tubes as lightweight filler materials have not yet been investigated and modelled. As compared with expanded counterparts, extruded PS foams have more homogenous cell size and contain no weak boundaries of beads; hence are potentially more suitable materials for the filling of thin tubular sections. Uniaxial compression stress-strain curves of foams determined in accordance with ASTM 1621-91 on 40mm long cubic samples are shown in Fig. 6.2b. The curves show typical elastoplastic foam compression behaviour, composing of three distinct deformation regions: elastic, collapse (plateau) and densification.

Cylindrical foam fillers with an outer diameter that was slightly larger than the inner diameter of empty tube ($\sim 0.5\text{mm}$) were core drilled from the as-received PS foam sheets through the thickness direction. The foam filler samples were inserted into empty tubes tightly without imposing any damage to the cells. Compression tests were conducted on a fully computer controlled Schmadzu AGI universal testing machine. Test samples were compressed between two flat plates without any constraint applied to the ends of tubes. Compression tests on empty and foam-filled tubes, all 40mm in length, were performed at a deformation rate of 100mm/min, the same as that of compression tested foam samples.

For the bitubular arrangements the deep-drawn Al tubes received in 25mm (0.29mm in wall thickness and 27mm in height) and 35mm (0.35mm in wall-thickness and 0.27mm in height) in outer diameter were produced by Metalum Company of Turkey. As-received extruded PS foam sheets with dimensions of 50x600x1200mm were manufactured by Izocam Company of Turkey. The density of the PS foam was determined by dividing the mass of the cubic foam sample (50x50x50mm) by its volume and found to be 32.1kg/m³. The circular PS foam fillers were core-drilled through the thickness of the as-received foam sheet. Al closed-cell foams were prepared using the foaming from powder compacts (precursors) process at Izmir Institute of Technology. The detailed information on the foaming process and foam sample preparation is given in [167]. By simply changing the furnace holding time, foam plates having three different densities: 270, 350 and 430kg/m³ were obtained and used in filling of thin-walled Al tubes. The density of Al foam filler was determined by simply dividing its weight to its volume.

The crushing behaviour of foams samples and foam-filled tubes were determined using a computer controlled Schimadzu AG-I testing machine at a crosshead speed of 2.5mm/min. Fig. 6.3 shows the compression stress-strain responses of the Al foam fillers. The stress-strain curves of the foams show typical elastoplastic compression

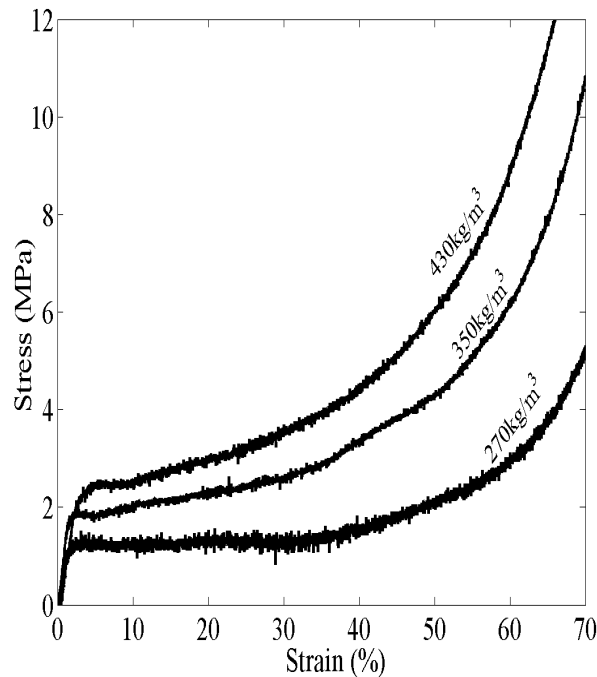


Figure 6.3: Compression stress-strain curves of Al foam fillers

behaviour, composing of three distinct deformation regions: elastic, collapse (plateau) and densification. As is seen in Fig. 6.3 the plateau stresses of Al foams are not constant in the collapse region and increase with increasing strain and foam density. The differences in cell size and cell size distribution cause the collapse of weak cells before the collapse of strong cells, leading to increase in the stress values in collapse region.

6.2 Numerical Modelling of Foam-filled Aluminum Crash Absorbers - FEM

The geometrical models were created in the commercial FE package ANSYS. Later the meshed geometrical models were exported to PAM-GENERIS in order to set the boundary conditions. The numerical solutions were carried out using the explicit FE code PAM-CRASH. PAM-VIEW was used as the visualisation tool post-processor.

The Al tubes were modelled using Belytschko-Tsay-4 node-thin shell elements. In foam-filled tube modelling (to save computational time) only one half of the tube was modelled due to symmetry. The foam filler and the compression test plates were modelled with 8-node solid elements. FE meshes of the quasi-static axial compression testing of empty and foam-filled tubes are shown in Fig. 6.4, respectively.

The compression test base and upper plates were modelled as rigid bodies. The dis-

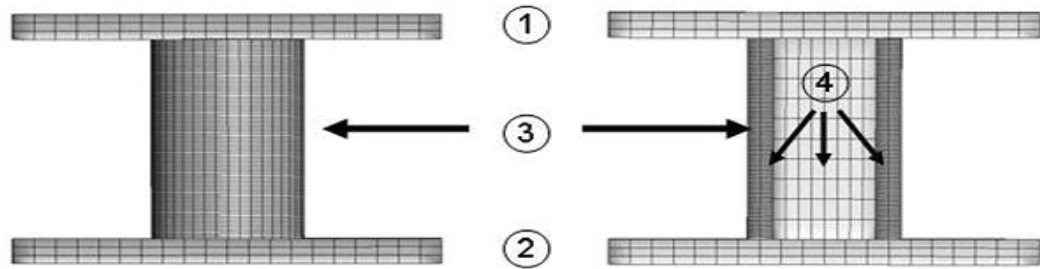


Figure 6.4: FE discretisation of a) empty tube (full model), b) foam-filled tube (half model), 1 and 2: compression test plates, 3: empty and foam-filled tube meshing and 4: foam-filler meshing

placements and rotations of the compression test plates were constrained except the displacement of the upper plate along the vertical axis. The movement of the upper load plate was fully determined by the movement of an artificial "node" located at the rigid body center of gravity. Boundary conditions for the rigid body were applied to the center of gravity node only.

PAM-CRASH Material type 103 corresponding to the elastic-plastic isotropic thin shell material was used for the tube material. Material type 103 uses an enhanced plasticity algorithm that includes transverse shear effects. It exactly satisfies Hill's criterion and precisely updates the element thickness during the plastic deformation.

The material behaviour of PS foam was modelled using the crushable foam (elastic-plastic) solid mode, namely PAM-CRASH Material type 2, which corresponds to solid materials exhibiting coupled volumetric bulk and deviatoric shear plasticity, as discussed before. Prior to the numerical investigation of foam-filled tubes, PS foam compression behaviour was simulated to validate the foam material model. The numerical simulations and experimental results were compared for each density of PS foam and the comparison is shown in Fig. 6.5. Agreement between numerical and experimental stress-strain curves shown in this figure is satisfactory for the modelling purpose.

Three contact models were used in the modelling: i) a tied contact between the base plate and the empty tube, ii) a node-to-segment contact between the upper plate and the tube ends and iii) a self-contact (self impacting contact with edge treatment) in order to prevent interpenetration between folds in the tube wall during plastic deformation. The self-contact impact algorithm of PAM-CRASH type 36 allows all slave segments to be defined in a given sliding interface. No segment orientation is specified, since the algorithm automatically detects penetrations and keeps in memory the

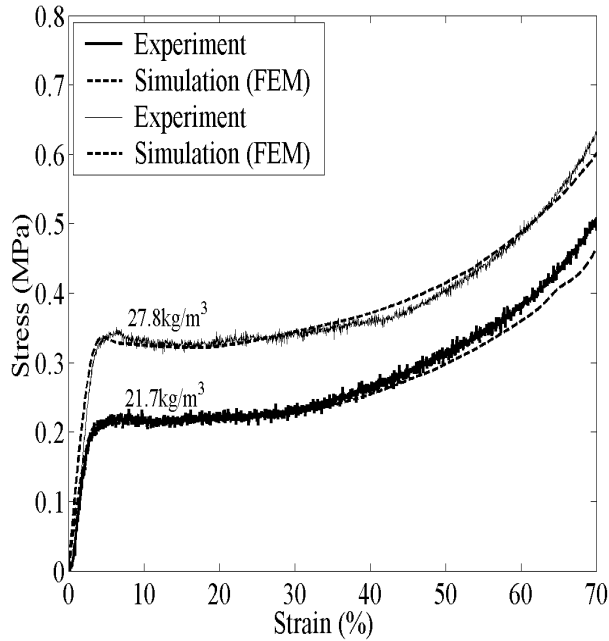


Figure 6.5: Quasi-static compression stress-strain curve of PS foam fillers

segment side from which a slave node comes into contact. The self-contact impact algorithm also uses a search algorithm, the so-called 3D Bucket sort algorithm in which the 3D slave surface is subdivided into a number of buckets and the slave nodes are recalculated in terms of bucket coordinates. Depending on the slave node bucket coordinates, its proximity to the slave segments is quickly determined. After the global search phase, an accurate local search algorithm is started.

The folding of the tube wall results in local deformation of and penetration into the foam filler surface. It was experimentally observed that the penetration depth through the foam filler surface was relatively small as compared with the radius of the filler (Fig. 6.6).

Based on this observation, a fine discretisation was applied to the foam filler near the tube wall surface, in order to reduce the computational time, as shown in Fig. 6.4. The mesh patterns are combined with a tied kinematic constraint type contact that connects two contact interfaces defined on two meshed parts of a structure that are close to each other but whose respective FE grids are not necessarily matching. Internal solid anti-collapse contact, namely PAM-CRASH contact type 10, was used additionally in order to prevent numerical problems that could arise when the solid elements of foam were heavily compressed and distorted. The option helps to reduce excessive compression; therefore, avoids too large drops in the stable solution time steps. This option also helps to avoid too large element distortions that may lead to ill-defined elements.

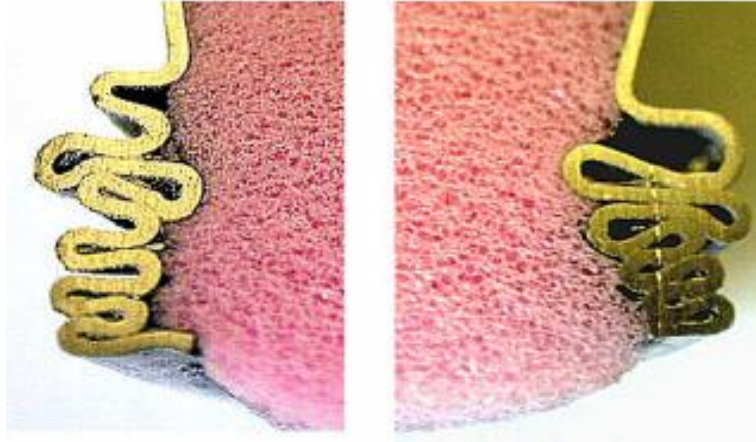


Figure 6.6: Penetration of the tube wall into foam filler

The interaction between the tube wall and the foam filler was defined via multiple segment-to-segment contact, PAM-CRASH contact type 23.

Multiple segment-to-segment contact uses an enhanced searching algorithm for detecting penetrations. Based on each master segment domain box, candidate slave nodes are searched by an efficient sorting method. For a given master segment at every time step, only its candidate nodes are checked for penetrations. Penalty forces are applied to those nodes which are judged to be penetrating the master segment.

Mesh optimisation

In FE analysis the number of FEs for a fixed geometry depend on element size and may significantly influence numerical results. The optimal FE mesh number has been established by refining the mesh until convergence is reached. The 25mm tube circumference was meshed with 40 elements and in order to determine the optimal size of mesh, the geometry was meshed with 20, 40, 80 and 160 elements along the height. The nomenclature used to describe the models is that 40x80 is to be interpreted as 40 elements along the circumference and 80 elements along the height.

Quasi-Static Simulation

The compression of empty and foam-filled tubes was performed at a cross-head speed of 100mm/min, corresponding to a deformation rate of $(4.16 \times 10^{-2} \text{s}^{-1})$ (the cross-head speed divided by the initial length of the tube) which is relatively slow for the dynamic numerical simulations since the explicit time integration method is conditionally stable when the time step is sufficiently small. Therefore in general very small time increments

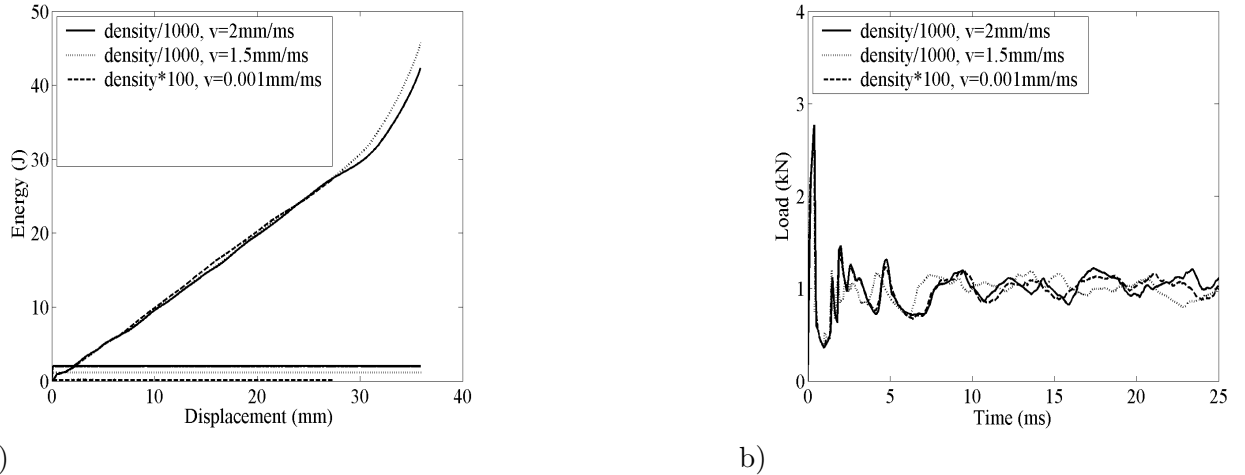


Figure 6.7: a) Kinetic and internal energy histories of 25mm empty tubes at various density scaling and deformation rates, b) corresponding load-displacement curves

have to be used. Contrary to implicit methods which are more efficient for relatively slow phenomena such as static strength and buckling problems, the explicit method is more efficient for very fast phenomena such as impact and explosion. Santosa et al. [23] however presented a procedure to achieve a quasi-static process using the explicit dynamics scheme by suggesting two alternatives; scaling down the material mass density and scaling the test speed up and scaling up the mass density and scaling the test speed down. The first one results in large number of time increments. The second alternative results in larger time step and therefore reduces the number of time step increment for such a low loading rate. In this present work, the loading velocity was scaled up to 2mm/ms and the material density was scaled down by a factor of 1000. The loading velocity was ramped up from zero and reached the required value after 0.01ms of the simulation and then was held constant.

As stated in the work Santosa et al. [23], the procedure above requires the control of two simulation parameters in order to verify the quasi-static process is being correctly modelled. First, the total kinetic energy should be very small as compared with the total internal energy over the period of crushing response. Second, the crushing load-displacement response of the system must be an independent function of the applied velocity. Therefore, as test example kinetic and internal energy histories of 25mm-diameter empty tube were carefully investigated using different mass density scaling and deformation velocities. Fig. 6.7a shows that kinetic energy is relatively smaller than the internal energy for the investigated three different mass density scaling-deformation rates combinations. It is also shown in Fig. 6.7b that the load-displacement responses of density-rate combinations are very similar. Based on efficiency and solution time considerations, numerical implementations were decided to be performed by scaling down the mass density with a factor of 1000 and with a loading velocity of 2mm/ms.

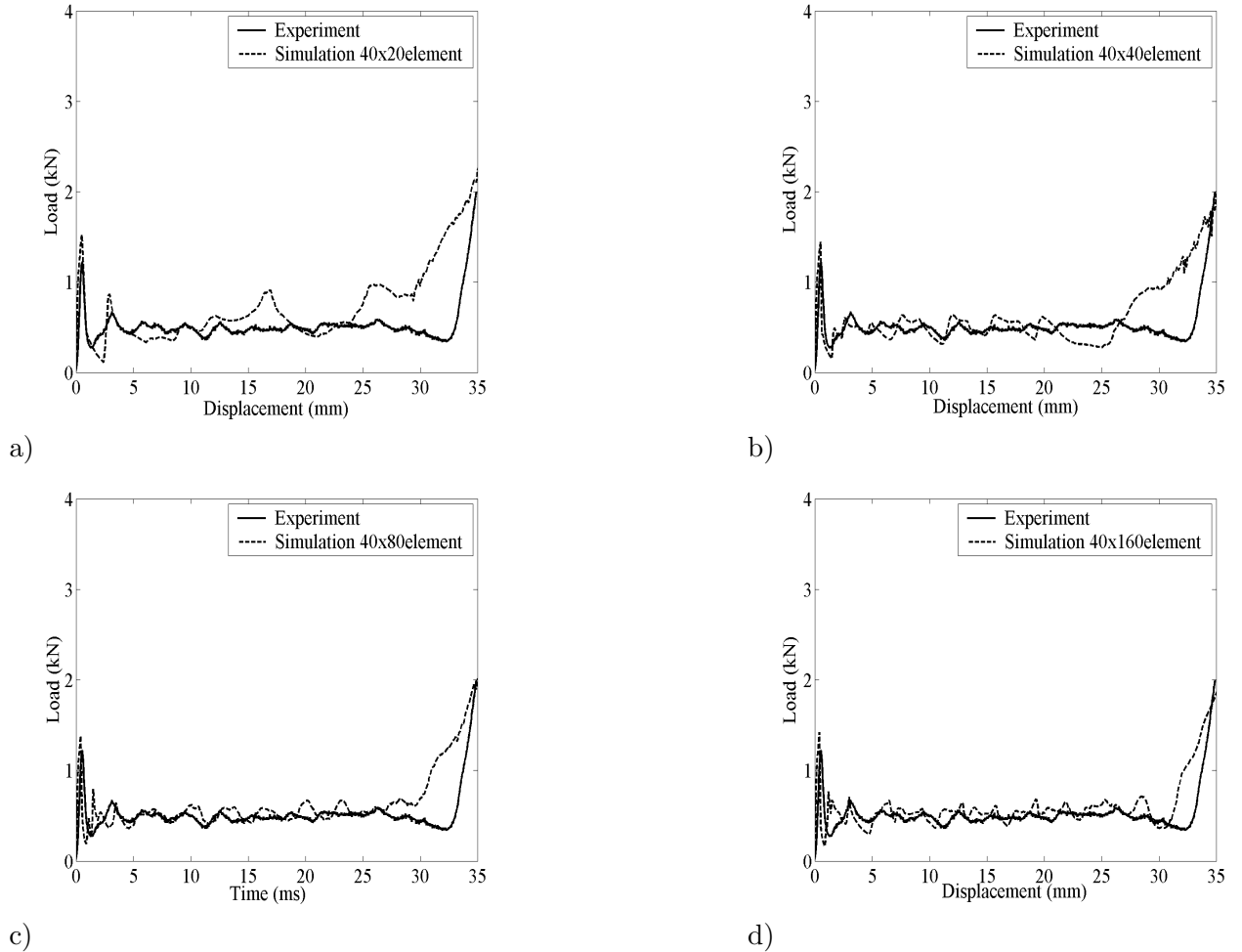
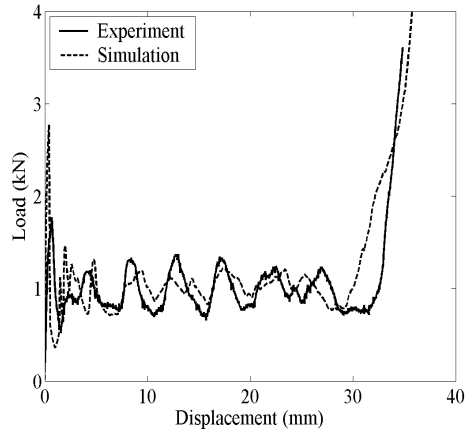


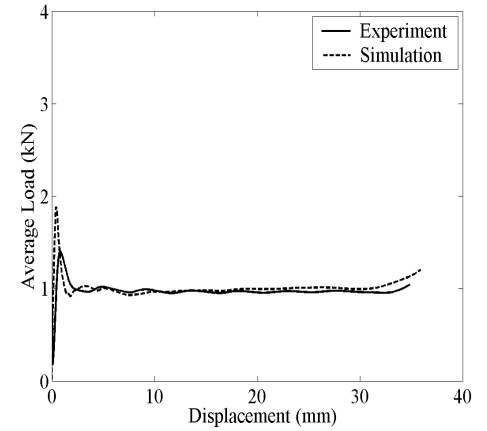
Figure 6.8: Numerical and experimental load-displacement curves of 25mm empty tube for different meshes along the height: a) 40x20, b) 40x40, c) 40x80 and d) 40x160

Empty Aluminum Tubes

The load-displacement curves of empty tube models constructed with four different numbers of elements; 40x20, 40x40, 40x80 and 40x160, are shown sequentially in Figs. 6.8a-d for 25mm tube, respectively. In these figures for the purpose of comparison experimental load-displacement curve of 25mm empty tube is also shown. As seen in Figs. 6.8c-d, the load-displacement curves of models with 40x80 and 40x160 elements give reasonably good agreements with the experimental load-displacement curve while the load-displacement curves of models constructed with 40x20 and 40x40 elements show substantial disagreements. The similar effects of number of elements on the load-displacement curves of 25mm empty tube were also found. FE models were however continued with 40x80 elements for both tube geometries for the computational efficiency.



a)



b)

Figure 6.9: a) Comparison of experimental and numerical load-displacement curves of 25mm empty tube, b) comparison of experimental and numerical average load-displacement curves of 25mm empty tube

It was experimentally and numerically found that 25mm empty tubes deformed in diamond mode and corresponding experimental and numerical load-displacement and average load-displacement curve shown in Fig. 6.9, respectively. The agreement between experimental and numerical average load values is quite satisfactory except in the initial and densification regions of the load-displacement curves, corresponding to the points of the first and the last fold formation. Totally 7-8 folds formed in 25mm empty tubes.

The experimental and model deformed shapes of empty 25mm tubes corresponding to the deformation ratios of 15%, 30% and 50% are sequentially shown in Fig. 6.10. The model deformed shapes exactly matched to the experimental deformed shapes, which again confirmed the agreement between model and experiments. It is also noted in model and experimental deformed shapes of Fig. 6.10 that folding started in asymmetric mode before reverting into diamond mode in both tubes, a phenomenon observed in multi-mode collapse mode [168].

Filled Al tubes

The foam filling in 25mm tube switched the collapse mode from diamond to concertina mode and again model and experiment show very similar deformed shapes (Fig. 6.11) and load-displacement curves (Fig. 6.12). The effect of foam filling is to reduce the fold length and hence to increase the number of folds formed (9-10), a result which was also previously found in foam-filled Al and steel tubes [21]- [23], [29].

The restraining effect of foam filler on the fold formation was considered to be the

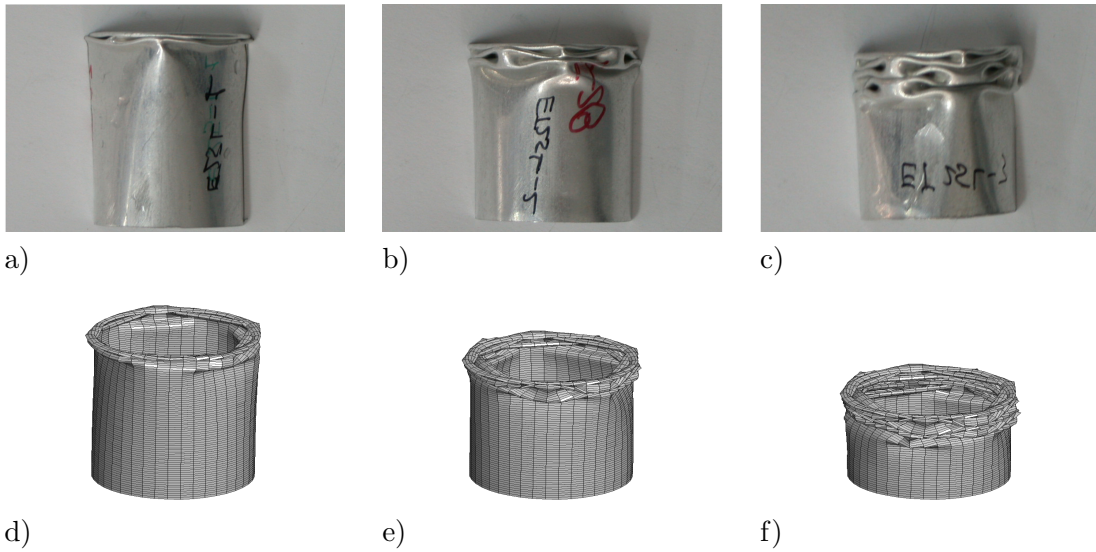


Figure 6.10: Deformation histories of 25mm empty tube at various percentage deformation ratios: a-c) experimental, d-f) numerical

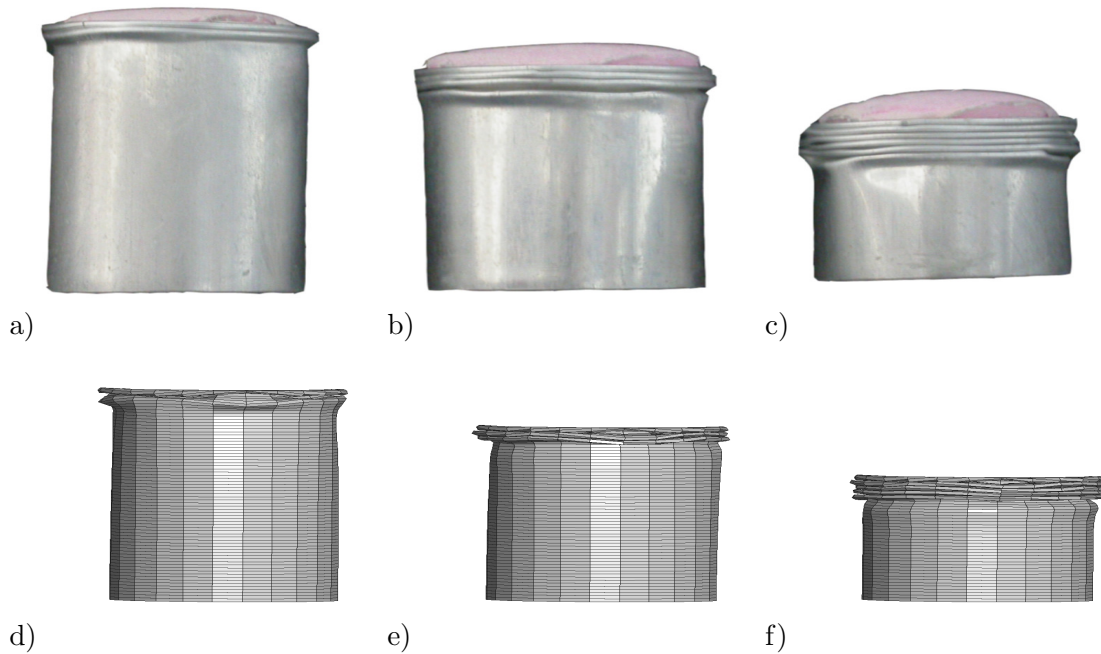


Figure 6.11: Deformation histories of 25mm 27.8kg/m³ PS foam-filled tube at various percentage deformation ratios: a) experimental, b) numerical

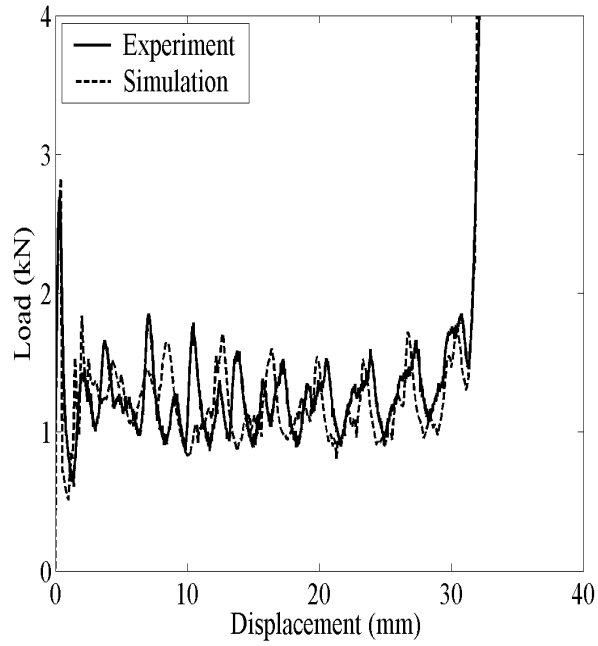


Figure 6.12: Numerical and experimental load-displacement curves of 25mm 27.8kg/m³ PS foam-filled tube

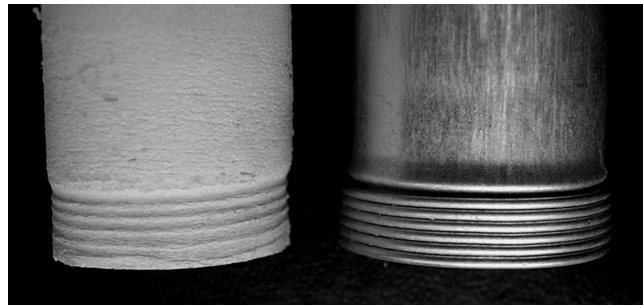


Figure 6.13: Images of side views of partially deformed 25mm 27.8kg/m³ PS foam-filled tubes at 30% deformation; filler and tube surfaces

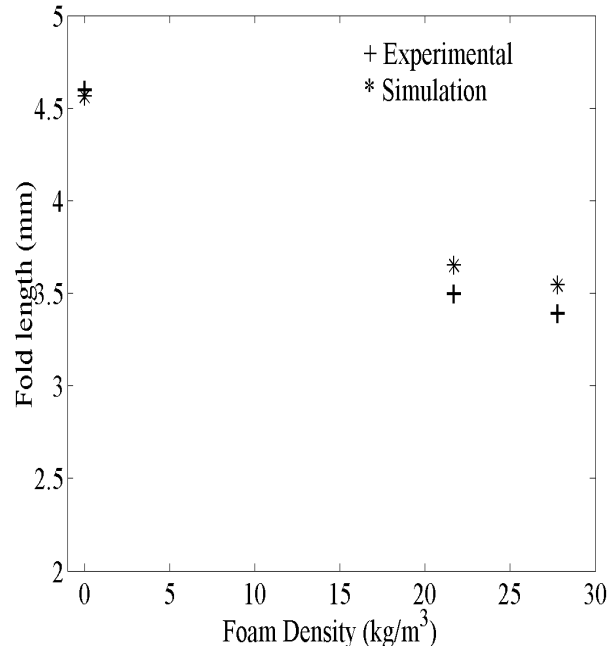


Figure 6.14: Numerical and experimental fold lengths vs. foam density

major cause of the reduced fold length in filled tubes. The entrance of the column wall into foam filler results in shorter fold lengths and increases the number of folds formed [22]. Santosa et al. [23] stated that the encroachment of the column wall into the Al foam filler allows an additional compression in the foam and retards the sectional collapse of the column. A similar filler-tube encroachment effect is also seen on the surface images of partially crushed foam-filled tube's fillers and tubes in Fig. 6.13.

For comparison the experimental and numerical fold lengths of tubes as function of foam density are shown in Fig. 6.14. The numerically measured fold lengths are slightly higher than the experimentally measured fold lengths and the effect of increasing foam density is to reduce the fold length as seen in Fig. 6.14, confirming the restraining effect of foam filler to tube wall folding; the higher the density of foam filler the higher the resistance to tube wall folding.

The change of collapse mode from diamond into concertina with foam filling was also observed previously in Al foam-filled Al and steel tubes, polyurethane foam-filled Al tubes and wood sawdust-filled plastic tubes [19], [23], [169]- [171] and it was proposed to be due to the thickening effect of foam filling, which drives the deformation shift from diamond to concertina. It was also shown by Hanssen et al. [169] that at a critical Al foam density the deformation mode in filled Al tubes shifted from diamond to concertina mode. A similar mode-shift was also found in polyurethane foam-filled thin-walled Al tubes with the increasing of foam density [19]. For the present work, it

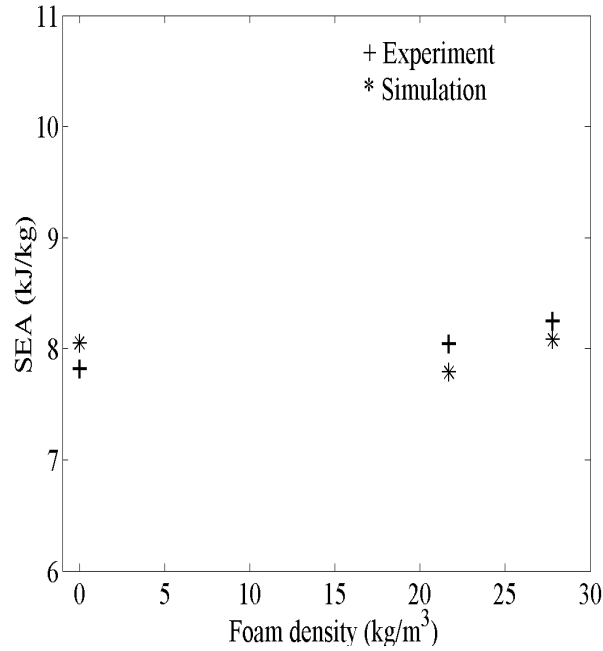


Figure 6.15: Numerical and experimental SAEs (at 50% deformation) in tubes as function of foam density

is quite possible that the foam densities used are higher than the critical foam density for the mode-shift in 25mm tube. The experimental and numerical SEAs corresponding to the 50% deformation of empty and foam-filled tubes are shown for 25mm tube in Fig. 6.15.

Again, experimental and numerical SEAs agree well with each other; the maximum difference between them is 2%. It is also noted in Fig. 6.15 that lower density foam filling (21.7kg/m³) is almost ineffective in increasing the SEAs of the filled tubes over those of empty ones. The percentage increase in SEA in higher density foam filling (27.8kg/m³) is found numerically 1.5% and experimentally 5% for 25mm tubes. These results also show agreement with the study of Guillow et al. [19] in that the average crushing load of foam-filled tube is higher than that of simply addition of crushing loads of empty tube (alone) and foam filler (alone). It should however be stated here that the comparison of the EAs between empty and filled tubes should be made on the equal mass basis by taking into consideration the thickening of the empty tube wall. Previous studies on Al foam-filled tubes and boxes have shown that there existed a critical total filled tube mass and the corresponding critical foam density above which the use of foam filling became more efficient than the empty tube [22], [29], [172]- [174]. The effect of PS foam filler density and the critical total mass of filled tubes should be further investigated numerically and experimentally for efficient crash element designs.

6.3 Discussion - FEM

In general, satisfactory agreements were found between the results of FE modelling and experimental quasi-static crushing tests of empty and PS foam-filled thin-walled Al tubes. The model and experiments have also highlighted several effects of foam filling in thin walled Al tubes. The number of folds formed in foam-filled tubes, both in diamond and concertina mode of deformation, increased with foam filling and also with increasing foam filler density. It was further found that the restraining effect of filler shifted the deformation mode from diamond to concertina in the larger diameter tube investigated. The EAs in foam-filled tubes were shown to increase with increasing filler density and higher than the sum of the EAs of empty tube (alone) and filler (alone).

6.4 Numerical Modelling of Foam-filled Aluminum Crash Absorbers - SPH and Direct-Coupled FEM/SPH Method

Although the above proposed FE mesh-based model can be used for the crashworthy analysis of foam-filled Al crash absorbers, in general the modelling of crash and impact scenarios based on FEs are complex. It is difficult to simulate large deformation and structural failure in FEM since FEM is based on a continuum mechanics formulation requiring element connectivity. Additionally in explicit analysis the time step depends on the size of the elements in the simulation. Large deformations may cause small time steps, element distortion, hourglassing resulting in error termination. Additionally time consuming discretisation and requirement of special treatments (in above mentioned example mesh coupling between fine and coarse discretisation) are the drawbacks of FEM based analysis. Therefore in the second part of this section, a meshless SPH Method and an FEM/SPH coupling technique were used to model PS foam filler deformation. Beside the advantages of its meshless nature, as a result of the dynamic neighbouring search algorithm, the SPH Method is computationally expensive. One alternative numerical solution technique that is commonly used is coupling, as explained in Chapter 4. Since SPH uses a Lagrangian formulation, a possible coupling between SPH and standard Lagrangian FEM is straightforward using contact interfaces. This means a coupling between discrete smoothed particles for the parts where large deformation occurs and FEs for the parts where small deformation takes place is possible. Coupled FEM/SPH technique has been chosen here to investigate the efficiency of coupling for large deformation analysis. In the coupled FEM/SPH technique, discrete particles were used to model only the deformation zones of severe element distortion which cause hourglassing and tube wall penetration, while the major part of the PS foam filler was modelled with FEs. The numerical results including deformation modes, load-deformation histories, fold length and SAE values were compared with the results of experimental and FEM numerical analysis.



Figure 6.16: Discrete particle modelling of foam filler: a) general, b) detailed view



Figure 6.17: Coupled solid element/discrete particle modelling of foam filler: a) general, b) detailed view

Meshless Modelling of PS Foam Filler

The fully discrete particle and direct-coupled solid element/DE model of the filler in the foam-filled tube are shown sequentially in Figs. 6.16- 6.17. Discrete particles and solid elements are coupled with kinematical type tied contact algorithm that allows the stable computations without distortion. The material model used for discrete SPH particles was an isotropic elastic-plastic-hydrodynamics solid material model, of which an EOS was used to model the pressure-volume relation, as explained in Chapter 4. Discrete particles were generated with a simple transformation of FE mesh into mass points.

Since the computational time is related with the number of particles and their contact search duration the optimum number of particles in SPH model and the number of solid elements and particles for coupled FEM/SPH approach have been investigated. First of all the initial solid discretisation of the foam filler was considered. The fine

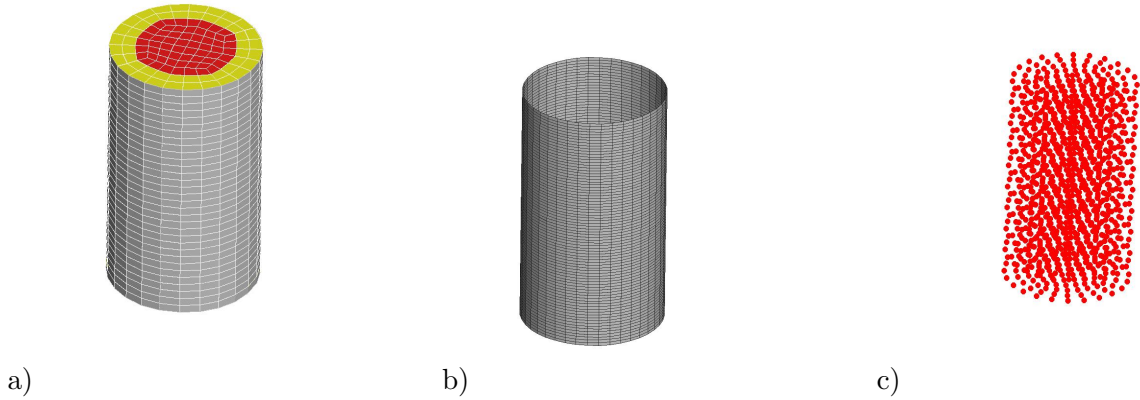


Figure 6.18: a) The initial FEM model for the SPH and direct-coupled FEM/SPH modelling: a) 1: Central deformation zone, 2: Tube interaction deformation zone, b) conversion of solid elements into discrete particles and c) discrete modelling of foam-filler

discretisation near the tube wall (Tube interaction deformation zone) was removed and this area meshed with the same mesh size as the central deformation zone of foam filler. For the characterisation of the foam material same interaction parameters are used in SPH and direct-coupled FEM/SPH modelling.

As mentioned in Chapter 4 in discrete particles can be compressed under compression load as FEs. Therefore for the modelling of foam filled, using a compression test simulation the material parameters can be obtained for further numerical simulations. Fig. 6.19 shows the comparison of the compression responses of discrete- and FE-modelled foam specimen with the experimental results. SPH Method may suffer from the boundary problems the numerical compression test setup extended to a constrained compression setup and the response of FEs and discrete particles is also compared under constrained conditions. Since for the crushing behaviour of foam-filled tubes both FEs and discrete particles are constrained by the tube wall the constrained compression test (Fig. 6.20) helps obtaining proper material response of the foam filler using DEs.

Fig. 6.21a shows the upper view of the discrete particle distribution of the initial model. Since the discrete particle distribution is based on the previously used FE discretisation, the particles are distributed equidistant. In order to show the effect of particle distribution on the crash response a model in which equidistant distribution (in crush direction too) of the particles used proposed. The distance between the SPH particles kept constant to obtain a homogeneous distribution of interaction. Since the change in the number of particles resulting from the change of smoothing length affects the model results, the model was constructed in a way that the results were stable concerning the interaction between the particles.

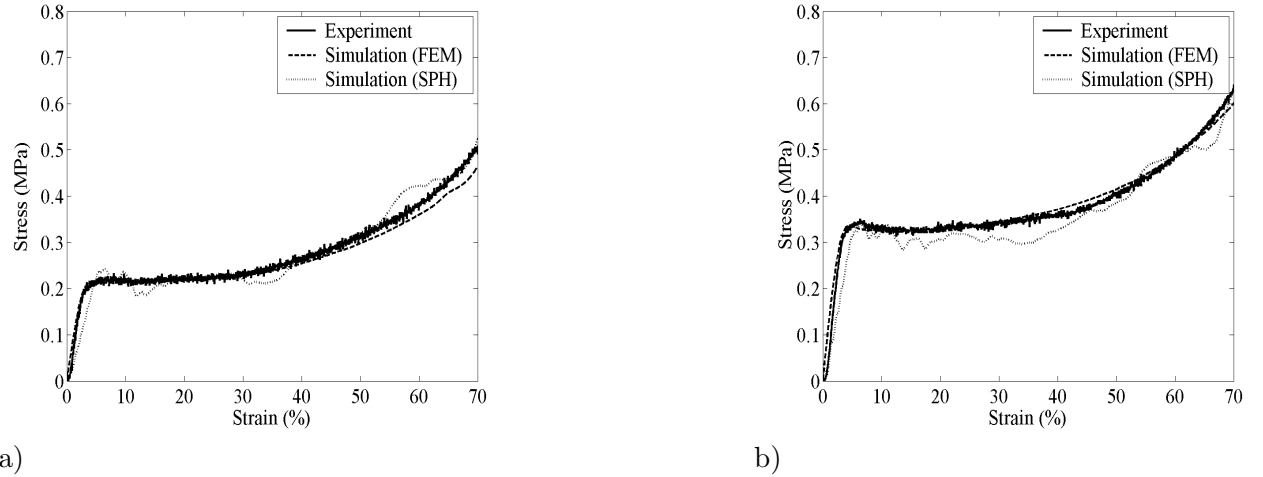
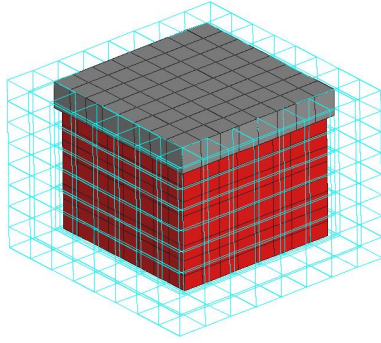


Figure 6.19: Comparison of compression responses of PS foam with the density of a) 21.7kg/m^3 , b) 27.8kg/m^3 using FEM and SPH

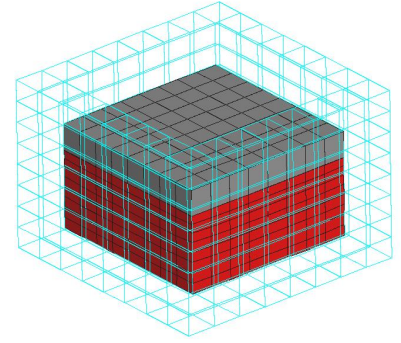
Fig. 6.22 shows the comparison of load-displacement curves of abovementioned models. The crush responses of the three models have the same characteristics and as expected the model with fewer particles gives the lower load level. The initial model and model with double number of particles give almost the load levels however in terms of computational time the former model is cheaper.

Another interesting aspect is the comparison of the deformation modes. Fig. 6.24 shows the numerical deformation modes of the foam-filled tubes at 50% deformation. As mentioned in the previous section the PS foam-filled tubes deform in concertina mode which was obtained with the initial model.

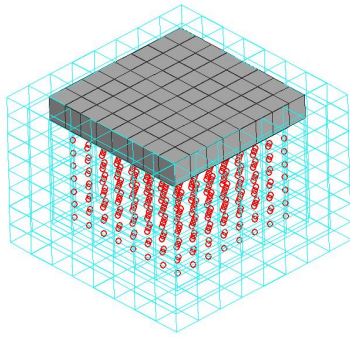
The model with half number of particles, depending on the lack of interaction between the particles and the tube wall, gives larger fold lengths and diamond deformation mode. The model with double number of particles results in mixed-mode in which contains some concertina deformed folds. Therefore the initial model gives satisfactory agreements with the experimental investigations in terms of deformation mode. In the simulations with SPH Method the interaction between the particles is one of the key issues in modelling. The smoothing length is the driving parameter for the interaction zone for a particle. Fig. 6.25 shows the effect of maximum smoothing length on the crush force. For this investigation the initial numerical model was used for the further simulations. The higher the maximum smoothing length the higher the final crush load. This is the result of the increased number of neighbouring particles which a reference particle has contact. It can be concluded that the numerical model developed can highlight the different aspects of the discrete modelling of a solid domain.



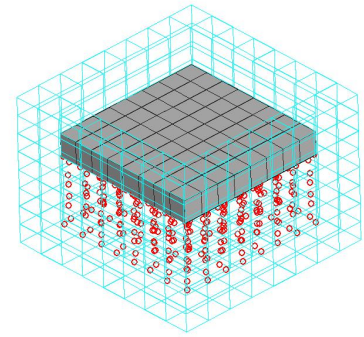
a)



b)

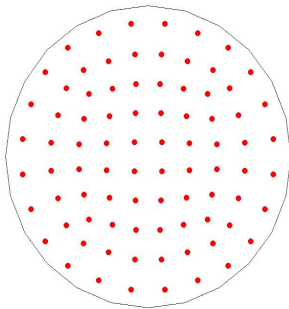


c)

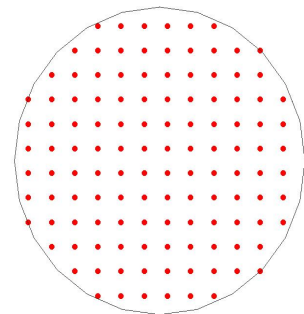


d)

Figure 6.20: Initial states (a and c) and 30% compression strain (b and d) of FEs and discrete particles under numerical constrained compression setup



a)



b)

Figure 6.21: a) Initial distribution of the particles, b) equidistant distribution of the particles

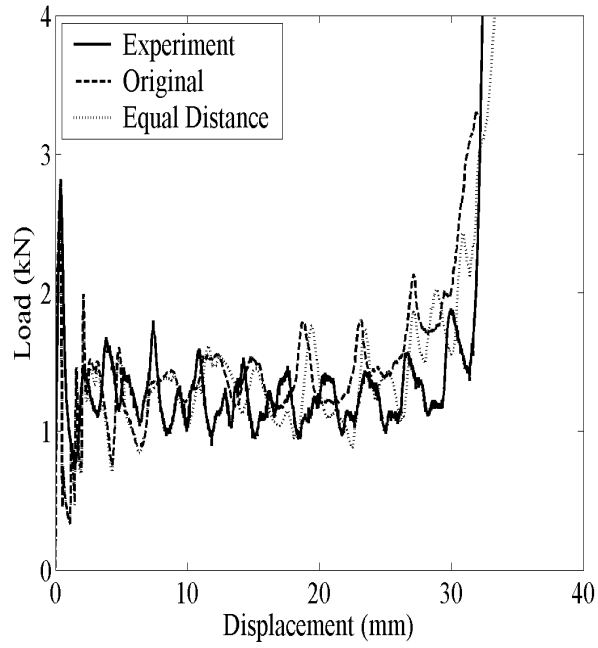


Figure 6.22: The comparison of load-displacement response of particle distribution (Original: initial particle distribution, equal distance: equidistant particle distribution)

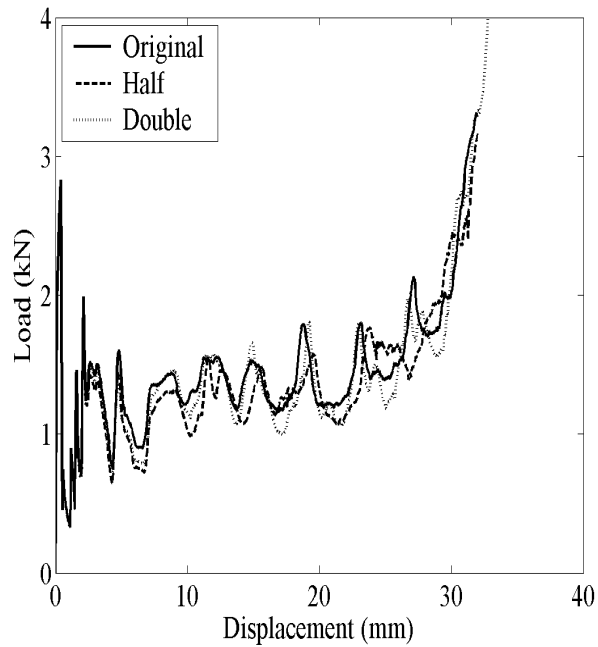


Figure 6.23: The comparison of load-displacement response of number of particles (Original: 1296 particles, half: 648 particles and double: 2592 particles)

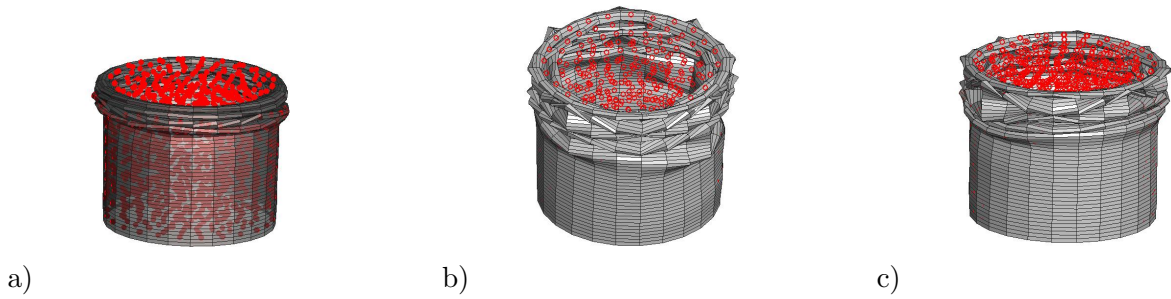


Figure 6.24: The numerical deformation modes at 50% compression: a) Initial model, b) model with half number of particles and c) model with double number of particles

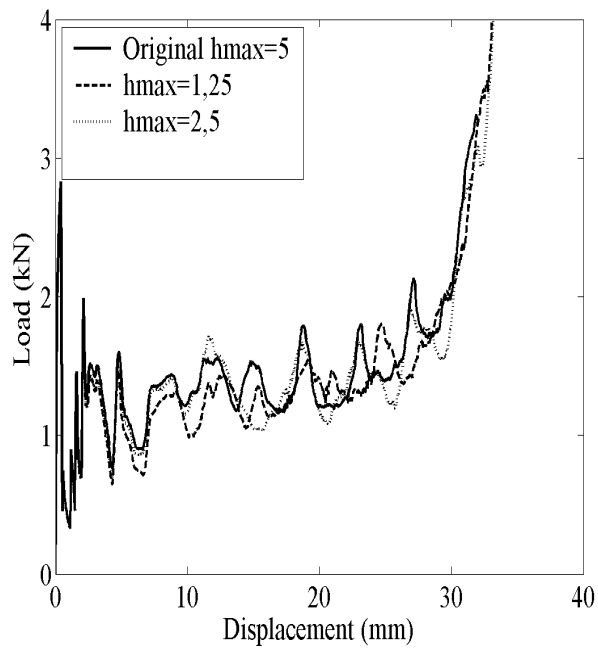


Figure 6.25: The comparison of load-displacement response of maximum smoothing length

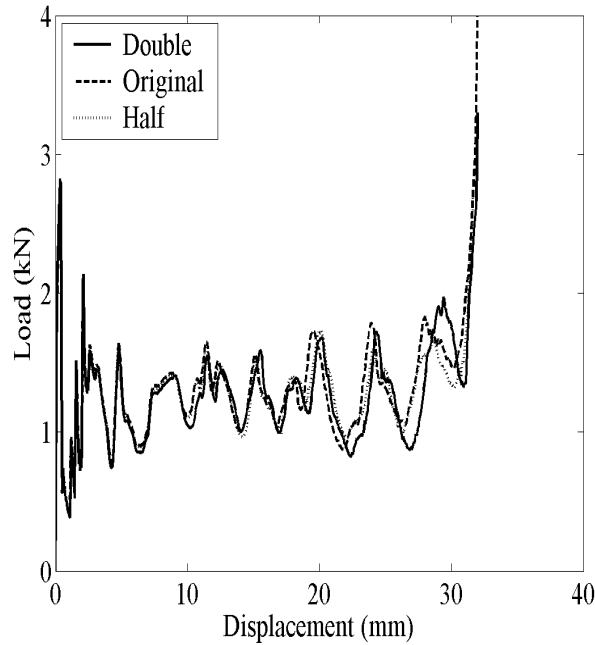
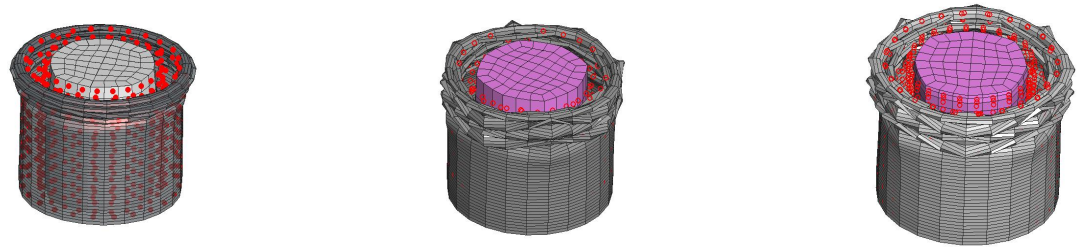


Figure 6.26: The comparison of load-displacement response of number of particles and solid elements: Original: 576 particles/600 FEs, half: 288 particles/300 FEs, double: 1152 particles/1200 FEs

For the direct-coupled FEM/SPH model also a mesh optimisation analysis was conducted. The direct-coupled model consists of 720 particles (12x48) and 600 (12x50) solid elements. Two models which contain half and double of the number of particles and solid elements, 288 particles (6x48) and 300 (6x50) solid elements, 1152 (24x48) particles and 1200 (24x50) solid elements, respectively. Fig. 6.26 shows the comparison between the load-displacement curves of the models with different number of particles and solid elements. The three proposed discretisation give similar results however the model with half number of particles and solid elements give relatively lower crush force value. Fig. 6.27 shows the deformation mode of PS foam-filled tubes at 50% compression. The experimentally observed concertina deformation mode was also numerically observed with the initial model. The model with half of the number of particles and solid elements deforms in diamond mode with larger fold length depending on the reduced contact between the particles, solid elements and tube wall. A mixed-mode deformation was obtained with the model using double the number of particles and solid elements.

It is noted that the deformed shapes and load-displacement curves of FEM show good agreement with the experimental results. As the foam filler experiences relatively large deformations, the sizes of solid elements become smaller, particularly in the region where the tube wall interacts with the filler. Since an explicit numerical scheme is used

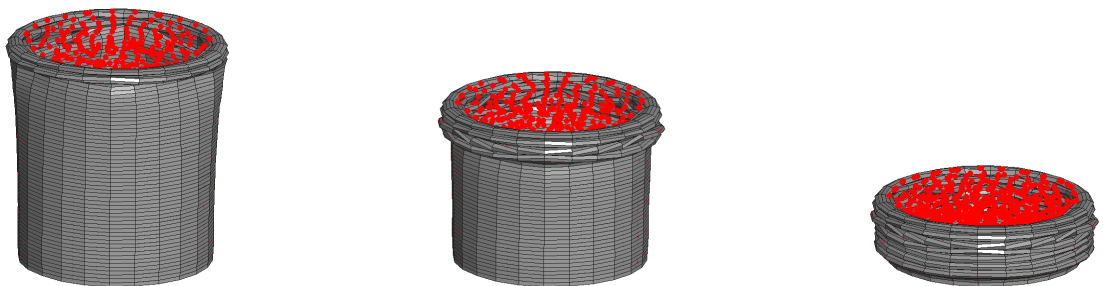


a)

b)

c)

Figure 6.27: The numerical deformation modes at 50% compression: a) Initial model, b) model with half number of particles and solid elements and c) model with double number of particles and solid elements

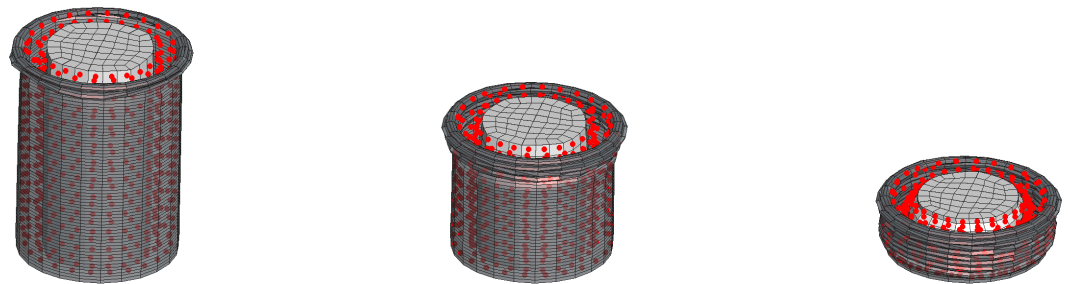


a)

b)

c)

Figure 6.28: SPH model progressive folding of foam-filled tube at a) 30%, b) 50% and c) 80% deformation

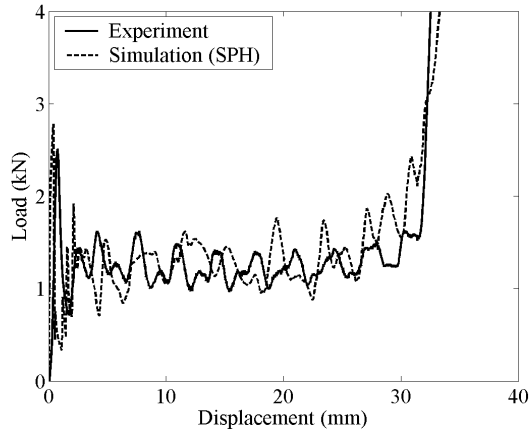


a)

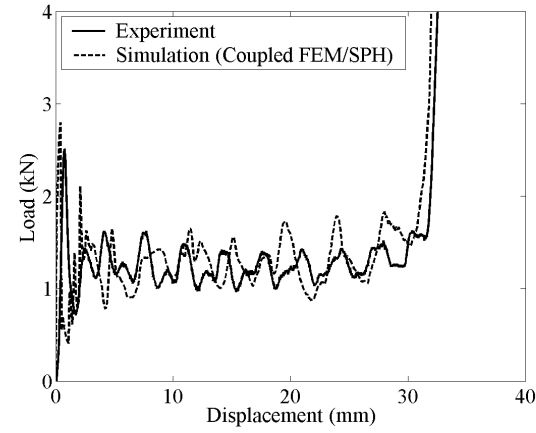
b)

c)

Figure 6.29: Coupled FEM/SPH model progressive folding of foam-filled tube at a) 30%, b) 50% and c) 80% deformation



a)

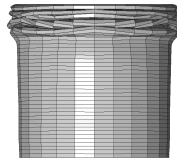


b)

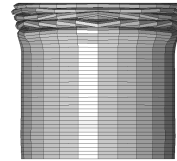
Figure 6.30: Comparison of experimental and numerical load-displacement curves of foam-filled tube: a) SPH, b) direct-coupled FEM/SPH



a)



b)



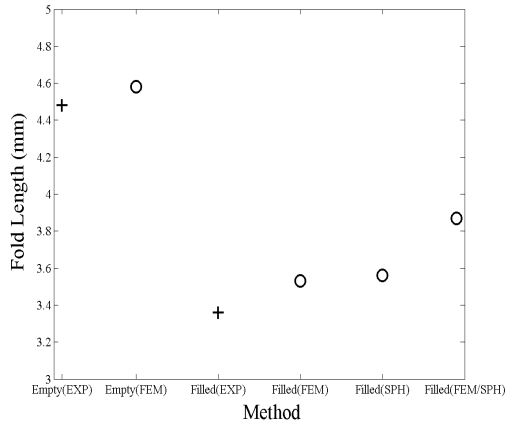
c)

Figure 6.31: Deformed shapes of foam-filled tubes at 50% deformation: a) FEM, b) SPH and c) direct-coupled FEM/SPH

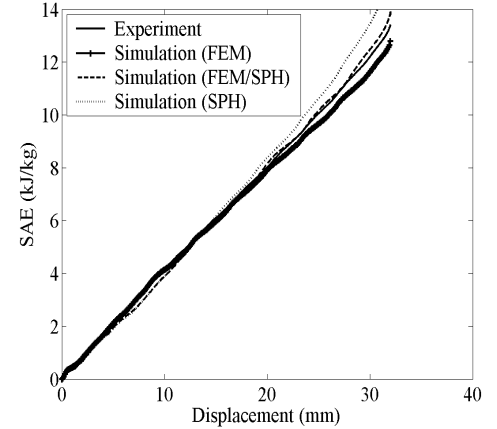
in the analysis, the small element size may cause expensive computational time and error termination.

Figs. 6.28 and 6.29 show SPH and coupled FEM/SPH simulated progressive foam-filled tube deformations at 30%, 50% and 80% deformations, respectively. The models used show a deformation mode change from diamond in the empty tube into concertina in the filled tubes, similar to FEM. The change of deformation mode in SPH Method and coupled FEM/SPH simulations further proved the successful employment of the interactions between shell elements and discrete particles and discrete particles and solid elements.

The resultant load-displacements curves of SPH and coupled FEM/SPH simulations are shown in Figs. 6.30a-b, respectively. In the same figures, the experimental load-displacements curves are also shown for comparison. Both approaches, as also seen in these figures, are found to give satisfactory agreements with the experimental load-displacement curves. It is also noted in Figs. 6.30a-b that the proposed approaches



a)



b)

Figure 6.32: a) Numerical and experimental fold lengths at 50% deformation, b) comparison of experimental and numerical SAE vs. displacement curves of foam-filled tube

result in relatively higher load values than those of FEM around the densification region of the tube deformation. The higher load values are however more pronounced in SPH Method (Fig. 6.30a). Under extensive crushing, since the particles have interactions with the surrounding particles in addition to their initial neighbours, the densification of SPH-modelled foam is steeper than that of FE-modelled foam.

It was previously shown that the restraining effect of foam filling to the tube wall decreased the fold lengths hence increased the number of folds formed in the foam-filled tubes [175]. The FEM, SPH and coupled FEM/SPH deformed shapes of the foam-filled tubes are sequentially shown in Figs. 6.31a-c at 50% deformation. The total number of folds formed, 5, in the models used, as seen in this figure, is the same as that in the experiment. The numerically measured fold lengths are however found slightly higher than the experimentally measured fold lengths (Fig. 6.32). The foam filling causes experimentally 75% reduction in the fold length as compared with empty tube, while the reduction in the fold length increases to 77%, 78% and 84% in FEM, SPH and coupled FEM/SPH simulations, respectively. The experimental and numerical SAE values corresponding to 50% deformation of foam-filled tubes are shown in Fig. 6.32b for comparison.

Numerical simulations based on SPH and coupled FEM/SPH show comparable SAE values with those obtained by FEM and experiments. In filled tubes, the differences in SAE values at 50% deformation between experiment and FEM and SPH and coupled FEM/SPH are 2%, 3.9% and 1.1%, respectively.

In FE modelling of foam filler using explicit numerical solution technique and classical solid elements, the time step depends on the size of the element in the simulation

and the FE model has the longest simulation time primarily due to the severe solid elements deformation. The coupled model reduces the computational time by a factor of 0.75 compared to SPH model and by a factor of 0.30 compared to FE model. The internal force calculation consumes 78% of the total computational time in SPH model while it is reduced to 65% in coupled FEM/SPH technique.

6.5 Discussion - SPH and Direct-Coupled FEM/SPH Method

The quasi-static axial crushing of PS foam-filled Al tubes was simulated using SPH and coupled FEM/SPH and the numerical results were compared with those obtained using FEM and experiments. Both numerical methods were found to give satisfactory agreements with FEM and experiments. The used models successfully simulated the switch in the deformation mode of filled tubes. The comparable load-deformation histories, fold lengths and SAE values between the experiments and numerical analysis, further confirmed that both SPH and coupled FEM/SPH could be applied to model foam-filled tube deformation in cases where classical FEM suffers from severe element distortion and expensive computations.

6.6 Numerical Modelling of Bitubular Foam-filled Aluminum Crash Absorbers - SPH and Direct-Coupled FEM/SPH Method

After obtaining a stable and accurate numerical model based on SPH Method and direct-coupled FEM/SPH Method, the crushing behaviour of several different crash elements composing of empty and foam-filled bitubular tubes were investigated numerically and the results were compared with that of experimental investigations.

Modelling of Al Foam Filler

PAM-CRASH provides material model for the metallic cellular solids capable of undergoing large deformation strain including Al foam and Al honeycomb. In this investigation, the material model of Al foam was simplified by replacing the actual behaviour with an appropriate equivalent honeycomb having the same properties in three directions (thickness, width and length). The mechanical behaviour of metal foams in varying densities was simulated using the following relations [161]:

$$E^* = E_s \left(\frac{\rho^*}{\rho_s} \right)^2 \quad (6.1)$$

$$G^* = 0.375 E_s \left(\frac{\rho^*}{\rho_s} \right)^2 \quad (6.2)$$

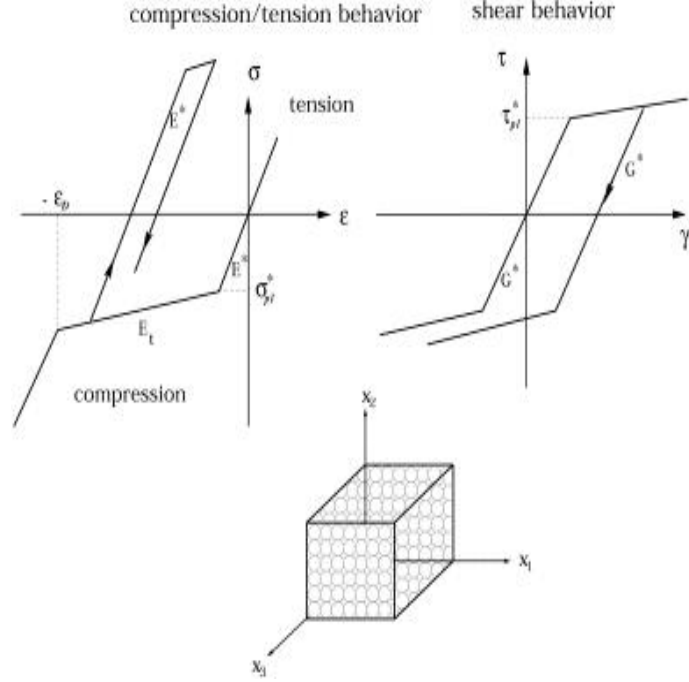


Figure 6.33: Material model for Al foam [161]

$$\sigma_{PL}^* = \sigma_{YS} \left(\frac{\rho^*}{\rho_s} \right)^{\frac{3}{2}} \quad (6.3)$$

$$\tau_{PL}^* = 0.5\sigma_{YS} \left(\frac{\rho^*}{\rho_s} \right)^{\frac{3}{2}} \quad (6.4)$$

$$\epsilon_D = 1 - 1.4 \frac{\rho^*}{\rho_s} \quad (6.5)$$

where, E , G , σ_Y , τ and ρ are the Young's and shear modulus, yield and shear stress and density, respectively. The subscript PL, s and * refer to plateau, foam material and foam, respectively and stands for densification strain at which the metal foam begins to densification. Fig. 6.33 shows the material parameters listed above with corresponding stress-strain curves under compression, tension and shear for the simplified model.

Simulation Results

Empty tubes both 25 and 35mm in diameter deformed in progressive diamond mode forming eight-corner folding geometry. Fig. 6.34 shows the numerically obtained deformation patterns of 25mm-diameter tube at 0%, 40% and 80% strains. It has been experimentally found and numerically confirmed that 4-5 folds formed in both empty tubes. Typical numerical and experimental load-displacement curves of the tubes are

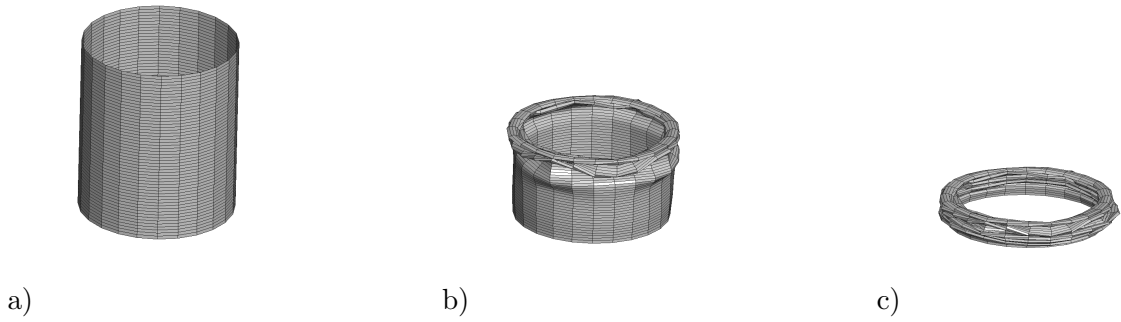


Figure 6.34: Images of crushed 25mm-diameter Al tube at a) 0%, b) 40% and c) 80% strains

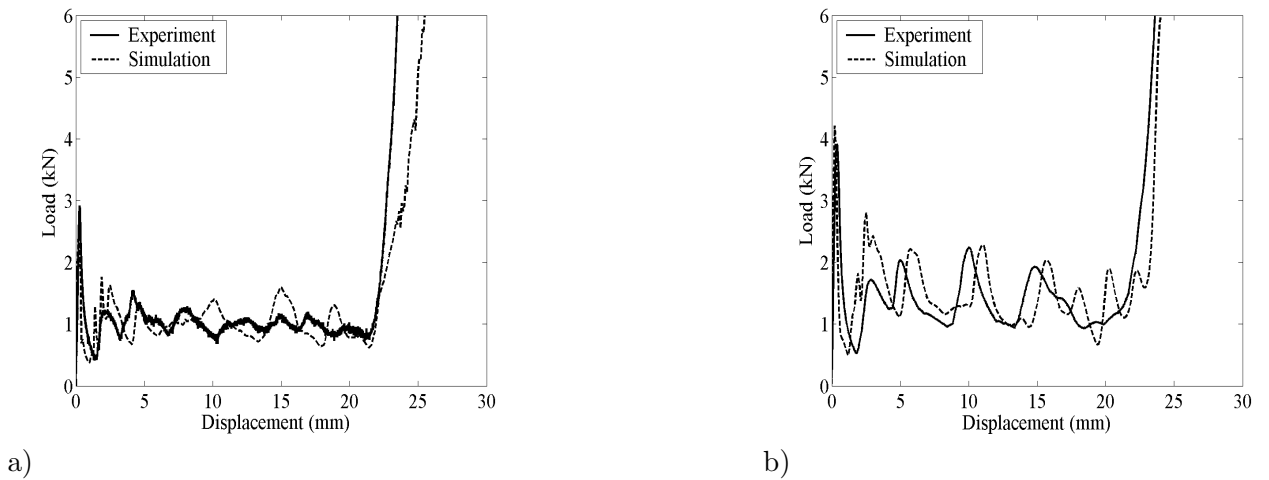


Figure 6.35: a) Numerical and experimental load-displacement curve of a) 25mm- and b) 35mm-diameter empty tubes

shown in Figs. 6.35a-b for 25 and 35mm-diameter tubes, respectively. Despite to the differences between the displacements corresponding the to the peak loads, numerical and experimental load values are relatively comparable and show well agreements with each other. It is also noted in Figs. 6.35a-b that numerical and experimental initial peak load values are greater than those of following peak loads. This is a phenomenon commonly observed in thin-wall tube crushing, which simply arises from the constraining effect imposed by the compression test platens.

Foam-filled single tubes

The effect of Al foam filling of 25mm-diameter empty Al tube is to shift the deformation mode from diamond to progressive axisymmetric (concertina) mode of deformation, regardless the Al-foam density (270, 350 and 430kg/m³) used for filling. The number of folds formed also increased with Al foam filling from 4 in empty tube to 6 in filled tube and hence the fold length decreased accordingly. Figs. 6.36- 6.37 show experi-

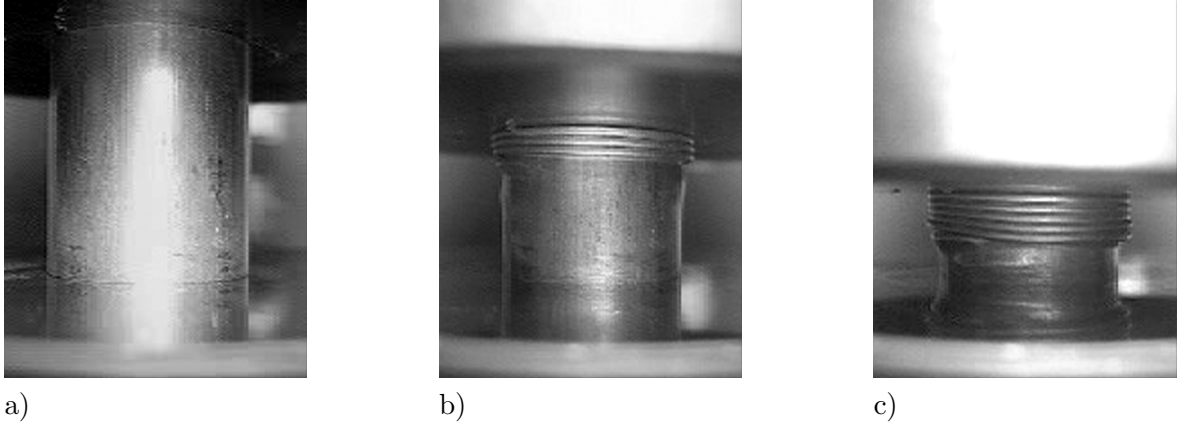


Figure 6.36: Images of crushed 25mm-diameter Al foam-filled (270kg/m^3) tube at a) 0%, b) 40% and c) 70% strains

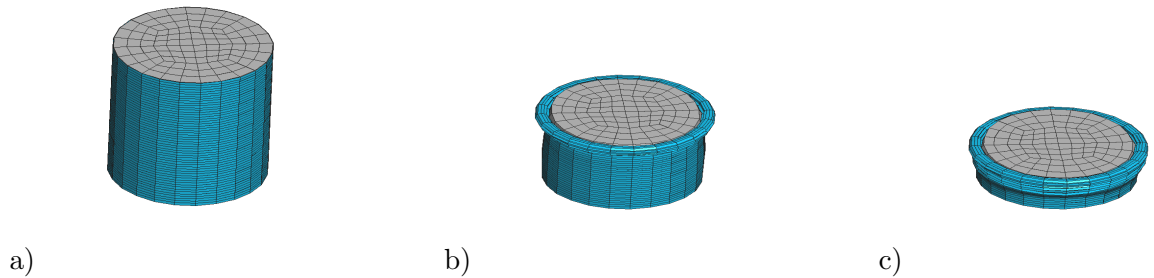


Figure 6.37: Numerical images of crushed 25mm-diameter Al foam-filled (270kg/m^3) tube at a) 0%, b) 40% and c) 70% deformation

mental and numerical concertina mode of deformation of 25mm-diameter tube filled with 270kg/m^3 Al foam at 0%, 40% and 70% strains, respectively. The numerical and experimental load-displacement curves for Al foam-filled tubes at three different foam densities are shown in Figs. 6.38a-c. Numerical deformation patterns and load values of filled tubes show relatively well agreements with those of experiments as shown in Figs. 6.36- 6.38.

Foam-filled bitubular tubes

In investigated bitubular configurations, BPH, BPP and BPA, the outer 35mm-diameter tube deformed in diamond mode (Figs. 6.39a-c) similar to empty tubes. The inner 25mm-diameter tube deformed in diamond mode in BPH and concertina mode in BPP and BPA configurations, showing again the thickening effect of the foam filling. It is also noted that the PS foam filler experiences low values of compression stresses than Al foam at the same strain level. For this reason the PS foam filler shows comparably larger deformations particularly near to the folded tube wall (A in Fig. 6.40) than Al foam filler (B in Fig. 6.40). Therefore the discrete particles were used to model the

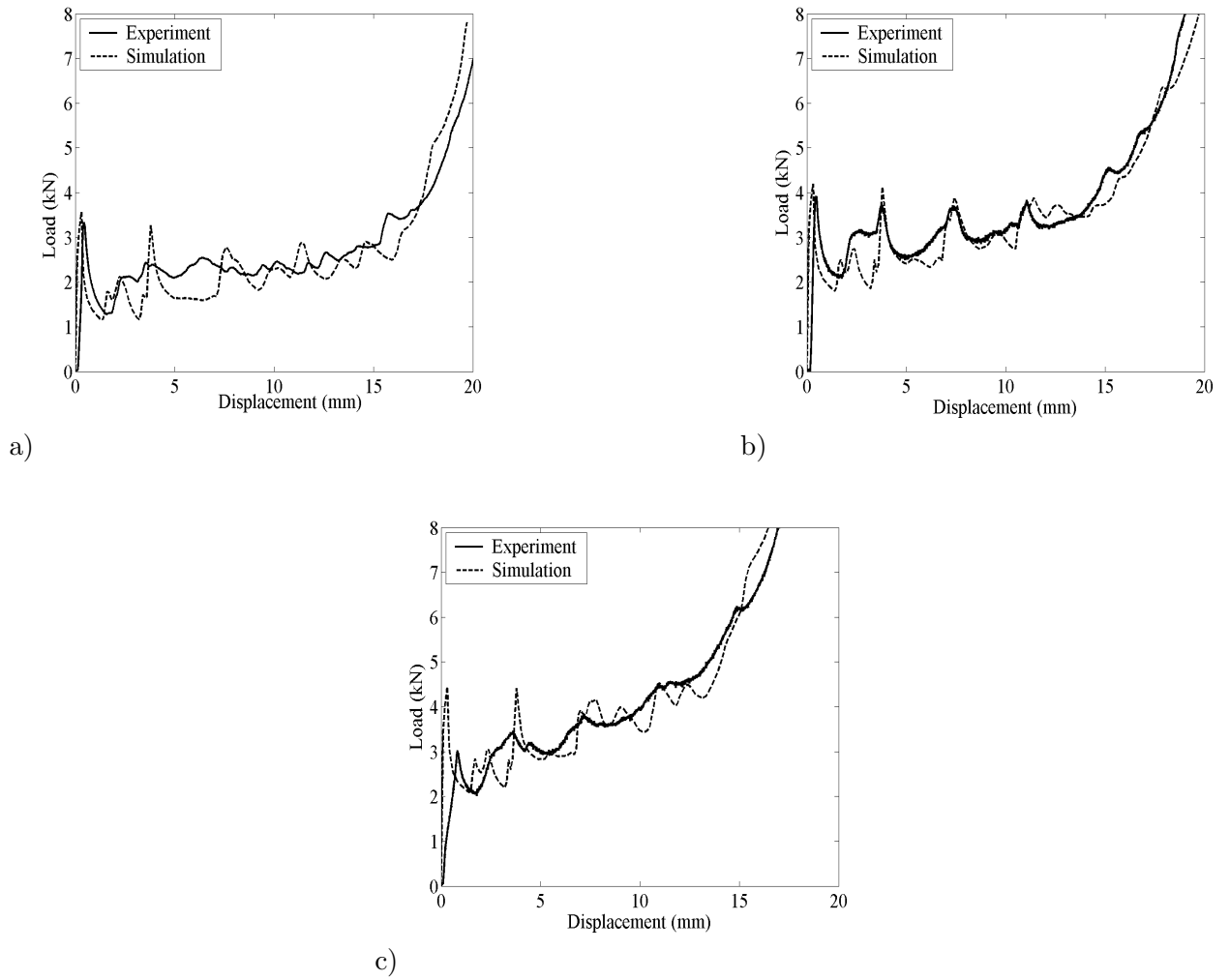


Figure 6.38: Numerical and experimental load-displacement curves of a) 270kg/m^3 , b) 350kg/m^3 and c) 430kg/m^3 Al foam-filled 25mm tubes

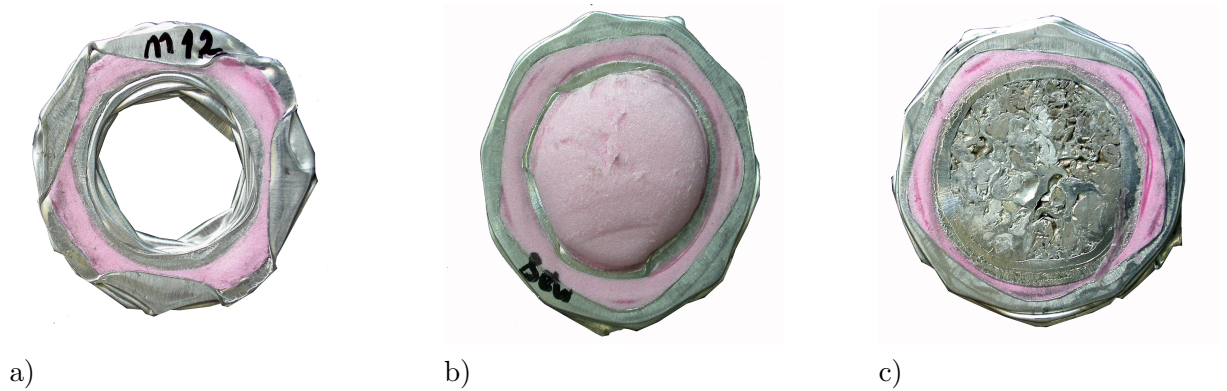


Figure 6.39: Top view of deformed: a) BPH, b) BPP and c) BPA bitubular configurations. In a) both tubes deformed on diamond mode, while interior tube deformed in concertina mode in b) and c)

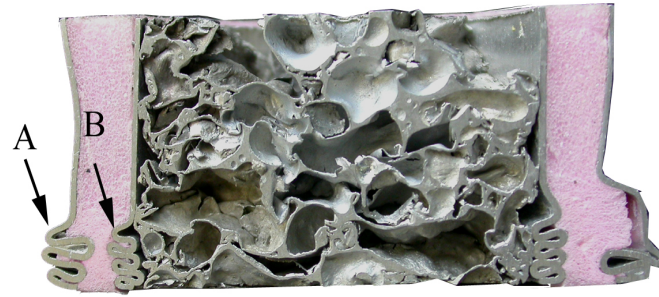


Figure 6.40: Side view of crushed BPA specimen

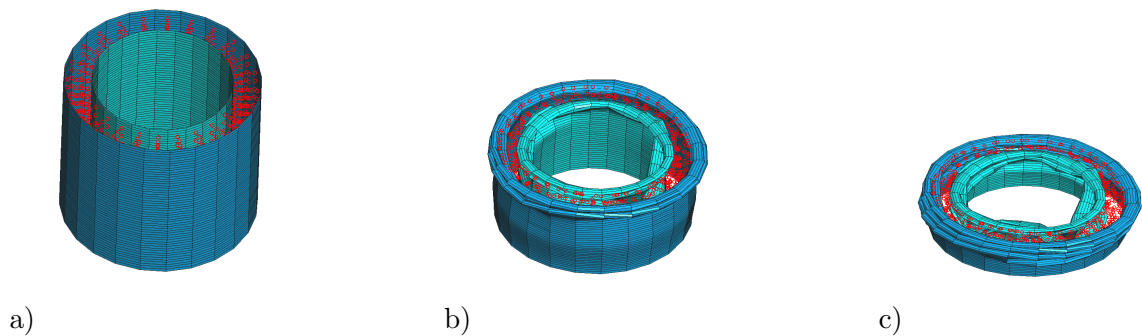


Figure 6.41: Numerical images of crushed BPH design at a) 0%, b) 40% and c) 65% deformation

extensive deformation zones of PS foam filler in bitubular configurations.

Figs. 6.41- 6.43 show the numerical deformation patterns of the BPH, BPP and BPA configurations, respectively. The experimental deformation patterns are seen in these figures reproducible with the proposed numerical coupled model. The experimental and numerical number of folds also shows well coincidence. The experimental number of folds is the same for the three configurations, 4, while the numerical fold numbers are 5, 4 and 4 for BPH, BPP and BPA, respectively. The comparison between numerical and experimental load-displacement curves of BPH, BPP and BPA configurations are shown sequentially in Figs. 6.44a-c. Although the first load-peak values of the numerical load-displacement curves are higher than those of experimental values, the following load values are very similar. It is assumed that the foam fillers have the same strength values in three orthogonal directions in the modelling, but the anisotropy in strength values of the filler exists due to the variations in the cell size and cell wall thicknesses. This inevitably results in discrepancies between the numerical model and experimental results.

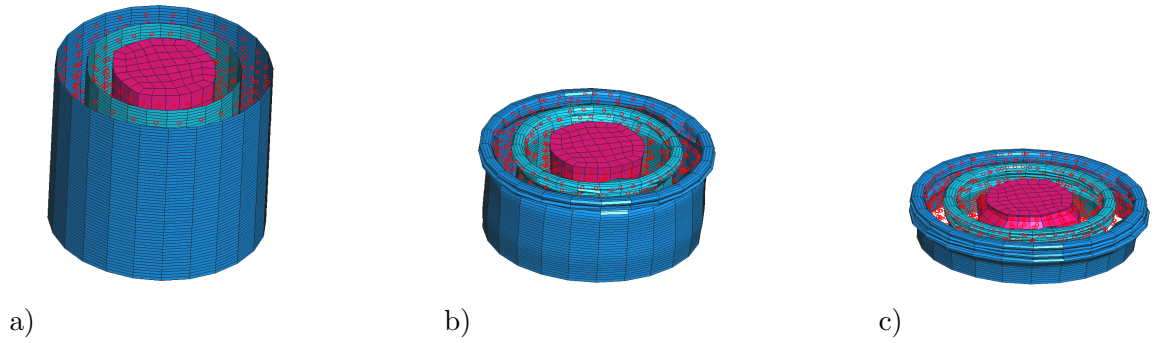


Figure 6.42: Numerical images of crushed BPP design at a) 0%, b) 40% and c) 65% deformation

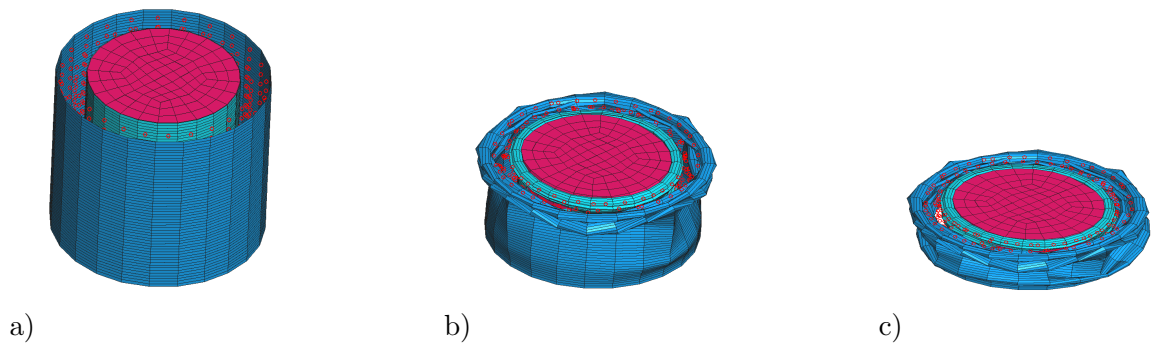


Figure 6.43: Numerical images of crushed BPA design at a) 0%, b) 40% and c) 65% deformation

Comparison of SAE values

The experimental and numerical SAE values of the investigated empty and foam-filled single and bitubular tubes corresponding to 50% deformation are tabulated in Table 6.1. The maximum difference between the experimental and numerical SAE values in Table 6.1 is about 10%. The experimental SAE values listed in this table show that single empty tube absorb more energy than foam-filled single and bitubular tubes.

Design	Experimental SAE kJ/kg	Numerical SAE kJ/kg
Empty	8.21	7.83
Filled single tube (270kg/m ³)	5.57	5.11
Filled single tube (350kg/m ³)	6.69	6.14
Filled single tube (430kg/m ³)	6.16	6.24
BPH	7.38	7.09
BPP	7.35	6.95
BPA	5.82	5.12

Table 6.1: Experimental and numerical SAE values of empty and foam-filled tubes at 50% strain

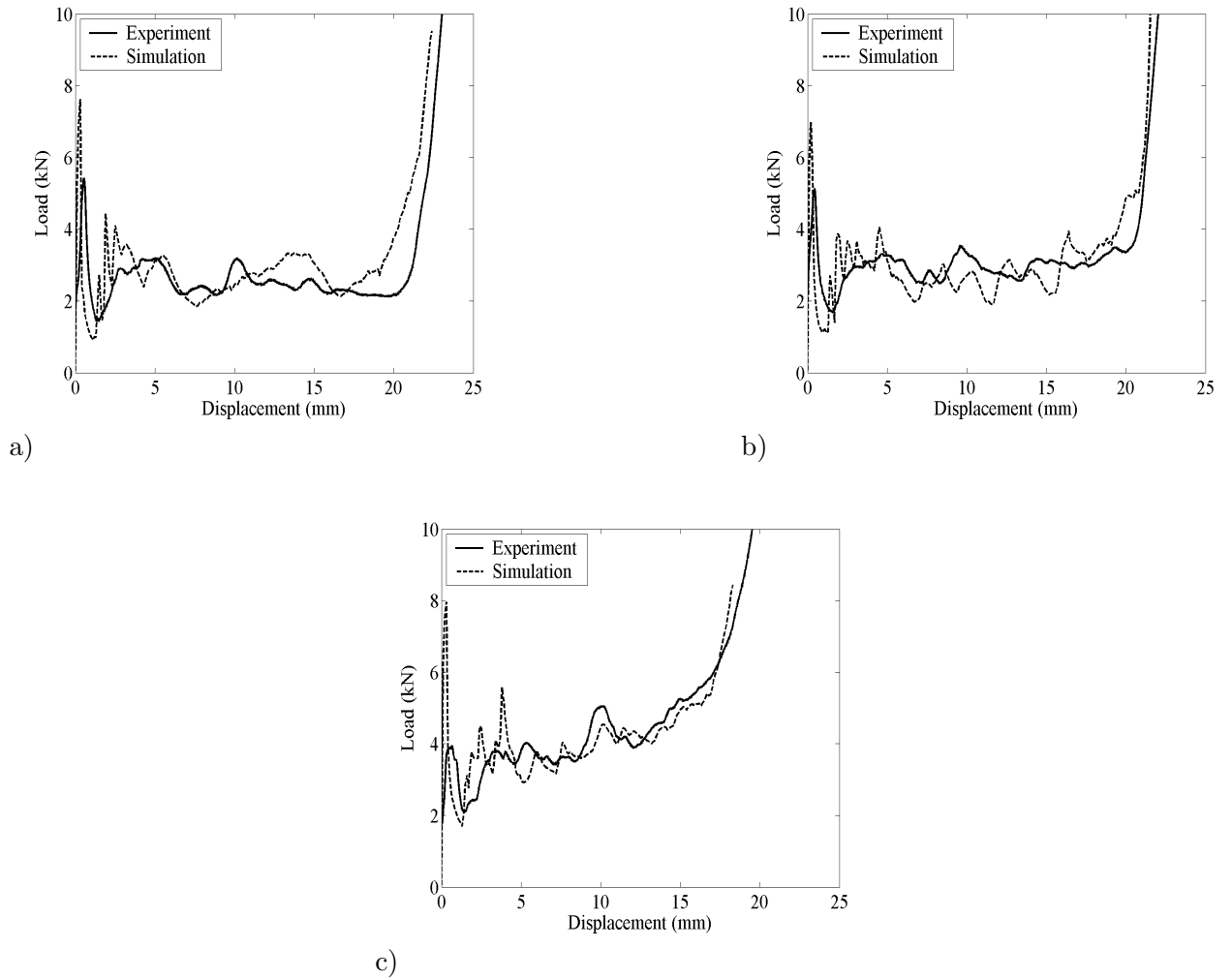


Figure 6.44: Numerical and experimental load-displacement curves of a) BPH, b) BPP and c) BPA designs

Design	Experimental SAE kJ/kg	Numerical SAE kJ/kg
Empty	12.7	12.39
Filled single tube (270kg/cm ³)	13.17	13.31
Filled single tube (350kg/cm ³)	16.78	14.89
Filled single tube (430kg/cm ³)	18.86	19.16
BPH	11.36	11.97
BPP	12.28	12.75
BPA	13.43	12.93

Table 6.2: Experimental and numerical SAE values of empty and foam-filled tubes at 80% strain

The SAE values of Al foam-filled single and bitubular tubes are found to be lower than that of empty tube until large strains are reached. As the crash absorbers undergo large deformations, the foam filling of single, bitubular and multi-tubes designs become energetically more efficient compared with single empty tube. As is tabulated in Table 6.2 the experimental and numerical SAE values of Al foam-filled single tubes and BPA bitubular designs exceed the single empty tube SAE value at 80% strain. The increase of SAE values of filled tubes over that of empty tube is mainly to the increase of the foam density with increasing deformation strain. It was previously shown that there is a critical foam density above which the foam filling became more efficient [22]. The critical foam filler density therefore reached during the deformation of the foam-filled tubes.

6.7 Discussion - SPH and Direct-Coupled FEM/SPH Method

In this section the quasi-static crushing behaviour of Al foam-filled single, bitubular configurations were compared through compression testing and numerical analysis. Tubes and foam fillers were modelled using FEM and direct-coupled FEM/SPH. In all tested and modelled configurations Al foam filling changed the deformation mode from diamond into concertina. Single empty Al tube showed higher SAE values than Al foam-filled single tubes, Al and PS foam-filled bitubular configurations.

In terms of numerical simulation, the results of proposed numerical models for BPH, BPP and BPA configurations have shown well accordance with the experimental results.

6.8 Discussion - Numerical Modelling of Aluminum Crash Absorbers

The quasi-static axial crushing of PS foam-filled single and bitubular Al configurations were simulated using SPH and coupled FEM/SPH and the numerical results were compared with those obtained using FEM and experiments. Both numerical methods were found to give satisfactory agreements with FEM and experiments. The used models successfully simulated the switch in the deformation mode of filled tubes. The comparable load-deformation histories, fold lengths and SAE values between the experiments and numerical analysis, further confirmed that both SPH and coupled FEM/SPH could be applied to model foam-filled tube deformation in cases where classical FEM suffers from severe element distortion and expensive computations.

6.9 Composite Crush Absorbers

Composite crush absorbing elements made of glass- or carbon-fibre-reinforced tubes exhibit high SAE in axial crush. A challenge for the engineer is to utilise these properties

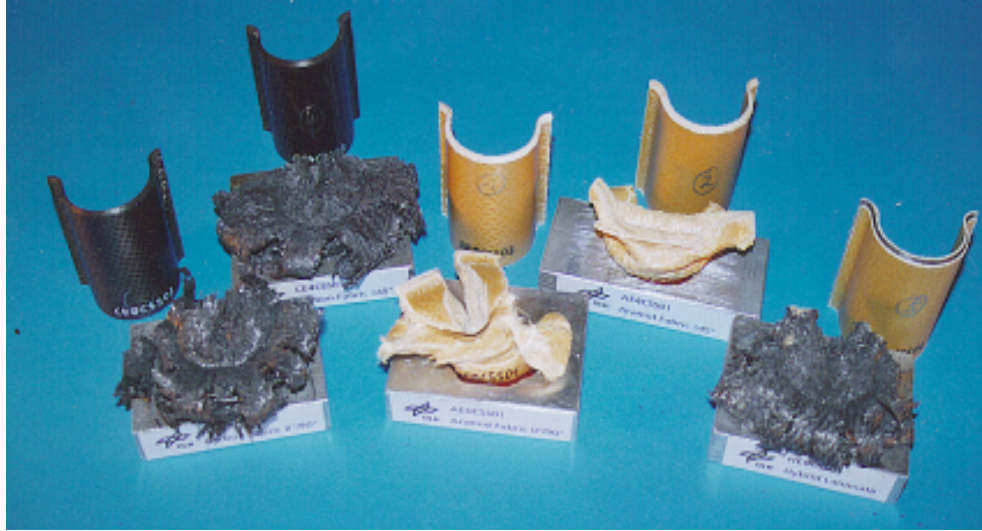


Figure 6.45: Crushing behaviour of different tube segment specimens [176]

in structural applications. Therefore it is very important to understand the EA and failure mechanisms, to have tools for assessing the crashworthiness of such structures and to consider the design of specific energy absorbing substructures.

After having a fundamental understanding of the modelling of crash behaviour using particle-based modelling techniques, the previously conducted work extended to model the crushing behaviour of CFRP energy absorber components.

6.10 Experimental Investigations on Carbon-Fibre-Reinforced Composite Tube Segments

The European Union funded project CRASURV (Design for Crash Survivability) aimed at increasing the knowledge of the crash behaviour of lightweight composite structures and their application in aircraft fuselage structures. DLR was responsible for manufacturing and test of different components and sub-components made of carbon fabric, aramid fabric and a hybrid laminate made of carbon and aramid fabrics (Fig. 6.45). The experimental results which presented here are from the tests conducted in the frame of CRASURV Project. Within this test programme the behaviour of two basic materials, a carbon and an aramid fabric with the epoxy resin system M10 (Ciba-Geigy) have been selected. In addition to the tests on carbon and aramid materials, a series of test on a hybrid layup of the two basic materials were conducted. The selected layup is the same as that in the energy absorbing webs of the generic box structures which are build and tested by DLR in other tasks of the project. The materials used in these investigations are: The flat specimens for the tension, coupon compression and

Material	Industrial Name	Thickness
Carbon Fabric	VICOTEX G803/M10	$t_{nom}=0.3\text{mm}$
Aramid Fabric	STRAFIL AT2856/M10	$t_{nom}=0.22\text{mm}$
Hybrid Laminate	VICOTEX G803/M10	$t_{nom}=2.10\text{mm}$
	STRAFIL AT2856/M10	

Table 6.3: Materials used for the segment specimens

bending tests have been cut from laminated plates, which have been fabricated in the autoclave between two polished steel plates. In case of the carbon materials 7 layers of the VICOTEX G803/M10 material have been used, the aramid plates consists of 9 layers of STRAFIL AT285/M10. A total three plates with the dimensions 300x300mm have been fabricated with the basic materials, two of them in $0^\circ/90^\circ$ direction and one plate in the $\pm 45^\circ$ direction. One plate of the same dimensions has been produced with the hybrid layup, Table 6.3.

The tube segment specimens ($0^\circ/90^\circ$ and $\pm 45^\circ$) have been manufactured in closed steel moulds using the same number of layers and layup as described above for the plates. In one shot a segment of about 200mm length could be fabricated, which was cut into three individual specimens of about 67mm length, Fig. 6.46. In a following mechanical process a bevel trigger of 45° has been machined to the top edge of the specimen. The specimens for the upcoming dynamic crushing tests have been manufactured together with those tested quasi-statically. From each 200mm large performs one specimen has been selected for the quasi-static tests, a second one will be tested dynamically with $v_0=5\text{m/s}$ and the last one with $v_0=10\text{m/s}$.

During the dynamic tests in DLR's drop tower the displacement of the drop mass which corresponds directly to the stroke of the specimen and the load close to the impacting flat plate have been recorded with a sampling frequency of 200 kHz. To get the load information close to the crush front a piezoelectric load cell has been fixed between the impacting flat steel plate and the additional masses in the drop mass assembly. In addition, the exact velocity of the drop mass was measured just before the impact using a light barrier. The tube segment specimen is embedded in an Al base plate and fixed on the load platform of the drop tower with adhesive. This prevents tilting and global movements and buckling caused by the axial loading. Since triggering able a progressive crushing a bevel trigger of 45° at the outside of the tube segment has been used for a progressive crushing behaviour.

In the frame of the project several tests such as tensile, shear, coupon compression, segment compression (dynamic-crushing), short beam and flexural test have been conducted. Since this thesis aims at improving the existing simulation techniques for the

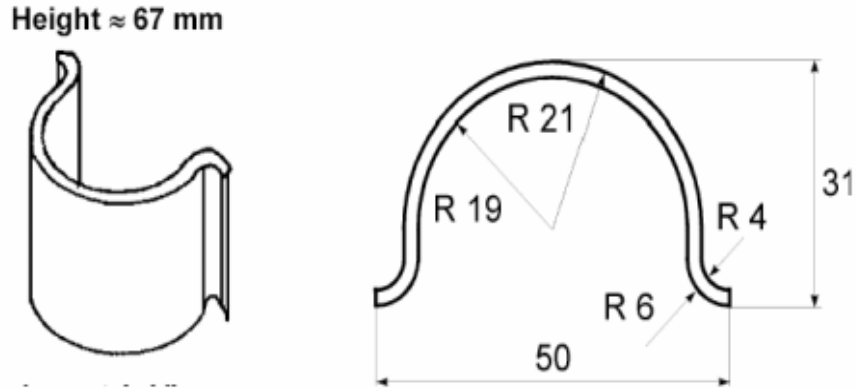


Figure 6.46: Sketch of the DLR-tube segment specimen [176]

modelling of impact and dynamic crush behaviour of the composite structures in this chapter the experimental procedure for obtaining the material parameters of the composite material models is not reported. The experimental dynamic crush of composite tube segments was discussed in detail. The numerically obtained results were compared with dynamic crush tests. Further information concerning the identification of the material parameters can be found in [176].

Dynamic Crush Tests of Composite Tube Segments

A Carbon-Fibre-Reinforced Segment $0^\circ/90^\circ$ ($v_0=5\text{m/s}$)

Fig. 6.47 shows the specimen after the dynamic crushing test. The carbon-fibre-reinforced segment fragmented into small carbon debris and these debris are continuously compressed during the tests or fell apart from the specimen. Fig. 6.48 shows the crushing force-deformation history of the carbon-fibre-reinforced composite tube segments. Three tested specimens show the same crushing characteristics: After a first peak (between 20-25kN), the crushing force oscillates in between 12 and 17kN and exhibit a constant crushing load until the bottoming out. The nearly constant crushing load shows that the carbon-fibre-reinforced segments can be used as effective crash absorbers since they absorb crash energy in a progressive manner.

B Carbon-Fibre-Reinforced Segment $0^\circ/90^\circ$ ($v_0=10\text{m/s}$)

The previously highlighted crushing behaviour was also obtained by the dynamic crush test with $v_0=5\text{m/s}$. The deformation patterns depicted in Fig. 6.49. Fig. 6.50 shows the crushing load-deformation history of the composite segments. The crushing load-

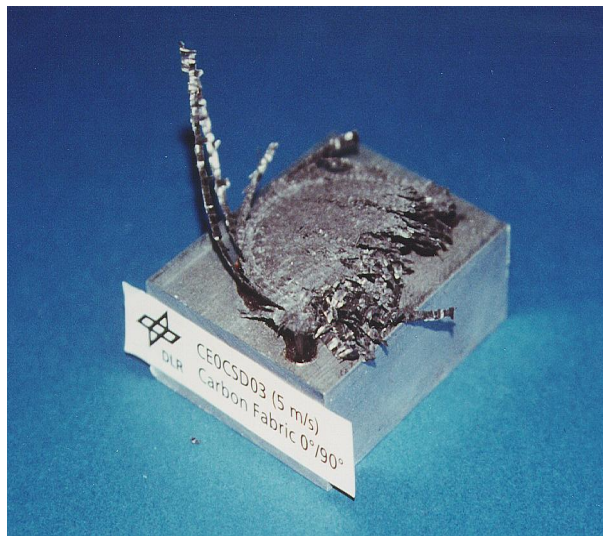


Figure 6.47: Carbon-fibre-reinforced segment $0^\circ/90^\circ$ specimen after dynamic crushing test with $v_0=5\text{m/s}$ [176]

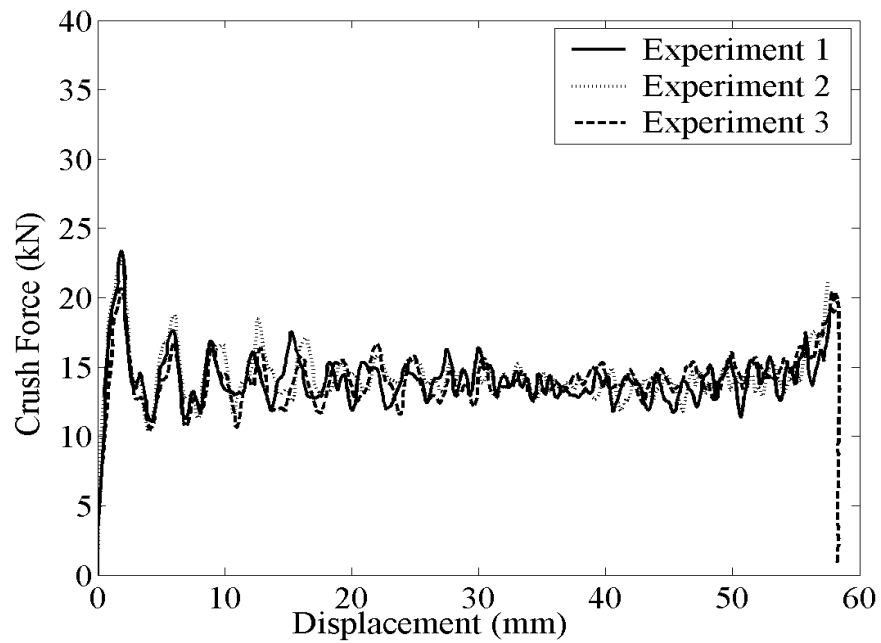


Figure 6.48: Results of dynamic crushing tests - $0^\circ/90^\circ$ ($v_0=5\text{m/s}$)

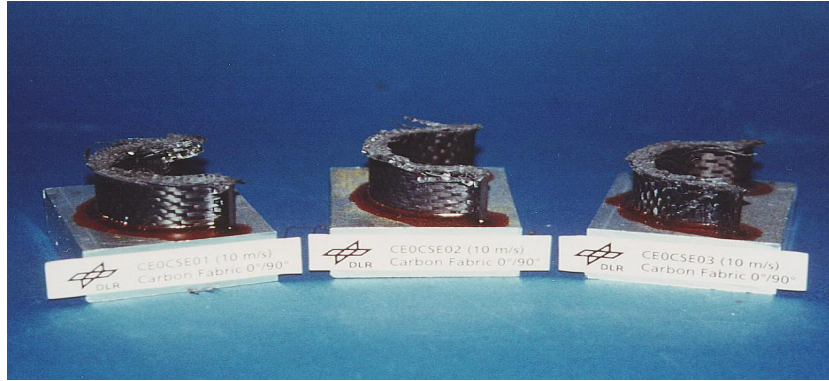


Figure 6.49: Carbon-fibre-reinforced $0^\circ/90^\circ$ specimens after dynamic crushing test with $v_0=10\text{m/s}$ [176]

deformation history is comparable with the dynamic crush test with $v_0=10\text{m/s}$. However the peak force and the plateau load levels are lower.

C Carbon-Fibre-Reinforced Segment $\pm 45^\circ$ ($v_0 = 5\text{m/s}$)

In Fig. 6.51 the tested specimen is shown after the test. The deformation is comparable with the tests conducted with the specimens with $0^\circ/90^\circ$ orientation. The specimen fragmented into small debris and structural integrity has been lost. Fig. 6.52 shows the crushing force-deformation history during the crushing process. Here one can observe that the crushing load, after the first peak, slightly increases. Although the orientation changed, the carbon-fibre-reinforced composite segments exhibits optimal EA behaviour.

D Carbon-Fibre-Reinforced Segment $\pm 45^\circ$ ($v_0 = 10\text{m/s}$)

Finally the carbon-fibre-reinforced specimens with $\pm 45^\circ$ orientation were tested under a loading speed of $v_0=10\text{m/s}$. Fig. 6.53 show the similarity of the deformation patterns between the specimens with an orientation of $0^\circ/90^\circ$ and $\pm 45^\circ$. However the crushing load-deformation history differs from the previously conducted tests. Fig. 6.54 shows that the differences between the first peak loads and the progressive crushing load levels differ measurably.

Experimental investigations showed that the carbon-fibre-reinforced segments can be used as effective crash energy absorber. The crushing force-deformation histories during the crush process exhibit similar characteristics with different load levels. In all the tests after a high peak level a constant crushing load level was obtained. This indication also shows the importance of the introduction of the bevel trigger. The crushing

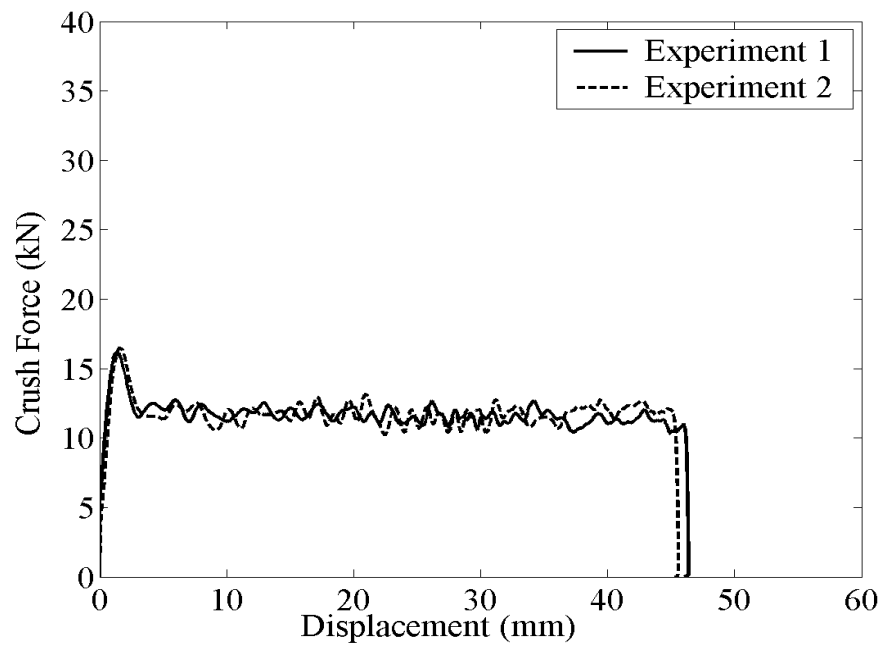


Figure 6.50: Results of dynamic crushing tests - $0^\circ/90^\circ$ ($v_0=10\text{m/s}$)



Figure 6.51: Carbon-fibre-reinforced $\pm 45^\circ$ specimen after dynamic crushing test with $v_0=5\text{m/s}$ [176]

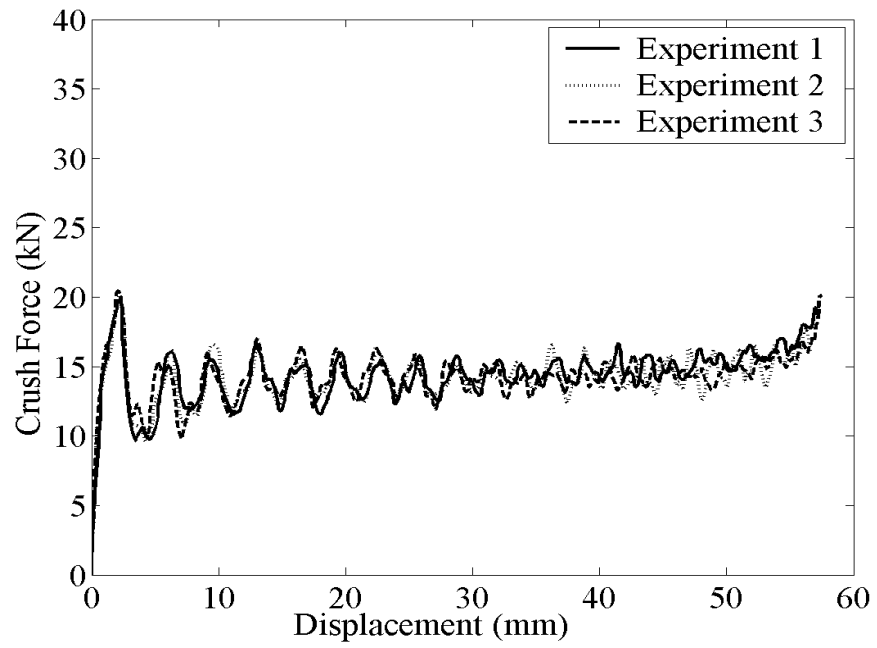


Figure 6.52: Results of dynamic crushing tests - $\pm 45^\circ$ ($v_0=5\text{m/s}$)

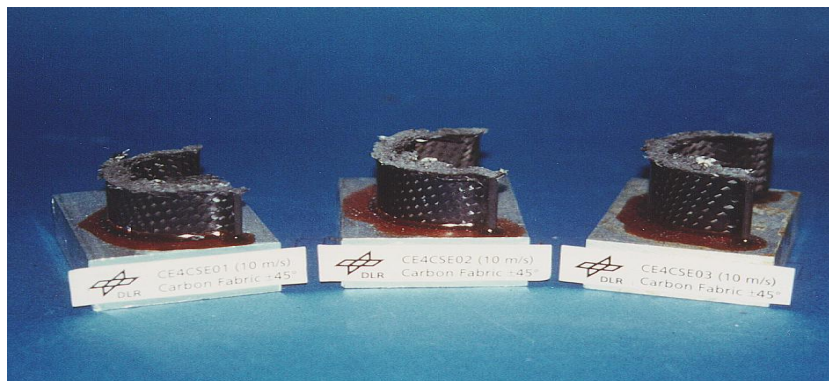


Figure 6.53: Carbon-fibre-reinforced $\pm 45^\circ$ specimen after dynamic crushing test with $v_0=10\text{m/s}$ [176]

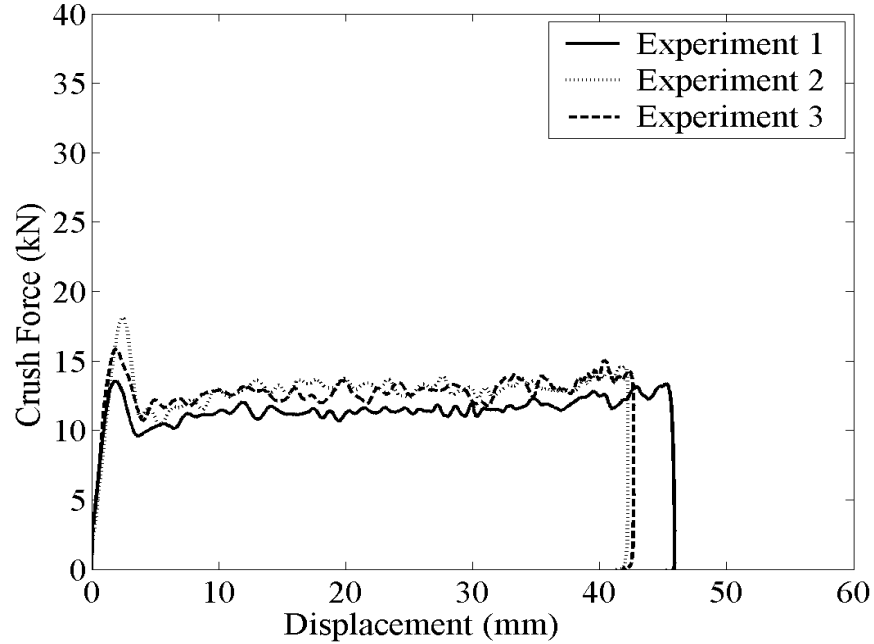


Figure 6.54: Results of dynamic crushing tests - $\pm 45^\circ$ ($v_0=10\text{m/s}$)

load level is highly dependent on the crushing speed. Here the contribution, mainly duration, of the friction mechanics between the specimen and the loader plays a key role.

6.11 Numerical Modelling of the Carbon-Fibre-Reinforced Segments

In this section a numerical model for the segment compression (dynamic-crushing) was generated and the crushing behaviour of the segment specimens made of carbon-fibre-reinforced composite was investigated. Although in the experimental part of the project three different kinds segments made of carbon fabric, aramid fabric and hybrid fabric were investigated, here just the results, as in the experimental part, of the segments made of carbon fabric segment with an orientation of $0^\circ/90^\circ$ were reported. The material parameters used in the numerical simulations are obtained from the experimentally conducted tests.

The carbon-fibre-reinforced segment specimen consists of 7 layers. As mentioned before for the modelling of the shell layers there are two different common methods used for crash and impact simulations: Layered shell model in which the delamination interface is ignored and stacked shell model in which the interaction between the adjacent layers and the delamination interface between these layers are calculated. For the modelling of the crush behaviour of segment specimens a combination of these approaches has

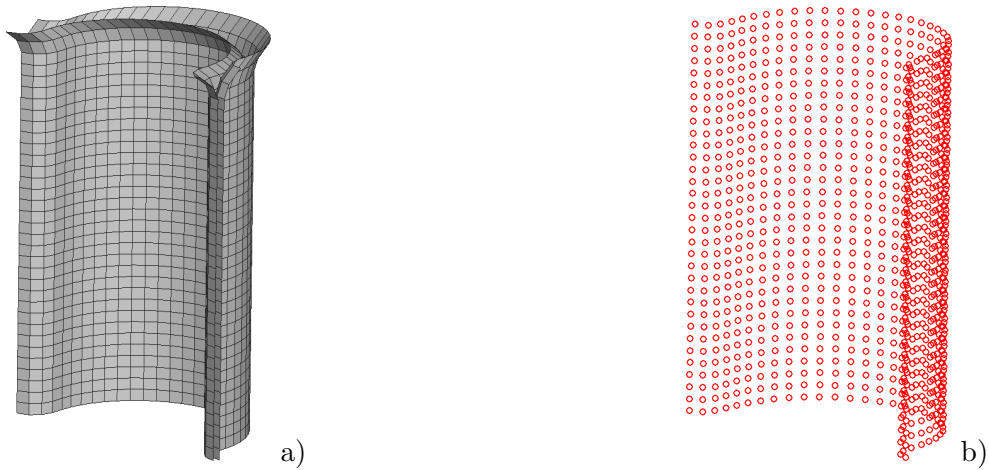


Figure 6.55: a) Modelling of segment walls, b) modelling of resin

been used. The above mentioned 7 layers divided into two groups: Group1: 3 layers and Group2: 4 layers. Group 1 and 2 represented with one layer using layered shell model, Fig. 6.55. Experimental crushing analysis showed that after the initiation of delamination, the tube walls split and progressive fragmentation takes place. The resin crushed under compression loads. After the split of the tube walls which initiates a high peak load, the resin fragments into small debris. This response can be defined as elastic-plastic material behaviour with an initial peak crush load. Therefore the interface resin is modelled with particles using elastic-plastic material model, (Fig. 6.55). The particles are compacted under compression stresses, allowing stable computations, avoiding further element elimination and lost of contact force information dependent on the EET. Since the study presented here aims to highlight the capability of particle modelling a simplified model was considered. For each single tube wall element a corresponding discrete particle for resin was discretised. Between these layers a delamination interface and a tied contact (with represents the debonding at the resin interface) defined, Fig. 6.56. The delamination parameters used here were obtained by previously conducted tests at DLR.

In the experimental investigations a bevel type trigger has been used for the progressive crushing. Therefore a trigger has been also introduced to the numerical model. During the crush event inner and outer walls of the triggered components bend and this create a larger crush front for further progressive crushing. However in numerical models the realistic modelling of the shell bending behaviour made of composites are hard, since most of the failure mechanisms are based on the EET. Element elimination shear strain value of 10% was used for the damage initiation of the segment walls. Here, in the numerical model the crushing front and the delamination path were introduced by offsetting the elements at the upper end of the shell layers.

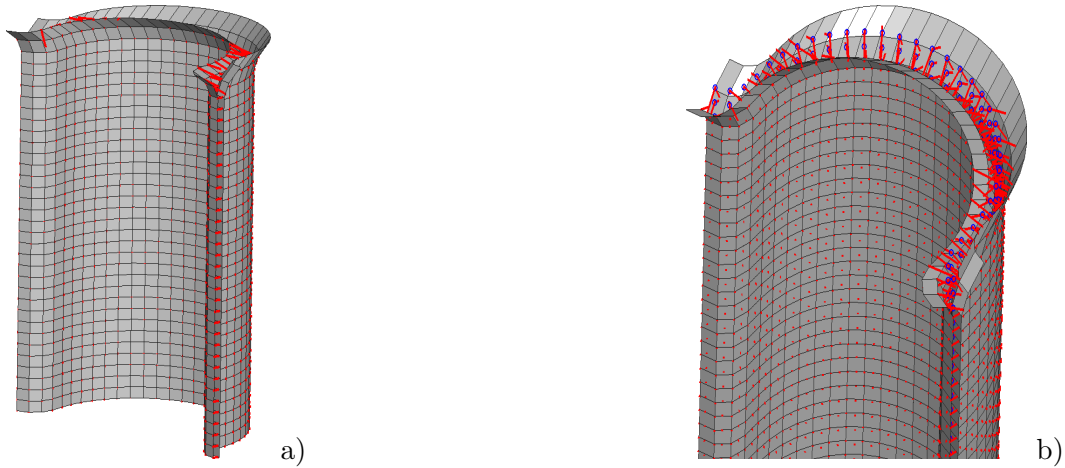


Figure 6.56: a) Representation of the delamination interface, b) representation of the debonding interface

The dynamic test on segment specimens were performed using a drop mass. In numerical investigations the kinetic energy of the drop mass converted into a constant crushing velocity ($v_0=5\text{m/s}$ and $v_0=10\text{m/s}$). Figs. 6.57 and 6.58 show the deformation stages of crushing segment at 0%, 20%, 40%, 60% and 80% for $v_0=5\text{m/s}$ and $v_0=10\text{m/s}$, respectively.

As one can see, the introduced crash front works well and a global progressive crushing behaviour was obtained. For the numerical simulations with $v_0=5\text{m/s}$, tube walls were eliminated earlier than the simulation with $v_0=10\text{m/s}$. This causes loss of strength in the direction of crush propagation. However in both cases, the fragmentation behaviour of the resin was modelled successfully. The fragments are mainly placed in the center of the specimen and some fell apart. The contact surface between the loaders and the specimen was kept through the simulation. However, the damage of the tube walls is still dependent on the size of the mesh. This phenomena was studied by Holzapfel et al. [177] and similar findings were obtained. In the numerical simulations presented here a mesh size of 2mm was used. Although promising results were obtained further investigations concerning the effect of element size and also the number of particles on crushing response must be studied.

Figs. 6.59 and 6.60 show the corresponding crush force-displacement history of the abovementioned numerical simulations. Both simulations reproduce the progressive crushing characteristics observed in the experimental investigations. The results of the proposed numerical model are promising. However a stable load path was not obtained. This can rely on the lack of contact between the loaders and the segment specimen. Since the contact information, result of lack of contact, between two timesteps can not

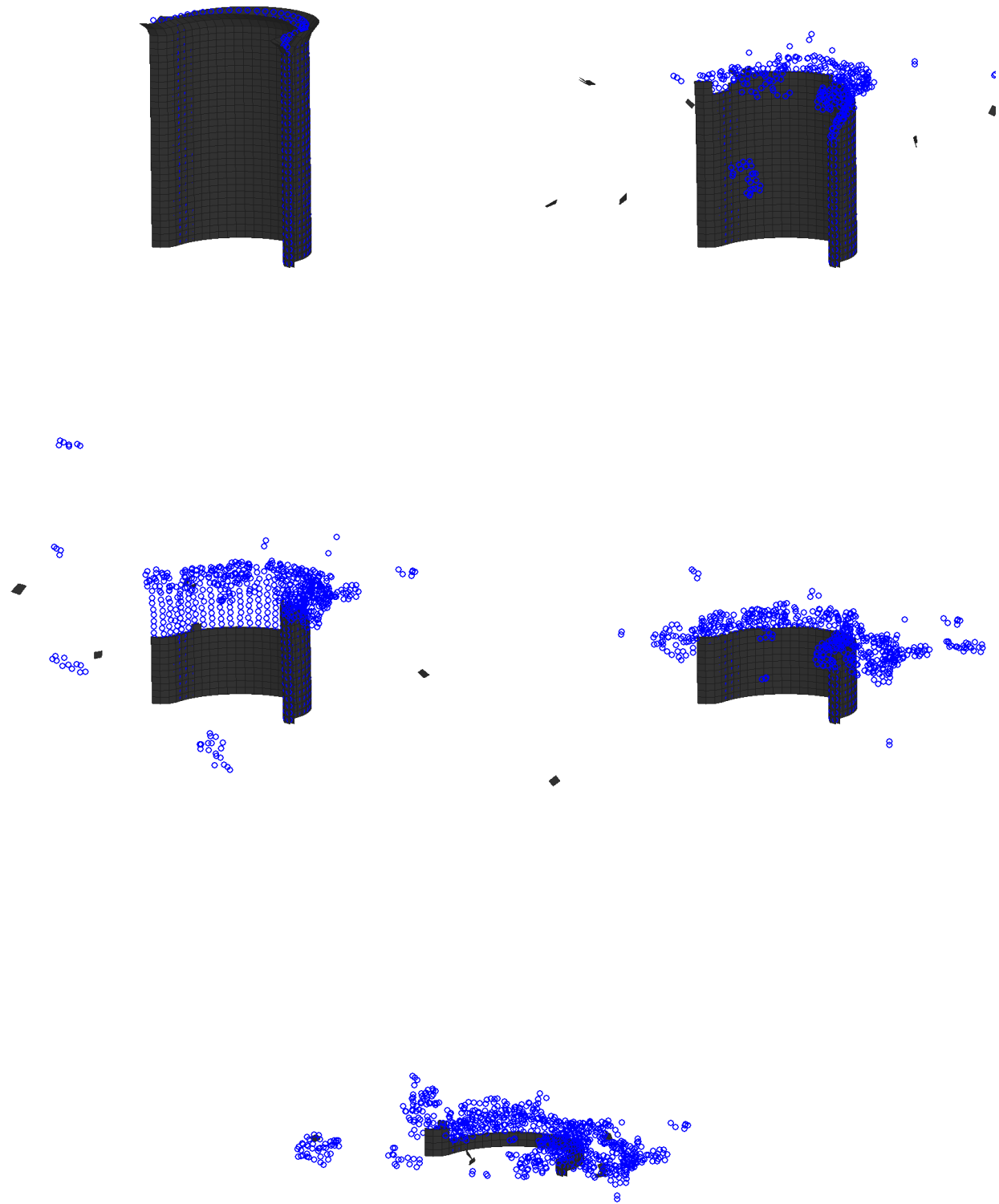


Figure 6.57: Numerical images of crushed carbon-fibre-reinforced composite segment ($v_0=5\text{m/s}$) at a) 0%, b) 20%, c) 40%, d) 60% and e) 80% deformation

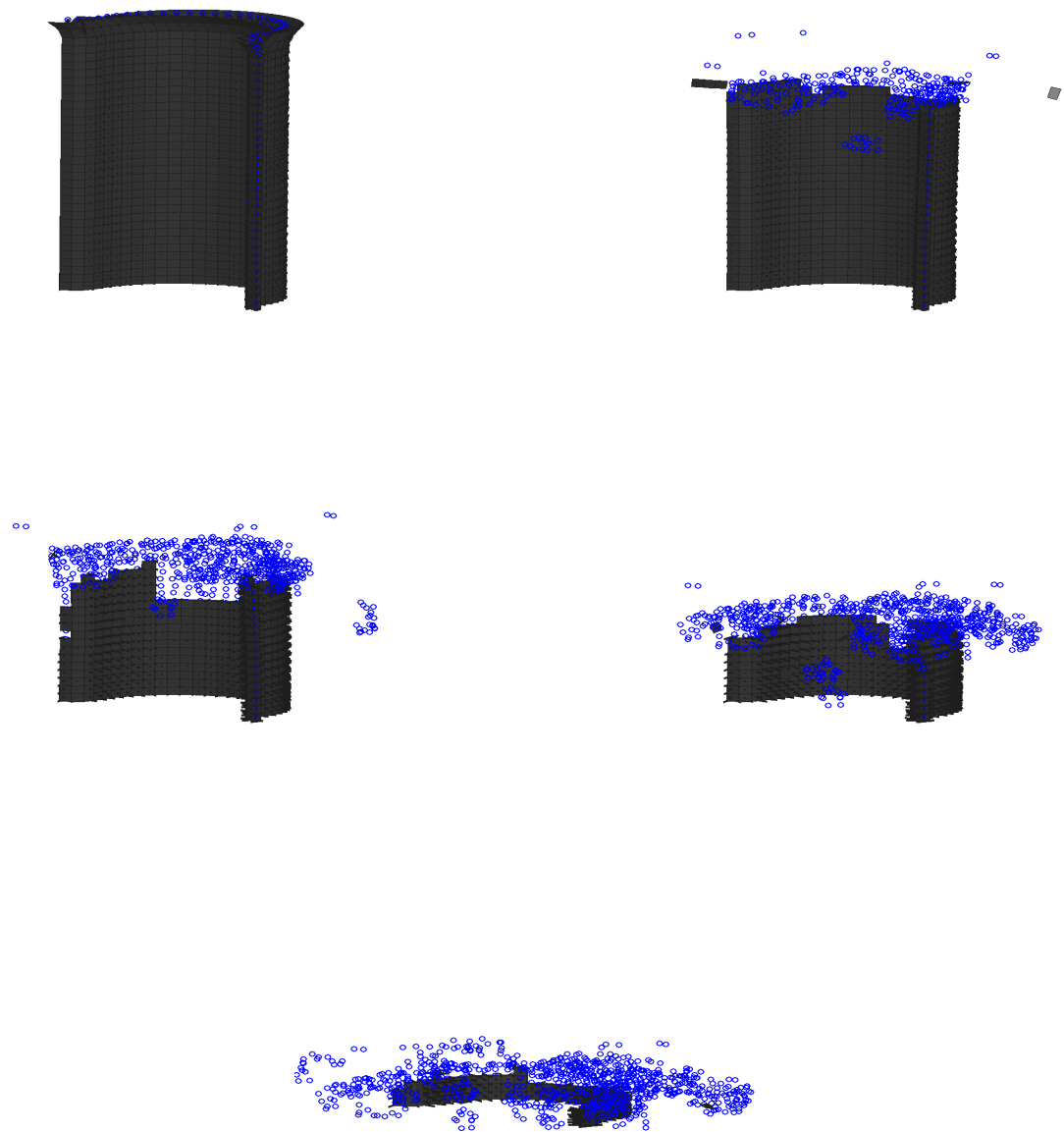


Figure 6.58: Numerical images of crushed carbon-fibre-reinforced composite segment ($v_0=10\text{m/s}$) at a) 0%, b) 20%, c) 40%, d) 60% and e) 80% deformation

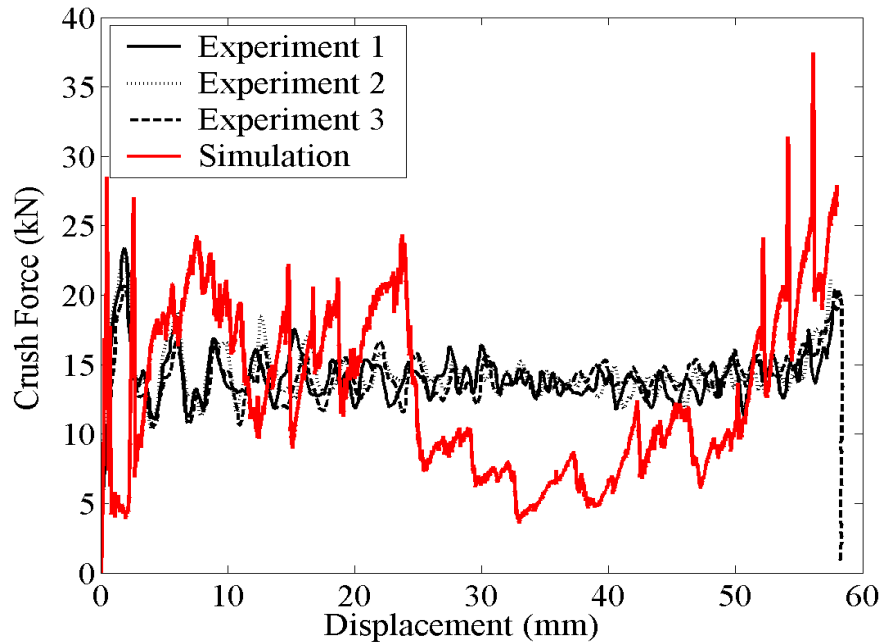


Figure 6.59: Results of dynamic crushing tests - $0^\circ/90^\circ$ ($v_0=5\text{m/s}$)

be obtained, such severe crush force drops are possible.

As one can observe in Fig. 6.59 such crush force drops, between 30-50mm deformation, are more critical than the one observed in Fig. 6.60. This is the result of the early elimination of the segment tube wall observed in the deformation plots (Fig. 6.57). The level of crush force-displacement histories for both velocities differ slightly which was not observed in the experiments and was not expected. Therefore the strain-rate dependency of the material models must be further studies and validated.

6.12 Discussion - Numerical Modelling of the Carbon-Fibre-Reinforced Segments

The dynamic crushing reponse of carbon-fibre-reinforced composite segments are studied under two different loading speeds ($v_0=5\text{m/s}$ and $v_0=10\text{m/s}$). The segment tube walls were modelled with conventional shell elements whilst the discrete particles were used for the resin. The delamination interface and bonding between the segment walls and the resin were realised with tied contact. The numerical simulations show satisfactory agreement with the experimentally obtained results. However the model requires some improvements concerning the material models. Further studies must be also conducted to understand the effect of element size, number of particles and element elimination strain on crushing response.

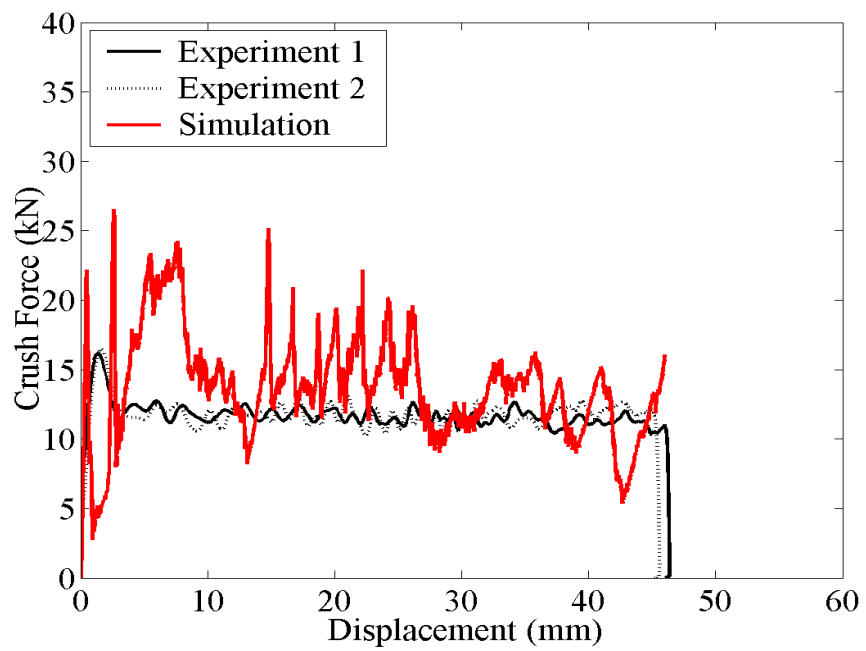


Figure 6.60: Results of dynamic crushing tests - $0^\circ/90^\circ$ ($v_0=10\text{m/s}$)

Conclusions

Numerical techniques based on the coupling of the Finite Element Method (FEM) with the meshless Smooth Particle Hydrodynamics (SPH) Method were proposed for the modelling of composite damage phenomena under crash and impact loads.

The results of the presented study permits the following conclusions to be drawn:

- Although FEM is a well-established numerical tool, it cannot model impact and crush involving large deformation and brittle fragmentation in their complexity.
- SPH Method can be effectively used for the prediction of large deformations and thereby represents an important technique for the high velocity impact (HVI) simulation. It can substitute the FEM-based core models in sandwich structures, which mostly give error termination.
- Because SPH Method is a particle-based meshless method using Lagrangian frame, the coupling of SPH Method and FEM can be established via contact interfaces. In order to optimize the computational time, the discrete particles can be used for the parts where large deformation and damage occurs, whilst FEs for the parts where small deformation take place.
- For the modelling of the fragmentation behaviour the particle nature of the SPH Method offers better possibilities than the FEM.
- The particle discretisation is relatively easy since the discrete particles are generated with a simple transformation of FE mesh into mass points.
- The discrete particles can be embedded into FEs enabling the implementation of a semi-adaptive coupling technique.
- Metallic tube crash absorbers can be correctly modelled with the suggested techniques. The numerical simulations highlighted the experimentally observed deformation modes in detail. The reproducibility of the experimental results and the well-known standard material parameters of metals also contributed to the analysis of results.
- Simulation of the behaviour of composite segments cannot be validated with experimental results due to their specimen-dependent character. The proposed

techniques indicate an important step towards modelling the fragmentation of thin-walled composite structures.

Some limitations of this study must be considered:

- Additionally to the numerical material parameters used to characterise the particle-based material, the SPH Method contact parameters such as smoothing length and radius of the influence, the choice of smoothing function among others are required. Material characterisation of SPH Method-based material models are highly contact parameter-dependent.
- The number of particles and the extent of each particle's domain of influence employed in the simulations with SPH Method and coupled FEM/SPH Method were limited due to the influence on computational time.
- The boundary problem limits the application of the SPH Method, which is unstable under tension load.
- The explicit tool PAM-CRASH has limited material models for SPH option, therefore only an elastic-plastic material model was used throughout the work. This material model, however, itself is also limited and requires further development (e.g.: the friction between the particles and damping are not included in the model).

The presented results indicated the potential of SPH Method and its direct- and semi-adaptive coupling with FEM. Continuous development of the improved simulation tools are needed by designers of energy absorbing composite structures such as helicopter subfloors and landing gear absorbers under crash loads.

Schlussfolgerungen

Numerische Verfahren basierend auf der Kopplung von finiten Elementen (FEM) mit dem netzfreien Smooth Particle Hydrodynamics Verfahren (SPH) wurden für die Modellierung des Nachbruchverhaltens von Verbundstrukturen unter Crash- und Impaktbelastungen vorgeschlagen.

Die in der Arbeit vorgelegten Ergebnisse lassen folgende Schlussfolgerungen zu:

- Obwohl FEM ein etabliertes numerisches Verfahren ist, lassen sich Impakt- und Crushing-Vorgänge mit großen Verformungen und spröder Fragmentierung in deren Komplexität nicht modellieren.
- Das SPH-Verfahren ermöglicht eine genaue Beschreibung von großen Verformungen und stellt somit ein wichtiges numerisches Werkzeug für die Hochgeschwindigkeits-Simulation dar. Dieses Verfahren kann die FEM-basierten Modelle ersetzen, die meistens einen fehlerhaften Abbruch der Simulation verursachen.
- Weil das SPH ein partikelbasiertes netzfreies numerisches Verfahren ist, welches die Lagrangesche (materielle) Beschreibung nutzt, lässt sich dessen Kopplung mit FEM durch Kontaktzonen realisieren. Um die Rechenzeit zu optimieren, empfehlen sich der Einsatz von diskreten Partikeln für die Zonen, in denen große Verformungen auftreten, und von finiten Elementen für die Bereiche, die sich wenig verformen.
- Das SPH-Verfahren bietet mit seinem partikelbasierten Ansatz eine bessere Möglichkeit zur Berechnung des Fragmentationsverhaltens als die FEM-Methode.
- Die Partikeldiskretisierung ist weniger aufwendig, da die diskreten Partikel durch eine einfache Umwandlung von FEM-Netz in mass points generiert werden.
- Die diskreten Partikel werden in finite Elemente eingebettet und erlauben dadurch die Implementierung eines semi-adaptiv gekoppelten Verfahrens.
- Die vorgeschlagenen Verfahren ermöglicht eine korrekte Aussage über das Verhalten von metallischen Crash-Rohren. Die numerischen Ergebnisse bestätigen die experimentell beobachteten Deformationsmoden. Die Reproduzierbarkeit und die weitestgehend bekannten Materialparameter der Metalle trugen dazu bei.

- Aufgrund des probenabhängigen Verhaltens der Verbund-Rohrsegmente lassen sich die Simulationsergebnisse nicht mit den experimentellen Daten validieren. Die hier empfohlenen numerischen Verfahren stellen aber einen wichtigen Schritt in Richtung der Modellierung der Fragmentierung an dünnwändigen Verbundstrukturen dar.

Einige Einschränkungen in dieser Arbeit sind zu beachten:

- Zusätzlich zu den benötigten numerischen Materialparametern für die Charakterisierung des partikelbasierten Materials, müssen die SPH-Kontaktparameter, wie Smoothing-Länge und der Radius des Einflussbereiches und die Smoothing-Funktion ermittelt werden. Die Materialcharakterisierung von SPH-basierten Materialmodellen ist stark von Kontaktparametern abhängig.
- Die Anzahl der eingesetzten Partikel und die Größe des Einflussbereiches der Partikel, die für die Simulation mit SPH und gekoppelten FEM/SPH-Verfahren angesetzt wurden, waren wegen ihres Einflusses auf die Rechenzeit limitiert.
- Die Anwendung des SPH-Verfahrens ist durch das jeweilige Randwertproblem ggf. limitiert; unter Zugbelastung wird das Verfahren instabil.
- Das explizite Berechnungsprogramm PAM-CRASH verfügt über eine begrenzte Anzahl von Materialmodellen für die SPH-Simulation. Deshalb wurde in dieser Arbeit ausschließlich das elastisch-plastische Materialmodell angewandt. Dieses Modell ist allerdings beschränkt und verbesserungsfähig, z.B. werden Reibung und Dämpfung zwischen Partikeln im Modell nicht berücksichtigt.

Die Ergebnisse der beschriebenen Untersuchungen bestätigen das Potenzial des SPH-Verfahrens, der direkten und der semi-adaptiven Kopplung mit der FEM-Methode. Die Weiterentwicklung dieser numerischen Werkzeuge wird weiterhin für die Auslegung von energieabsorbierenden Verbundstrukturen benötigt, z.B. Anwendungsmöglichkeiten sind die Auslegung von Hubschrauberböden oder Pralldämpfer in Fahrwerksanlagen.

Bibliography

- [1] <http://www.carbonfiber.gr.jp/english/tanso/images/plane01b.jpeg>.
- [2] <http://www.carbonfiber.gr.jp/english/tanso/images/plane02b.jpeg>.
- [3] <http://www.embraer.com.br>.
- [4] Aircraft Survival Design Guide, USARTL-TR-79-22 A-E, Vol. 1-V, 1979.
- [5] Annual Statistical Report 2005, CARE, European Commission Community Road Accident Database 2005.
- [6] Alexander J.M., An approximate analysis of collapse of thin-walled cylindrical shells under axial loading, Quarterly of Applied Mathematics, Vol. 13, pp. 1-9, 1960.
- [7] Alghamdi A.A.A., Collapsible impact energy absorbers: an overview, Thin-Walled Structures, Vol. 39, pp. 189-213, 2001.
- [8] Andrews K. R. F., England G. L., Ghani E., Classification of the axial collapse of cylindrical tubes under quasi-static loading, International Journal of Mechanical Science, Vol. 25, No. 9-10, pp. 687-696, 1983.
- [9] Abramowicz W., Jones N., Dynamic axial crushing of circular tubes, International Journal of Impact Engineering, Vol. 2, pp. 263-281, 1984.
- [10] Abramowicz W., Jones N., Dynamic progressive buckling of circular and square tubes, International Journal of Impact Engineering, Vol. 4, pp. 243-269, 1986.
- [11] Jones N., Abramowicz W., Static and dynamic axial crushing of circular and square tubes, In: Reid S.R., editor, Metal Forming and Impact Mechanics, New York: Pergamon Press, pp. 225-247, 1985.
- [12] Wierzbicki T., Bhat S.U., Abramowicz W., Brodtkin D., A two folding elements model of progressive crushing of tubes, International Journal of Solids and Structures, Vol. 29, pp. 3269-3288, 1992.
- [13] Pugsley A.G., Macaulay M., The large scale crumpling of thin cylindrical columns, Quarterly Journal of Mechanics and Applied Mathematics, Vol. 13, Issue 1, pp. 1-9, 1960.

- [14] Abramowicz W., Wierzbicki T., Axial crushing of foam-filled columns, *Journal of Mechanical Science*, Vol. 30, Issues 3-4, pp. 263-271, 1988.
- [15] Abramowicz W., Jones N., Dynamic axial crushing of circular tubes, *International Journal of Impact Engineering*, Vol. 2, pp. 263-281, 1984.
- [16] Thornton P.H., Energy absorptions by foam filled structures, SAE paper 800372, 1980.
- [17] Lampinen B.H., Jeryan R.A., Effectiveness of polyurethane foam in energy absorbing structures, SAE paper 820494, 1982.
- [18] Reid S.R., Reddy T.Y., Gray M.D., Static and dynamic axial crushing of foam filled sheet metal tubes, *International Journal of Mechanical Sciences*, Vol. 23, pp. 295-322, 1986
- [19] Guillow S.R., Lu G., Grezbieta R.H., Quasi-static compression of thin-walled circular aluminum tubes, *International Journal of Mechanical Sciences*, Vol. 43, pp. 2103-2123, 2001
- [20] Reddy T.Y., Wall R.J., Axial compression of foam filled thin-walled circular tubes, *International Journal of Impact Engineering*, Vol. 7, pp. 151-166, 1988.
- [21] Seitzberger M., Rammerstorfer F.G., Grading R., Degischer H.P., Blaimschein M., Walch C., Experimental studies on the quasi-static axial crushing of steel columns filled with aluminum foam, *International Journal of Solids and Structures*, Vol. 37, pp. 4125-4147, 2000.
- [22] Santosa S., Wierzbicki T., Crash behavior of box columns filled with aluminum honeycomb or foam, *Computers and Structures*, Vol. 68, pp. 343-367, 1998.
- [23] Santosa S., Wierzbicki T., Hanssen A.G., Langseth M., Experimental and numerical studies of foam-filled sections, *International Journal of Impact Engineering*, Vol. 24, pp. 509-534, 2000.
- [24] Børvik T., Hopperstad O. S., Reyes A., Langseth M., Solomos G., Dyngeland, T., Empty and foam-filled circular aluminium tubes subjected to axial and oblique quasi-static loading, *International Journal of Crashworthiness*, Vol. 8, pp. 481-494, 2003.
- [25] Santosa S., Wierzbicki T., Effect of an ultralight metal filler on the bending collapse behavior of thin-walled prismatic columns, *International Journal of Mechanical Sciences*, Vol. 41, pp. 995-1019, 1999.
- [26] Kim H.-S., Wierzbicki T., Biaxial bending collapse of thin-walled beams filled partially or fully with aluminum foam, *International Journal of Crashworthiness*, Vol. 5, pp. 363-380, 2000.

- [27] Kim H-S., Analysis of crash response of aluminum foam-filled front side rail of a passenger car, *International Journal of Crashworthiness*, Vol. 2, pp. 189-207, 2001.
- [28] Chen W., Nardini D., Experimental study of crush behavior of sheet aluminium foam-filled sections, *International Journal of Crashworthiness*, Vol. 5, pp. 447-468, 2000.
- [29] Seitzberger M., Rammerstorfer F.G., Degischer H.P., Gradinger R., Crushing of axially compressed steel tubes filled with aluminum foam, *Acta Mechanica*, Vol. 125, pp. 93-105, 1997.
- [30] Chen W., Wierzbicki T., Relative merits of single-cell, multi-cell and foam-filled thin-walled structures in energy absorption, *Thin-Walled Structures*, Vol. 39, pp. 287-306, 2001.
- [31] Santosa S., Wierzbicki T., The concept of double-walled sandwich columns for energy absorption, *International Journal of Crashworthiness*, Vol. 4, Issue 2, pp. 175-197, 1999.
- [32] Zarei H., Kröger M., Optimum honeycomb filled crash absorber design, *Materials and Design*, Vol. 29, pp. 193-204, 2008.
- [33] Hull D., A unified approach to progressive crushing of fibre-reinforced composite tubes, *Composites Science Technology*, Vol. 40, pp. 377-421, 1991.
- [34] Farley G.L., Jones R.M., Crushing characteristics of continuous fiber-reinforced composite tubes, *Journal of Composite Materials*, Vol. 26, pp. 37-50, 1992.
- [35] Farley G.L., The effect of fiber and matrix maximum strain on the energy absorption capability of composite materials, *Journal of Composite Materials*, Vol. 20, pp. 322-334, 1986.
- [36] Hamada H., Coppola J.C., Hull D., Effect of surface treatment on crushing behaviour of glass cloth / epoxy composite tubes, *Composites*, Vol. 23, Issue 2, pp. 93-99, 1992.
- [37] Price J.N., Hull D., Axial crushing of glass fibre-polyester composite cones, *Composites Science and Technology*, Vol. 28, pp. 211-230, 1987.
- [38] Mamalis A.G., Yuan Y.B., Viegelaahn G.L., Collapse of thin-wall composite sections subject to high speed axial loading, *International Journal of Vehicle Design*, Vol. 13, Issues 5-6, pp. 564-579, 1992.
- [39] Mamalis A.G., Manolakos D.E., Viegelaahn G.L., Yap S.M., Demosthenous G.A., On the axial crumpling of fibre-reinforced composite thin-walled conical shells, *International Journal of Vehicle Design*, Vol. 12, Issue 4, pp. 450-467, 1991.

- [40] Mamalis A.G., Manolakos D.E., Viegelaahn G.L., Crashworthy characteristics of thin fibre reinforced composite frusta under axial collapse, *International Journal of Vehicle Design*, Vol. 10, Issue 2, pp. 165-174, 1989.
- [41] Thornton P.H., Edwards P.J., Energy absorption in composite tubes, *Journal of Composite Materials*, Vol. 16, pp. 521-545, 1982.
- [42] Kindervater C.M., Energy absorption of composites as an aspect of aircraft structural crash-resistance, *Developments in the Science and Technology of Composite Materials*, Eds. Füller J. et al., pp. 643-651, Elsevier Applied Science Publishers, London, 1990.
- [43] Farley G.L., Energy absorption of composite materials, *Journal of Composite Materials*, Vol. 17, pp. 267-279, 1983.
- [44] Thornton P.H., Energy absorption in composite structures, *Journal of Composite Materials*, Vol. 13, pp. 247-262, 1979.
- [45] Schmueser D., Wickliffe L.E., Impact energy absorption of continuous fibre composite tubes, *Journal of Engineering Materials and Technology*, Vol. 109, pp. 72-77, 1987.
- [46] Dorey G., Impact and crashworthiness of composite structures, *Structural Impact and Crashworthiness*, Ed. Davies, G.A.O., Vol. 1, pp. 155-192, Elsevier Applied Science Publishers, London, 1984.
- [47] Tao W.H., Robertson R.E., Thornton P.H., Effects of material properties and crush conditions on the crush energy absorption of fiber composite rods, *Composites Science and Technology*, Vol. 47, pp. 405-418, 1993.
- [48] Thornton P.H., Jeryan R.A., Crash energy management in composite automotive structures, *International Journal of Impact Engineering*, Vol. 7, Issue 2, pp. 167-180, 1988.
- [49] Hamada H., Ramakrishna S., Sato H., Effect of fiber orientation on the energy absorption capability of carbon fiber / PEEK composite tubes, *Journal of Composite Materials*, Vol. 30, Issue 8, pp. 947-963, 1996.
- [50] Thornton P.H., Energy absorption in composite structures, *Journal of Composite Materials*, Vol. 13, pp. 247-262, 1979.
- [51] Czaplicki M. J., Robertson R. E., Thornton P., Comparison of bevel and tulip pultruded tubes for energy absorption, *Composites Science and Technology*, Vol. 40, pp. 31-46, 1991.

- [52] Thuis H. G. S. J., Metz V. H., The influence of trigger configurations and laminate lay-up on the failure mode of composite crush cylinders, *Composite Structures*, Vol. 28, Issue 2, pp. 131-137, 1994.
- [53] Jiménez M. A., Miravete A., Larrod E., Revuelta D., Effect of trigger geometry on energy absorption in composite profiles, *Composite Structures*, Vol. 48, Issues 1-3, pp. 107-111, 2000.
- [54] Fairfull A.H., Hull D., Energy absorption of polymer matrix composite structures: Frictional Effects, *Structural Failure*, Eds. Wierzbicki T. and Jones N., pp. 255-279, John Wiley Sons, New York, 1988.
- [55] Mamalis A.G., Manolakos D.E., Demo G. A., *Crashworthiness of composite thin-walled structural components*, Technomic Publishing Co., 1998
- [56] Harte A.-M., Fleck N. A.; Ashby M. F., Energy absorption of foam-filled circular tubes with braided composite walls, *European Journal of Mechanics. A. Solids*, Vol. 19, Issue 1, pp. 31-50, 2000.
- [57] Farley G.L., Energy absorption of composite materials, *Journal of Composite Materials*, Vol. 17, pp. 267-279, 1983.
- [58] Shin K.C., Lee J.J., Kim K.H., Song M.C., Huh J.S., Axial crush and bending collapse of an aluminum/GFRP hybrid square tube and its energy absorption capability, *Composite Structures*, Vol. 57, Issue 1, pp. 279-287, 2002.
- [59] El-Hage H., Mallick P.K., Zamani N., Numerical modelling of quasi-static axial crush of square aluminium-composite hybrid tubes, *International Journal of Crashworthiness*, Vol. 9, Issue 6, pp. 653-664, 2004.
- [60] Song H.W., Wan Z.M., Xie Z.M., Du X.W., Axial impact behaviour and energy absorption efficiency of composite wrapped metal tubes, *International Journal of Impact Engineering*, Vol. 24, pp. 385-401, 2000.
- [61] Babbage J.M., Mallick P. K., Static axial crush performance of unfilled and foam-filled aluminum-composite hybrid tubes, *Composite Structures*, Vol. 70, Issue 2, pp. 177-184, 2005.
- [62] Güden M, Yüksel S., Taşdemirci A., Tanoğlu M., Effect of aluminum closed-cell foam filling on the quasi-static axial crush performance of glass fiber reinforced polyester composite and aluminum/composite hybrid tubes, *Composite Structures*, Vol. 81, Issue 4, pp. 480-490, 2007.
- [63] Abrate S. *Impact on composite structures*. Cambridge University. Press; 1998

- [64] Rhodes M.D., Impact fracture of composite sandwich structures, pp. 311-316, Proceedings of 16th ASME/AIAA/SAE Structures, Structural Dynamics and Material Conference, 1975.
- [65] Mines R.A.W., Worrall C.M., Gibson A.G., Low velocity perforation behaviour of polymer composite sandwich panels, International Journal of Impact Engineering, Vol. 21, pp. 855-879, 1998.
- [66] Charles J.P., Guedra-Degeorges D., Impact damage tolerance of helicopter sandwich structures, Proceedings of 23rd International SAMPE Conference pp. 51-61, 1991.
- [67] Cantwell W.J., Dirat C., Kausch H.H., Comparative study of the mechanical properties of sandwich materials for nautical constructions, SAMPE Journal, Vol. 30, pp. 45-51. 1994.
- [68] Abrate S., Localized impact on sandwich structures with laminated facings, Applied Mechanics Reviews, Vol. 50, pp. 70-82, 1997.
- [69] Hazizan Md. A., Cantwell W.J., The low velocity impact response of foam-based sandwich structures, Composites Part B: Engineering, Vol. 33, Issue 3, pp. 193-204, 2002.
- [70] Raju B.B., Liu D., Dang X., Thickness effects on impact response of composite laminates, Proceedings of the 13th Annual Technical Conference on Composite Materials, Baltimore, Maryland, 21-23 September, 1998.
- [71] Horrigan D.P.W., Aithen R.R., Moltschaniwskyj G., Modelling of crushing due to impact in honeycomb sandwiches, Journal of Sandwich Structures and Materials, Vol. 2, Issue 2, pp. 131-151, 2000.
- [72] Cantwell W.J., Morton J., The influence of varying projectile mass on the impact response of CFRP, Composite Structures, Vol. 13, pp. 101-114, 1989.
- [73] Ambur D.R., Kemmerly H.L., Influence of impactor mass on the damage characteristics and failure strength of laminated composite plates, 39th AIAA/ASME/ASCE/AHS/ASC Structures, Structural Dynamics and Material Conference, Long Beach, California, 20-23 April, 1998.
- [74] Mitrevski T., Marshall I.H., Thomson R., Jones R., Whittingham B., The effect of impactor shape on the impact response of composite laminates, Composite Structures, Vol. 67, Issue 2, pp. 139-148, 2005.
- [75] Partridge I.K., Carti D.D.R., Bonnington T, Manufacture and performance of z-pinned composites. In: Advani S., Shonaike G. editors. Advanced polymeric materials: structure-property relationships, Chapter 3, CRC Press, 2003.

- [76] Carstensen T., Cournoyer D., Kunkel E., Magee C., X-Cor advanced sandwich core material. Published by Society for the Advancement of Material and Process Engineering with Permission. Copyright 2001 by Sikorsky Aircraft Corporation.
- [77] O'Brien K.T., Paris I.L., Exploratory investigation of failure mechanisms in transition regions between solid laminates and X-Cor truss sandwich. NASA/TM-2001-211413 2001 November 19-21.
- [78] Vaidya U.K., Palazotto A.N., Gummadi L.N.B, Low velocity impact and compression-after-impact response of z-pin reinforced core sandwich composites, *Journal of Engineering Materials and Technology*, Vol. 122, pp. 434-442, 2000.
- [79] Palazotto A.N., Gummadi L.N.B., Vaidya U.K., Herup E.J., Low velocity impact damage characteristics of Z-fiber reinforced sandwich panels - an experimental study, *Composite Structures*, Vol. 43, Issue 4, December 1998, pp. 275-288, 1998.
- [80] Cartie D.D., Fleck N., The effect of pin reinforcement upon the through-thickness compressive strength of foam-cores sandwich panels, *Composite Science and Technology*, Vol. 63, Issue 16, pp. 2401-2409, 2003.
- [81] Noels L., Stainier L. , Ponthot J. -P., Combined implicit/explicit algorithms for crashworthiness analysis *International Journal of Impact Engineering*, Vol. 30, Issues 8-9, pp. 1161-117, 2004.
- [82] Noels L., Stainier L. , Ponthot J. -P., Energy conserving balance of explicit time steps to combine implicit and explicit algorithms in structural dynamics, *Computer Methods in Applied Mechanics and Engineering*, Vol. 195, Issues 19-22, pp. 2169-2192, 2006.
- [83] Mishnaevsky L., Dong M., Hönl S., Schmauder S., Computational mesomechanics of particle-reinforced composites, *Computational Materials Science*, Vol. 16, Issues 1-4, pp. 133-14, 1999.
- [84] Cundall P.A., Strack O.D.L., A discrete numerical model for granular assemblies, *Gotechnique*, Vol. 29, Issue 1, pp. 47-65, 1979.
- [85] Kun F., Herrmann H.J., A study of fragmentation processes using a discrete element method, *Computer Methods in Applied Mechanics and Engineering*, Vol. 138, pp. 3-18, 1996.
- [86] Kun F., Herrmann H.J., Transition from damage to fragmentation in collision of solids, *Physical Review E*, Vol. 59, pp. 2623-2632, 1999.
- [87] Kun F., Herrmann H.J., Fragmentation of colliding discs, *International Journal of Modern Physics C*, Vol. 7, pp. 837-855, 1996.

- [88] Masuya H., Kajikawa Y., Nakata Y., Application of the distinct element method to the analysis of the concrete members under impact, *Nuclear Engineering and Design*, Vol. 150, pp. 367-377, 1994.
- [89] D'Addetta G.A., Kuhl E., Ramm E., Kun F., Micromechanical modelling of concrete cracking, *Proceedings of the European Conference on Computational Mechanics (ECCM99)*, Munich, Germany, 31 September - 3 October, 1999.
- [90] Hentz S., Donzé F.V., Daudeville L., Discrete element modelling of concrete submitted to dynamic loading at high strain rates, *Computers and Structures*, Vol. 82, Issues 29-30, pp. 2509-2524, 2004.
- [91] D'Addetta G.A., Kun F., Ramm E., Herrmann H.J., *From solids to granulates - Discrete element simulations of fracture and fragmentation processes in geomaterials*, *Lecture Notes in Physics*, Springer Verlag, Berlin, 2001.
- [92] D'Addetta G.A., Kun F., Ramm E., On the application of a discrete model to the fracture process of cohesive granular materials, *Granular Matter*, Vol. 44, pp. 77-90, 2002.
- [93] Wittel F.K., Schulte-Fischedick J., Kun F., Kröplin B.-H., Frieß M., Discrete element simulation of transverse cracking during the pyrolysis of carbon fibre reinforced plastics to carbon/carbon composites, *Computational Materials Science*, Vol. 28, Issue 1, pp. 1-15, 2003.
- [94] Wittel F.K., Kun F., Kröplin B.-H., Herrmann H.J., A study of transverse ply cracking using a discrete element method, *Computational Materials Science*, Vol. 28, Issues 3-4, pp. 608-619, 2003.
- [95] Wittel F.K., Dill-Langer G., Kröplin B.-H., Modeling of damage evolution in softwood perpendicular to grain by means of a discrete element approach, *Computational Materials Science*, Vol. 32, Issues 3-4, pp. 594-603, 2005.
- [96] Petrinic N., Duffin R., Discrete element modelling of soft body impact against rigid targets, *B2000 Users Workshop*, University of Twente, The Netherlands, 2000.
- [97] Lucy L.B., A numerical approach to the testing of the fission hypothesis, *The Astronomical Journal*, Vol. 82, pp. 1013-1024, 1997.
- [98] Gingold R.A., Monaghan J.J., Smoothed particle hydrodynamics: Theory and applications to non-spherical stars, *Monthly Notices of the Royal Astronomical Society*, Vol. 181, pp. 375-389, 1977.
- [99] Libersky L.D., Petscheck A.G., Smoothed particle hydrodynamics with strength of materials, in *Next Free Lagrange Conference*, Vol. 395, pp. 248-257, Springer Verlag, New York, 1991.

- [100] Libersky L.D., Petscheck A.G., High strain lagrangian hydrodynamics - a three dimensional SPH code for dynamic material response, *Journal of Computational Physics*, Vol. 109, pp. 67-75, 1993.
- [101] Johnson G.R., Stryk R.A., Beissel S.R. SPH for high velocity impact computations, *Computer Methods in Applied Mechanics and Engineering*, Vol. 139, pp. 347-373, 1996.
- [102] Benz W., Asphaug E., Explicit 3d continuum fracture modeling with smoothed particle hydrodynamics, in 24th Lunar and Planetary Science Conference, pp. 99-100, Lunar and Planetary Institute, 1993.
- [103] Benz W., Asphaug E., Impact simulations with fracture, I.Methods and tests, *Icarus*, Vol. 107, pp: 98-116, 1994.
- [104] Randles P.W., Carney T.C., Libersky L.D., Renick J.D., Petscheck A.G., Calculation of oblique impact and fracture of tungsten cubes using smoothed particle hydrodynamics, *International Journal of Impact Engineering*, Vol. 17, pp. 661-672, 1995.
- [105] Benz W., Asphaug E., Simulations of brittle solids using smoothed particle hydrodynamics, *Computer Physics Communications*, Vol. 87, pp. 253-265, 1995.
- [106] Bonet J., Kulasegaram S., Correction and stabilization of smoothed particle hydrodynamics methods with applications in metal forming simulations., *International Journal for Numerical Methods in Engineering*, Vol. 47, pp. 1189-1214, 2000.
- [107] Meywerk M., Simulation der Fluid-Struktur-Interaktion beim Fahrzeugcrash mit einer netzfreien Methode, *VDI Bericht, Tagung Würzburg*, 14-15 September, Nr. 1559, pp. 351-266, 2000.
- [108] Anghileri M., Castelletti Luigi-M. L., Tirelli M., Fluid-structure interaction of water filled tanks during the impact with the ground, *International Journal of Impact Engineering*, Vol. 31, Issue 3, pp. 235-254, 2005.
- [109] McCarthy M.A., Xiao J.R., McCarthy C.T., Kamoulakos A., Ramos J., Gallard J.P., Melito V., Modelling bird impacts on an aircraft wing - Part 2: Modelling the impact with an SPH bird model, *International Journal of Crashworthiness*, Vol. 10, No. 1, pp. 51-59, 2005.
- [110] Johnson A.F., Holzapfel M., Petrinic N., Modelling of soft body impact on composite structures, *Proceedings of European Conference on Computational Mechanics*, Cracow, Poland, 26-29 June, 2001.
- [111] Starke P., Lemmen G., Drechsler K., Validierung von Verfahren für die numerische Simulation von Vogelschlag, 4th LS-DYNA Anwenderforum, Bamberg, 2005.

- [112] Clegg R.A., Sheridan J., Hayhurst C.J., Francis N.J., The application of SPH techniques in AUTODYN-2D to kinetic energy penetrator impacts on multi-layered soil and concrete targets, 8th International Symposium on Interaction of the Effects of Munitions with Structures, Virginia, USA, 22-25 April 1997.
- [113] Fasanella E.L., Jackson K.E., Lyle K.H., Sparks C.E., Sareen A.K., Multi-Terrain Impact Testing and Simulation of a Composite Energy Absorbing Fuselage Section , AHS International 60th Annual Forum Technology Display, Baltimore, Maryland, June 7-10, 2004.
- [114] Oger G., Doring M., Alessandrini B., Ferrant P., Two-dimensional SPH simulations of wedge water entries, Journal of Computational Physics, Vol. 213, Issue 2, Pages 803-822, 2006.
- [115] Pentecôte N., Kohlgrüber D., Full-scale simulation of aircraft impacting on water, ICRASH 2004, International Crashworthiness Conference, San Francisco, USA, July 14 - 16, 2004.
- [116] Naghipour P., Aktay L, Johnson A.F., Numerical investigation of structural crash response of thin-walled structures on soft soil, Materials and Design, Vol. 29, pp. 2052-2060, 2008.
- [117] Johnson G.R., Stryk R.A., Beissel S.R. SPH for high velocity impact computations, Computer Methods in Applied Mechanics and Engineering, Vol. 139, pp. 347-373,1996.
- [118] Randles P.W., Libersky L.D., Smoothed particle hydrodynamics: Some recent improvements and applications, Computer Methods in Applied Mechanics and Engineering, Vol. 139, pp. 375-408, 1996.
- [119] Belytschko T., Liu W.K., Moran B., Nonlinear Finite Elements for Continua and Structures, John Wiley and Sons, New York, 2000.
- [120] Liu W.K., Oberste-Brandenburg C., Reproducing kernel and wavelet particle methods, Aerospace structures: Nonlinear Dynamics and System Response, pp. 39-56, 1995.
- [121] Liu W.K., Adee J., Jun S., Reproducing kernel and wavelet particle methods for elastic and plastic problems, Advanced Computational Methods for Material Modeling, pp. 175-190, 1993.
- [122] Liu W.K., Jun S., Zhang Y.F., Reproducing kernel methods, International Journal for Numerical Methods in Engineering, Vol. 20, pp. 1081-1106, 1995.

- [123] Takeda H., Miyama S.M., Sekiya M., Numerical simulation of viscous flow by smoothed particle hydrodynamics, *Progress of Theoretical Physics*, Vol. 116, pp. 123-134, 1994.
- [124] Morris J.P., Fox P.J., Zhu Y., Modeling low Reynolds number incompressible flow using SPH, *Journal of Computational Physics*, Vol. 136, pp. 214-226, 1997.
- [125] Li S., Liu W.K., Meshfree and particle methods and their applications, *ASME Applied Mechanics Review*, Vol. 54, pp. 1-34, 2002.
- [126] Zienkiewicz O.C., Kelly D.W., Bettress F., The coupling of the finite element method and boundary solution procedures, *International Journal for Numerical Methods in Engineering*, Vol. 11, pp. 355-375, 1977.
- [127] Krishnamurthy T., Raju I.S., Coupling of finite and boundary element methods for two-dimensional potential problems, *International Journal for Numerical Methods in Engineering*, Vol. 36, pp. 3593-3616, 1993.
- [128] Belytschko T., Organ D., Krongauz Y., Coupled finite element-elementfree galerkin method, *Computational Mechanics*, Vol. 17, Issue 3, pp. 186-195, 1995.
- [129] Hegen D., Element-free galerkin methods in combination with finite element approaches, *Computer Methods in Applied Mechanics and Engineering*, Vol. 135, Issues 1-2, pp. 143-166, 1996.
- [130] Huerta A., Fernandez-Mendez S., Enrichment and coupling of the finite element and meshless methods, *International Journal for Numerical Methods in Engineering*, Vol. 48, Issue 11, pp. 1615-1636, 2000.
- [131] Rao B.N., Rahman S., A coupled meshless-finite element method for fracture analysis of cracks, *International Journal of Pressure Vessels and Piping*, Vol. 78, Issue 9, pp. 647-657, 2000.
- [132] Liu G.R, Gu Y.T., Coupling of element free galerkin and hybrid boundary element methods using modified variational formulation, *Computational Mechanics*, Vol. 26, Issue 2, pp. 166-173, 2000.
- [133] Liu G.R., Gu Y.T., Meshless local Petrov-Galerkin(MLPG) method in combination with finite element and boundary element approaches, *Computational Mechanics*, Vol. 26, Issue 6, pp. 536-546, 2000.
- [134] Munjiza A., Bangash T., John N. W. M., The combined finite-discrete element method for structural failure and collapse, *Engineering Fracture Mechanics*, Vol. 71, Issues 4-6, pp. 469-483, 2004

- [135] Han K., Peric D., Crook A.J.L., Owen D.R.J., A combined finite/discrete element simulation of shot peening processes - Part I: studies on 2D interaction laws, *Engineering Computations*, Vol. 17, Issue 5, pp. 593 - 620, 2000.
- [136] Han K., Peric D., Owen D.R.J., Yu J., A combined finite/discrete element simulation of shot peening processes - Part II: 3D interaction laws, *Engineering Computations*, Vol. 17, Issue 6, pp. 680-702, 2000.
- [137] Owen D.R.J., Peric D., Mohammadi S., *Discrete Element Modelling of Multi-Fracturing Solids and Structures, Foreign Object Impact and Energy Absorbing Structure (Seminar Papers)*, IMECHE, London, 4 March, 1998.
- [138] Chen T., Raju S.I., Coupling finite element and meshless local petrov-galerkin methods for two-dimensional potential problems. Tech Report AIAA-2002-1659, American Institute of Aeronautics and Astronautics, American Institute of Aeronautics and Astronautics, 2002.
- [139] Zienkiewicz O.C., Kelly D.W., Bettress F., The coupling of the finite element method and boundary solution procedures, *International Journal for Numerical Methods in Engineering*, Vol. 11, pp. 355-375, 1977.
- [140] Krishnamurthy T., Raju I.S., Coupling of finite and boundary element methods for two-dimensional potential problems, *International Journal for Numerical Methods in Engineering*, Vol. 36, pp. 3593-3616, 1993.
- [141] Belytschko T., Organ D., Krongauz Y., Coupled finite element-elementfree galerkin method, *Computational Mechanics*, Vol. 17, Issue 3, pp. 186-195, 1995.
- [142] Liu G.R., Gu Y.T., Coupling of element free galerkin and hybrid boundary element methods using modified variational formulation, *Computational Mechanics*, Vol. 26, Issue 2, pp. 166-173, 2000.
- [143] Liu G.R., Gu Y.T., Meshless local Petrov-Galerkin(MLPG) method in combination with finite element and boundary element approaches, *Computational Mechanics*, Vol. 26, Issue 6, pp. 536-546, 2000.
- [144] Hegen D., Element-free galerkin methods in combination with finite element approaches, *Computer Methods in Applied Mechanics and Engineering*, Vol. 135, Issues 1-2, pp. 143-166, 1996.
- [145] Huerta A., Fernandez-Mendez S., Enrichment and coupling of the finite element and meshless methods, *International Journal for Numerical Methods in Engineering*, Vol. 48, Issue 11, pp. 1615-1636, 2000.

- [146] Rao B.N., Rahman S., A coupled meshless-finite element method for fracture analysis of cracks, *International Journal of Pressure Vessels and Piping*, Vol. 78, Issue 9, pp. 647-657, 2000.
- [147] Gu Y.T., Liu G.R., *Meshless Methods Coupled with Other Numerical Methods*, Tsinghua Science Technology, Vol. 10, Issue 1, pp. 8-15, 2005.
- [148] Attaway S. W., Heinstein M. W., Swegle J. W., Coupling of smooth particle hydrodynamics with the finite element method, *Nuclear Engineering and Design*, Vol. 150, Issues 2-3, pp. 199-205, 1994.
- [149] Johnson G. R., Linking of Lagrangian particle methods to standard finite element methods for high velocity impact computations, *Nuclear Engineering and Design*, Vol. 150, Issues 2-3, pp. 265-274, 1994.
- [150] Johnson G.R., Petersen E.H., Stryk R.A., Incorporation of an SPH option into epic code for a wide range of high velocity impact computations, *International Journal of Impact Engineering*, Vol. 14, pp. 385-394, 1993.
- [151] Sauer M., Hiermeier S., Scheffer U., Modelling penetration events using FE/MLSPH adaptive coupling. 10th International Symposium on Interaction of the Effect of Munitions with Structures, San Diego, California, 7-11 May, 2001
- [152] De Vuyst, T., Vignjevic R., Campbell J.C., Coupling between meshless and finite elements methods, *International Journal of Impact Engineering*, Vol. 31, pp. 1054-1064, 2005.
- [153] Johnson G.R., Stryk R.A., Beissel S.R. SPH for high velocity impact computations, *Computer Methods in Applied Mechanics and Engineering*, Vol. 139, pp. 347-373, 1996.
- [154] Johnson G. R., Stryk R.A., Conversion of 3D distorted elements into meshless particles during dynamic deformation, *International Journal of Impact Engineering*, Vol. 28, Issue 9, pp. 947-966, 2003.
- [155] Cottrell M.G., Yu J., Owen D.R.J., The adaptive and erosive numerical modelling of confined boron carbide subjected to large-scale dynamic loadings with element conversion to undeformable meshless particles, *International Journal of Impact Engineering*, Vol. 28, Issue 9, pp. 1017-1035, 2003.
- [156] Beissel S.R., Gerlach C.A., Johnson G.R., Hypervelocity impact computations with finite elements and meshfree particles, *International Journal of Impact Engineering*, Vol. 33, Issues 1-12, pp. 80-90, 2006.
- [157] Johnson A.F., Holzapfel M., Modelling soft body impact on composite structures, *Composite Structures*, Vol. 61, Issues 1-2, pp. 103-113, 2003.

- [158] Ladeveze P., Le Dantec E., Damage modelling of the elementary ply for laminated composites, *Composites Science and Technology*, Vol. 43, pp. 257-267, 1992.
- [159] Johnson A.F., Pickett A.K., Impact and crash modelling of composite structures: a challenge for damage mechanics, *European Conf. Computational Mechanics*, ECMM 99, Munich, 1999.
- [160] High Velocity Impact of Composite Aircraft Structures (HICAS), EU RTD Project BE 96-4238, 1998-2000.
- [161] PAM-CRASH FE Code, Engineering Systems International, 20 Rue Saarinen, Silic 270, 94578 Rungis-Cedex, France.
- [162] Johnson A.F., Kohlgrüber D., Design and performance of energy absorbing sub-floor structures in aerospace applications, *IMEchE Seminar S672*, London, 9 May, 2000.
- [163] Şerifi E., Hirth A., Matthei S., Müllerschön H., Modelling of foams using MAT83 - Preparation and evaluation of experimental data, 4th European LS-DYNA Users Conference, Ulm, Germany, 22-23 May, 2003.
- [164] Gibson L.J., Ashby M.F., *Cellular Solids: Structure and Properties*, Pergamon Press, Oxford, 1988.
- [165] Hiermaier S., Thoma K. Computational simulation of high velocity impact simulations using smoothed particle hydrodynamics, 9th DYMAT Technical Conference on Materials and Structural Modelling in Collision Research, TU Munich Germany 1995.
- [166] Aktay L., Johnson A.F., Kröplin B.-H., Semi-adaptive coupling technique for the prediction of impact damage, *Complas 2005*, Proceedings of the VIII International Conference on Computational Plasticity Fundamentals and Applications, Barcelona, Spain, 5-8 September, 2005.
- [167] Güden M., Yüksel S., Compression behavior of SiC-particulate foams produced by foaming from powder compacts, *Journal of Materials Science*, Vol. 41, pp. 4075-4084, 2006.
- [168] Singace A.A., El-Sobky H., Interplay of factors influencing collapse modes in axially crushed tubes, *International Journal of Crashworthiness*, Vol. 5, pp. 279-297, 2000.
- [169] Hanssen A.G., Langseth M., Hopperstad O.P., Static and dynamic crushing of square aluminium extrusions with aluminum foam filler, *International Journal of Impact Engineering*, Vol. 24, pp. 347-383, 2000.

- [170] Hanssen A.G., Hopperstad O.S., Langseth M., Design of aluminium foam-filled crash boxes square and circular cross-sections. *International Journal of Crashworthiness*, Vol. 6, pp. 177-188, 2001.
- [171] Singace A.A., Collapse behaviour of plastic tubes filled with wood sawdust, *Thin-Walled Structures*, Vol. 37, pp. 163-187, 2000.
- [172] Toksoy A.K., Güden M., Tanoğlu M., Hall I.W., Effect of adhesive on the strengthening of foam-filled circular tubes, *Journal of Material Sciences*, Vol. 39, pp. 1503-1506, 2004.
- [173] Hanssen A.G., Langseth M., Hopperstad O.P., Optimum design for energy absorption of square aluminium columns with aluminium foam filler, *International Journal of Mechanical Sciences*, Vol. 43, pp. 153-176, 2001.
- [174] Seitzberger M, Willminger S. Application of plastic collapse mechanisms for the axial crushing analysis of tubular steel structures filled with aluminum foam, *International Journal of Crashworthiness*, Vol. 6, pp. 165-176, 2001.
- [175] Aktay L., Toksoy A.K., Güden M., Quasi-static axial crushing of extruded polystyrene foam-filled thin-walled aluminum tubes: experimental and numerical analysis. *Materials and Design*, Vol. 27, pp. 556-565, 2007.
- [176] "Commercial Aircraft - Design for Crash Survavibility": CRASURV, D.1.1.1 Initial Materials Data of Carbon and Aramid Fabric Materials, 1997.
- [177] Holzapfel M., Kopp G., Adamski P., Elsenhans H., Christlein J., Hambrecht T., Numerische Nachbildung der Crashfront von faserverstärkten Strukturen mit Hilfe von Mehrschalenmodellen, 6.LS-DYNA Anwenderforum, Frankenthal, 2007.

Curriculum Vitae

Personal Data

Name	Levent Aktay
Date of Birth	June 02, 1977
Place of Birth	Ankara, Turkey
Marital Status	Married, 1 child
Nationality	Turkish

School Education

1983-1984	Kozyatağı Primary School, Istanbul
1984-1987	Hilal Primary School, Izmir
1987-1988	Şehit Rahmi Primary School, Balıkesir
1988-1991	Suphi Koyuncuoğlu Secondary School, Izmir
1991-1994	Üsküdar Science High School, Istanbul

University Education

1994-1999	Undergraduate Studies of Mechanical Engineering, Yıldız Technical University, Istanbul
1999-2000	Graduate Studies of Chemical Engineering, Friedrich Alexander University of Erlangen-Nürnberg, Nürnberg
2000-2002	M.Sc. in Computational Mechanics of Materials and Structures (COMMAS), University of Stuttgart
2002-2006	Doctoral Candidate, Institute of Structures and Design German Aerospace Center (DLR), Stuttgart

Professional Carrier

04/2006-10/2007	CAE Engineer, TECOSIM GmbH, Stuttgart
10/2007-05/2008	CAE Engineer, MBtech GmbH, Sindelfingen
since 05/2008	CAE Engineer, Daimler AG, Sindelfingen